Scalar Analogues of Compact Astrophysical Systems

by

Scott Hearne Hawley, B.S.

Dissertation

Presented to the Faculty of the Graduate School of

The University of Texas at Austin

in Partial Fulfillment

of the Requirements

for the Degree of

Doctor of Philosophy

The University of Texas at Austin

August 2000

Scalar Analogues of Compact Astrophysical Systems

Approved by
Dissertation Committee:

_____

_____

_____

_____

_____

To my family

Acknowledgments

I present these acknowledgements in "list" form, as there are many persons to thank: I wish to acknowledge my supervisor, Matthew Choptuik, for his guidance, provision and professional assistance in helping me become a competent independent researcher. I acknowledge Richard Matzner for graciously agreeing to serve as co-supervisor after changes to the committee became necessary, and for helpful discussions. I acknowledge my friend and fellow student J. Brian Pitts for his exceptional support and for many helpful interactions. Manish Parashar, primary developer of the GrACE package discussed in Chapter 5, deserves hearty thanks for his patience and assistance in my attempt to develop a more generic AMR application than those previously available. Thanks to Professor Jerry Bona for several delightful discussions of methods for solving the PDEs I was dealing with. Thanks to Greg Shields for his interest in helping me, for providing encouragement and many fascinating discussions of astrophysical phenomena. I wish to acknowledge Steve Liebling and Eric Hirschmann for their tutelage and assistance in the early stages of my boson star research discussed in Chapter 3. Thanks to Wai-Mo Suen for providing his source code to solve for the soliton star initial data, which was useful in developing the "multi-scalar stars" of Chapter 4. Thanks to Ashley Hill for her support and assistance regarding the project management of this dissertation. Thanks to the students and staff of the Center for Relativity, and David Nielsen and Luis Lehner in particular, for assistance, instruction, and lots of laughs. I acknowl-

SCOTT HEARNE HAWLEY

The University of Texas at Austin

August 2000

Scalar Analogues of Compact Astrophysical Systems

Publication No. _____

Scott Hearne Hawley, Ph.D.

The University of Texas at Austin, 2000

Supervisor: Matthew W. Choptuik

Co-Supervisor: Richard A. Matzner

This dissertation concerns the numerical simulation of scalar fields in curved space-times, in configurations which bear similarities to certain astrophysical systems. We present a new study of black hole threshold phenomena associated with "boson stars", which are star-like equilibrium solutions of the coupled Einstein and Klein-Gordon equations. We construct Type I critical solutions dynamically by imploding around the boson star a carefully tuned spherical shell consisting of a massless real scalar field. We compare the resulting critical solutions with unstable boson stars via an extension of the linear perturbative analysis of Gleiser and Watkins [Nucl. Phys. B**319** 733 (1989)], and establish a close link between spherically-symmetric critical solutions of a massive complex field and unstable boson stars. This work implies that unstable boson stars are unstable toward dispersal in addition to black hole formation, and may imply that neutron stars at or beyond the point of insta-bility may also be unstable to explosion. We also discuss "multi-scalar stars", a new class of quasi-periodic compact solutions which were discovered in the course of the boson star simulations. We further present work toward the development

of a computing environment to provide parallel adaptive mesh refinement (AMR) *automatically* to developers of sequential, single-grid finite difference codes. This work involves a hybrid of algorithms developed over several years at multiple institutions, presented in one cohesive package with the addition of several important new features. We consider an application to solve a canonical hyperbolic system, the wave equation, which serves as a prototype for a "generic driver" for AMR applications. To serve as a test case for the adaptive mesh refinement methods, as well as to provide information about a system which has received little study, we consider the evolution of a massive complex field coupled to an electromagnetic field in the vicinity of a Kerr black hole. Such a system has features similar to those of magnetohydrodynamic accretion disks, yet should allow for a simpler numerical treatment due to the absence of shocks. We present work in progress to create a three-dimensional single-grid code to interface with the adaptive mesh refinement driver.

Contents

List of Tables

List of Figures

Chapter 1

Introduction

1.1 Notation and Conventions

Throughout this dissertation we will use the traditional "numerical relativity" notation which is also employed in Misner, Thorne and Wheeler [73]. Namely, we employ a metric with signature $-+++$, we will use Greek indices to run from 0 to 3 (*i.e.* over time and space) and Latin indices to run from 1 to 3 (for spatial quantities), with the summation convention applied over each set of indices. We will use the symbol ∇_μ to denote the covariant derivative compatible with the four-dimensional metric $g_{\mu\nu}$, and the symbol D_i as the covariant derivative compatible with the three dimensional "spatial" metric h_{ij}. (Indices of "spatial" vectors such the electric and magnetic fields E^i and B^i are raised and lowered using h_{ij}.) As an additional shorthand notation throughout this dissertation, we will often employ the non-tensorial operator $\partial^\mu \equiv g^{\mu\nu} \partial_\nu$. (We will only use this operator on scalar fields.) We will work in geometrized units, such that Newton's constant $G = 1$ and the speed of light $c = 1$. For the massive scalar fields covered in this dissertation, the "boson mass" m has units of inverse length, for which the corresponding physical mass is $m\hbar/c$. Thus we choose $\hbar = 1$, but we emphasize that all the discussions and results

1

to follow are given within the context of *classical* field theory.

1.2   Layout

This thesis is concerned with the numerical simulation of systems which feature
scalar fields in strong gravitational fields. These systems bear many similarities to
well-known astrophysical fluid systems. A scalar field provides a useful matter source
which shares many features of a fluid, yet the scalar field is described by simpler
equations of motion, and thus can provide a simple "toy model" of an astrophysical
matter source with which to study dynamics in general relativity. This thesis is
divided into the following principal parts: boson stars, multi-scalar stars, scalar
accretion and adaptive mesh refinement.

    Boson stars are compact bodies composed of a complex massive scalar field,
minimally coupled to the gravitational field of general relativity. These objects are
local equilibrium solutions of the Einstein and Klein-Gordon equations, in which the
spacetime is *static,* although the real and imaginary components of the scalar field
oscillate. Boson stars have similarities to neutron stars, such as their possession
of a maximum mass which marks the transition from stability to instability. We
present dynamical simulations of boson stars which are driven to the threshold of
black formation via an exchange of energy with an additional real, massless scalar
field. We show that the critical solutions appear to be unstable boson stars.

    Multi-Scalar Stars are a family of stable, quasi-periodic compact solutions
to the Einstein-Klein-Gordon system which were discovered in the course of the
boson star simulations. This class of solutions contains boson stars and oscillating
soliton stars (which are periodic solutions involving a single real field) as subsets.
The remarkable feature of these multi-scalar solutions is that they indicate that
stable, quasi-periodic solutions are perhaps more generic than has been previously
assumed. We discuss the construction of multi-scalar stars and relate results of some

simulations of these objects.

Adaptive Mesh Refinement (AMR) is the name given to a class of techniques that can be used when modeling physical systems using approximate finite-difference solutions of partial differential equations. For simulations in which a fixed local accuracy is desired, the required resolution may vary widely both in space and in time, in a manner which is unknown *a priori*. AMR is a way of providing the appropriate amount of resolution throughout the space-time domain, and allows one to generate solutions within a desired error tolerance at a fraction of the cost of a corresponding uniform-grid (unigrid) application. However, even given a certain amount of computing efficiency one obtains from AMR, current finite-difference codes must be parallelizable if they are to take full advantage of the largest computers commonly available to researchers. AMR and parallelization each present significant challenges which for many researchers may be prohibitive and lead us to investigate the development of environments where AMR and parallelization are provided "automatically". This thesis includes work towards the creation of one such environment.

Scalar accretion is a term we will use to denote the dynamics of a scalar field which is being swallowed by a black hole. The intended system referenced here is a scalar "accretion disk" in which the scalar field is charged and coupled to an electromagnetic field, and evolving in the vicinity of a rotating black hole. This research was intended to serve as useful test case for the adaptive mesh refinement techniques described above. This work is just beginning, and we discuss the necessary background for the material and give a current status report.

1.3   Connection with Other Research

Scalar fields have not been measured by any experiment to date, yet current theories of particle physics and cosmology call for the existence of one or more scalar

(or pseudo-scalar) fields. Furthermore, measurements of galaxy rotation curves and the properties of galaxy clusters indicate that there is a substantial amount of non-baryonic matter, "dark matter", in the universe. The scalar fields studied in this thesis provide one candidate for the weakly-interacting "missing mass" of our universe. It is reasonable to suggest that, if these fields exist, they might reach sufficient densities in certain places as to condense into the compact objects we call boson stars, or be drawn into black holes (formed by scalar or fermionic matter) and display some of the dynamics described in this work.

The boson star research is interesting principally for what it tells us about strong-field gravity. Dynamic solutions of Einstein's equations in their full nonlinearity are fairly recent additions to the field of relativity, and the solution space of the theory is still largely unexplored. The work presented in this thesis is a further contribution to the study of critical phenomena in gravitational collapse, which began not quite a decade ago. This research may also suggest a direction for neutron star research in the near future, given the suggestion that, because boson stars can explode, neutron stars can probably do the same. This may prove to be a foundation for providing yet another scenario (among many) describing the mysterious gamma ray bursts measured by spaceborne gamma ray observatories.

The scalar accretion study, like the boson star work, also serves as both a "toy model" for more conventional (fermionic) astrophysics, and an interesting study in its own right about a system which has received very little attention. It is in part a stepping-stone to the goal of full 3D magnetohydrodynamic (MHD) simulations in evolving spacetimes. We may be able capture some features thought to be important in astrophysical fluid systems, such as processes for extracting energy from the black hole, and the production of high-speed jets.

The AMR work has relevance for computational physics as a whole, because many researchers are now interested in performing 3+1-dimensional simulations of

various phenomena, and such simulations will require efficient use of computational resources to provide sufficient resolution of interesting features in the system. Two applications of interest to this author are the binary black hole problem and the global simulation of MHD accretion disks.

1.4 Our Matter Model

1.4.1 Scalar Fields Themselves

What is a scalar field, "physically"? All the systems considered in this thesis are conceived within the context of *classical* field theory. In this view, the scalar field represents another fundamental field, like the electromagnetic and gravitational fields As mentioned previously, such additional fundamental fields are a feature of some popular theories of particles physics and cosmology, so fields such as those studied in this thesis may indeed exist in our universe. We will use the term "boson" at times (*e.g.* "boson star"), since scalar fields would be composed of spin-0 (bosonic) particles. The scalar field is regarded as a smoothly-varying field, a function defined on all points in space and time, for which the values of this function and its spatial and temporal derivatives contribute to a local energy density everywhere in the spacetime. This function evolves according to the well-known Klein-Gordon equation, with some possible coupling to other fundamental fields in the model, and may include a "mass" term which gives a dispersive quality to "wave packets" comprised of the scalar field. This dispersion is important as it provides an effective repulsive pressure, which can support a condensed mass of the field against gravitational collapse and allow it to form a boson star. Even if scalar fields do not actually exist in our universe, their study is nevertheless significant. Scalar fields have often been employed in relativity research because they represent a very simple matter source, having only one (coordinate-invariant) component and possessing nontrivial

dynamics in spherical symmetry.

In this thesis, we will consider complex and real scalar fields. For the boson star study of Chapter 3, we will use a model in which one complex massive field and one real massless field are coupled to the gravitational field of general relativity in spherical symmetry. Chapter 4 discusses the dynamics of two real massive fields coupled to gravitational field of general relativity. In Chapter 6, we will we will consider a massive complex field coupled dynamically to an evolving electromagnetic field in the presence of the static spacetime of a rotating black hole.

1.4.2 Scalar Fields vs. Hydrodynamics

Scalar fields share some properties with perfect fluids, which are often used in more 'realistic' models of astrophysical systems. A perfect fluid is characterized by three quantities: a fluid 4-velocity vector field, an energy density scalar field, and an isotropic pressure scalar field [37]. The stress energy tensor for a perfect fluid is given by

$$T^{\mu\nu} = (\rho + p)u^\mu u^\nu + pg^{\mu\nu} \tag{1.1}$$

where ρ and p are the energy density and pressure, respectively, in the rest frame of the fluid, u^μ is the fluid 4-velocity, and $g^{\mu\nu}$ is the metric tensor.

An important difference between scalar fields and fluids is that characteristics of the scalar field wave equation do not cross, and thus these systems do not develop discontinuities in generic evolutions of smooth initial data. The tendency of fluids to form shock waves presents a significant challenge to computational fluid dynamicists, requiring a host of sophisticated numerical techniques to handle these features properly in a computer code. Fluid systems also require special treatment for very low densities because the fluid equations are not well defined in the vacuum limit. For this dissertation, we will not need to handle shock waves, and can employ the more conventional methods developed for smoothly-evolving functions.

The similarities between scalar fields and perfect fluids can be made more rigorous by following a discussion due to Madsen [68]. A real scalar field can be described by the Lagrangian density

$$\mathcal{L} = -\frac{1}{2}\left(\partial^\mu\phi\partial_\mu\phi\right) + V(\phi) \tag{1.2}$$

where $V(\phi)$ is some potential term. The stress energy tensor is written as

$$T^{\mu\nu} = \partial^\mu\phi\partial^\nu\phi + \mathcal{L}g^{\mu\nu} \tag{1.3}$$

By comparing (1.1) and (1.3), we see that the fluid quantities are related to the scalar field quantities by

$$p = \mathcal{L} \tag{1.4}$$

$$(\rho + p)u^\mu u^\nu = \partial^\mu\phi\partial^\nu\phi \tag{1.5}$$

For the effective 4-velocity of the scalar field, we can define a vector field of unit magnitude via

$$u^\mu = \frac{\partial^\mu\phi}{\sqrt{-\partial^\nu\phi\partial_\nu\phi}}\,, \tag{1.6}$$

which only provides a meaningful notion of velocity when $\partial^\mu\phi$ is timelike. Contracting (1.5), we find

$$-(\rho + p) = \partial^\mu\phi\partial_\mu\phi$$

or, using (1.2) and (1.4),

$$\rho = p + 2V(\phi)\,. \tag{1.7}$$

For the complex fields used in this thesis, the discussion proceeds in the same manner as above, where $V(\phi)$ becomes $V(|\phi|)$, and in which we define the 4-velocity as

$$u^\mu = \frac{\partial^\mu|\phi|}{\sqrt{-\partial^\lambda|\phi|\partial_\lambda|\phi|}}\,. \tag{1.8}$$

An alternative definition would involve a complex 4-velocity,

$$\tilde{u}^\mu = \frac{\partial^\mu\phi}{\sqrt{-\partial^\lambda\phi\partial_\lambda\phi^*}}\,, \tag{1.9}$$

for which $\tilde{u}^a \tilde{u}^*_a = -1$, and in which the real and imaginary parts of $\tilde{u}$ provide notions of the 4-velocities of the real and imaginary parts of the field, respectively. With a complex 4-velocity the stress-energy tensor takes the form

$$T^{\mu\nu} = (\rho + p)\tilde{u}^\mu \tilde{u}^{*\nu} + pg^{\mu\nu} \,. \tag{1.10}$$

It is perhaps worth noting that in recent work by Schunck and collaborators [87, 35, 72], as well as the original work of Kaup [62], stated that the effective pressure is *anisotropic* in a boson star, whereas our preceeding discussion indicates that the effective pressure for scalar fields is indeed a scalar quantity (namely, the Lagrangian density). Schunck and collaborators seem to claim the existence of this pressure anisotropy on the basis that the stress energy tensor in mixed form, T^μ_ν, is not expressible in the form $\mathrm{diag}(-\rho, p, p, p)$ but rather as

$$T^\mu_\nu = \mathrm{diag}(-\rho, p_r, p_\perp, p_\perp) \,, \tag{1.11}$$

where p_r and $p_\perp$ are generally different. It seems likely that these authors do not pursue the idea of defining a velocity field in the manner described in preceeding paragraphs, since (as we shall see) the boson star is a standing wave and is *not moving* in the usual Schwarzschild-like coordinates, and thus the anisotropic stress (for comparison to static fluid stars) may be regarded as an anisotropic pressure. Since a scalar field is *not* a fluid, the notion of the field "velocity" (and hence "pressure"), while not entirely arbitrary, may be best chosen according to the features of the problem in which one is interested.

The preceeding discussion is intended to help establish the link between scalar fields and fluids. In addition to the merits of studying scalar field systems in their own right, and in addition to the value of such studies as testbeds for developing numerical techniques, the similarities between some properties of scalar fields and perfect fluids provide us with the possibility of deeper understanding of some fluid systems.

Chapter 2

Theoretical Background

2.1 Topics in Relativity

2.1.1 3+1 Decomposition

Often it is useful to view the "timeless" four-dimensional spacetime manifold as a series of snapshots of three-dimensional space which evolve with time. More technically, we say that we can decompose the spacetime into a one-parameter foliation of spacelike hypersurfaces, with the family parameter t serving as a time coordinate. We often refer to these spacelike surfaces as "slices" through the spacetime, and the choice of time coordinate as a choice of "slicing." In this view we then have three spatial dimensions plus one time dimension, and hence we attach the name "3+1" to this view of spacetime. The mathematical formalism associated with this view was presented in definitive form by Arnowitt, Deser and Misner [8], and hence we use the term "ADM formalism" to refer to their system.

In the ADM formalism, all dynamical tensor objects exist as 3-dimensional "spatial" tensors on each spacelike hypersurface, and are provided with "time derivative" quantities which connect spatial tensors on one hypersurface to those on the next hypersurface. The coordinate freedom is expressed in terms of the *lapse* α and

9
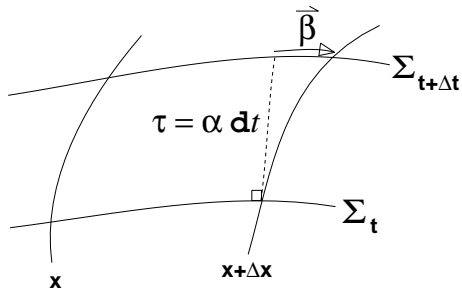
Figure 2.1: A schematic of the 3+1 decomposition. Here we show a 1+1 dimensional subset of the full spacetime, in which the time coordinate t advances roughly vertically, and the spatial coordinate x advances in an essentially horizontal direction. The surfaces Σ_t and $\Sigma_{t+\Delta t}$ define nearby surfaces of constant t. The amount of "skew" in the coordinates is given by β^i, which is called the *shift vector*. The amount of proper time τ along an interval normal to the spacelike hypersurfaces is $\tau = \alpha dt$.

the *shift vector* β^i, which are often chosen to vary with position. Figure 2.1 shows a schematic of the type of coordinates used in the ADM formalism. The lapse defines the relation between coordinate time t and the proper time τ measured by observers moving normally to the spacelike hypersurfaces; this relation is given by $\tau = \alpha dt$.

The hyperbolic character of Einstein's equation

$$G_{\mu\nu} = 8\pi T_{\mu\nu}$$

allows us to solve the equation by means of an *initial value problem*, in which we specify data on some initial spacelike hypersurface and determine the geometry of spacetime at later values of t via a set of equations of motion. Einstein's tensor equation consists of 10 equations for 10 variables. Four of these variables can be chosen arbitrarily as a result of coordinate (or "gauge") freedom. Thus we have an overdetermined system of 10 equations for six variables. Six of the equations contain second time derivatives of the 3-metric g_{ij} and are referred to as *evolution equations*. The remaining set of four equations (which do not contain second time derivatives) are *constraint equations*, which must be satisfied on each spacelike hypersurface to ensure that the evolution produces valid solutions to Einstein's equation. The

four constraints on the six evolution equations imply that there are *two* degrees of freedom in the theory, such as the two polarizations available for gravitational wave propagation.

The structure of the Bianchi identities tells us that if the initial data satisfies the constraint equations, the resulting evolution equations preserve these constraints for all time. Numerically, however, these constraints are solved imperfectly and some care must given to the specific form of evolution scheme used in a numerical simulation. The ADM formalism provides only a quasi-hyperbolic system of equations to solve. A host of explicitly hyperbolic formalisms [5, 14, 40, 41] have recently received attention, and are being implemented in numerical relativity codes [16, 57, 59, 92]. (For a review of hyperbolic formulations, see the review by Reula [83]). Nevertheless, the ADM formalism has provided the backbone for evolution codes for many years, and we will employ it (minimally) in Chapters 3 and 4 for our evolution of scalar fields in spherical symmetry.

2.1.2 Critical Phenomena

Note: Much of the discussion in this subsection is taken from a paper written with Matthew W. Choptuik [56].

Over the past decade, detailed studies of models of gravitational collapse have revealed that the threshold of black hole formation is generically characterized by special, "critical" solutions. The features of these solutions are known as "critical phenomena", and arise in even the simplest collapse models, such as a model consisting of a single real massless scalar field, minimally coupled to the general relativistic field in spherical symmetry [24]. Although we present here a brief overview of black hole critical phenomena, we suggest that interested readers consult the excellent reviews by Gundlach [45, 46] for many additional details.

The impetus for the pioneering study of critical behavior came from

Christodoulou who, in the course of his analytic studies of the Einstein-Massless-Klein-Gordon system in spherical symmetry (*cf.* [31, 32]) posed the following question [25]: Consider a generic smooth one-parameter family of initial data, such that for large values of the parameter p a black hole is formed, and for small values of p no black hole is formed. If one performs a bisection search to obtain the critical value $p^\star$ for which black hole is just barely formed, will this black hole have finite or infinitesimal mass? Choptuik was able to demonstrate, using sophisticated numerical techniques, that for a massless scalar field, the answer to this question is the latter. In so doing, he observed that all families of initial data near the critical point evolve to a single solution, term the "critical solution", which serves as intermediate attractor.

In subsequent studies carried out since then, it has invariably turned out that the solutions which appear in the strongly-coupled regime of the calculations (i.e. the critical solution), are almost totally *independent* of the specifics of the particular family used as a generator. In fact, the only initial-data dependence which has been observed so far in critical collapse occurs in models for which there is more than one distinct black-hole-threshold solution. In this sense then, black hole critical solutions are akin to, for example, the Schwarzschild solution, which can be formed through the collapse of virtually any type and/or shape of spherically distributed matter. In particular, like the Schwarzschild solution, black hole critical solutions possess additional symmetry (beyond spherical symmetry) which, to date, has either been a time-translation symmetry, in which the critical solution is static or periodic, or a scale-translation symmetry (hometheticity), in which the critical solution is either continuously or discretely self-similar (CSS or DSS).

However, in clear contrast to the Schwarzschild solution, black hole threshold solutions are, by construction, *unstable*. Indeed, after seminal work by Evans and Coleman [38] and by Koike et al [64], we have come to understand that critical

solutions are in some sense *minimally* unstable, in that they tend to have precisely one unstable mode in linear perturbation theory. Thus letting $p \to p^\star$ amounts to minimizing or "tuning away" the initial amplitude of the unstable mode present in the system.

Christodoulou's question identified two distinct possibilities for black hole threshold phenomena, and both types have been observed. Which type is observed depends in general upon the type of matter model *and* the initial data used— some models exhibit both types of critical behavior. Historically, Choptuik termed these Type I and Type II solutions, in a loose analogy to phase transitions in statistical mechanics, but at least at this juncture, we could equally well label the critical solutions by their symmetries (i.e. static/periodic or CSS/DSS) . For Type I solutions, there is a finite minimum black hole mass which can be formed, and, in accord with their static/periodic nature, there is a scaling law, $\tau \sim -\gamma \ln |p - p^\star|$, relating the lifetime, τ, of a near-critical solution to the proximity of the solution to the critical point. Here γ is a model-specific exponent which is the reciprocal of the real part of the eigenvalue associated with the unstable mode. On the other hand, Type II critical behavior—less relevant to the current study—is characterized by arbitrarily small black hole mass at threshold, and critical solutions which are generically *self-similar*.

The direct construction, or simulation, of critical solutions, has thus far been performed almost exclusively within the *ansatz* of spherical symmetry. In the spherical case one *must* couple to at least one matter field for non-trivial dynamics, and spherically symmetric critical solutions for a considerable variety of models have now been constructed and analyzed. In addition to the massless scalar case mentioned above, these include solutions containing a perfect fluid [38, 74], a scalar non-Abelian gauge field [30], and particularly germane to the current work, a *massive* real scalar field [15]. The work of Abrahams and Evans [2], which considered

13

axisymmetric critical collapse of gravitational waves, remains notable for being the only instance of a reasonably well-resolved non-spherical critical solution. (Studies involving Brill waves in three dimensions have demonstrated the existence of super-critical and sub-critical solutions, however isolation and study of the critical solutions *per se* will require considerably more resolution than that used in those studies. See [4, 10].)

In Chapter 3, we will discuss critical phenomena associated with a massive complex scalar field, which is observed when a boson star is "perturbed" by a finely-tuned pulse of massless real scalar field.

2.1.3 The Kerr Solution

In Chapter 6, we will consider the dynamics of a compled scalar field coupled to an electromagnetic field, both evolving in a (background) Kerr spacetime. The Kerr solution is a stationary, axisymmetric vacuum solution to the Einstein equation. That is, the Kerr solution possesses two Killing vector fields, one timelike and the other a "rotational" spacelike vector field. In essence, it describes the spacetime of a uncharged, rotating black hole. The more general Kerr-Newman solution allows for the inclusion of a net electric charge on the black hole, however such generality is not thought to be necessary for astrophysical applications, since any charge separation is expected to be quickly neutralized via the attraction of oppositely-charged matter.

Typically one sees the Kerr line element written in Boyer-Lindquist (BL) coordinates:

$$
\begin{aligned}
ds^2 = \quad & - \frac{\Delta - a^2 \sin^2 \theta}{\varrho^2} dt^2 - 2a \frac{2Mr \sin^2 \theta}{\varrho^2} dt d\varphi \\
& + \frac{\varrho^2}{\Delta} dr^2 + \varrho^2 d\theta^2 + \frac{\Sigma}{\varrho^2} \sin^2 \theta d\varphi^2,
\end{aligned}
\tag{2.1}
$$

where

$$
\Delta \equiv r^2 - 2Mr + a^2,
\tag{2.2}
$$

$$\varrho^2 \equiv r^2 + a^2 \cos^2 \theta, \tag{2.3}$$

$$\Sigma \equiv (r^2 + a^2)^2 - a^2 \Delta \sin^2 \theta, \tag{2.4}$$

M is the mass of the hole and a the black hole angular momentum per unit mass. We will only be considering the range $a^2 \leq M^2$.

Kerr-Schild coordinates

Kerr-Schild (KS) coordinates are a "rotational" analogue of the well-known Ingoing Eddington-Finkelstein (IEF) coordinates. KS coordinates can be obtained by transforming the BL coordinates t and φ into the KS coordinates $\tilde{t}$ and $\tilde{\varphi}$ according to:

$$d\tilde{t} + dr = dt + \frac{2Mr + \Delta}{\Delta} dr$$

$$d\tilde{\varphi} = d\varphi + \frac{a}{\Delta} dr \,.$$

Thus we arrive at the Kerr line element in KS form:

$$\begin{aligned}
ds^2 = & -\left(1 - \frac{2Mr}{\varrho^2}\right) d\tilde{t}^2 - \frac{4Mar}{\varrho^2} \sin^2 \theta d\tilde{t} d\tilde{\varphi} + \frac{4Mr}{\varrho^2} d\tilde{t} dr + \left(1 + \frac{2Mr}{\varrho^2}\right) dr^2 - \\
& 2a\left(1 + \frac{2Mr}{\varrho^2}\right) \sin^2 \theta dr d\tilde{\varphi} + \varrho^2 d\theta^2 + \sin^2 \theta \left[\varrho^2 + a^2 \left(1 + \frac{2Mr}{\varrho^2}\right) \sin^2 \theta\right] d\tilde{\varphi}^2 \,.
\end{aligned} \tag{2.5}$$

Unlike the BL coordinates typically used for studies of astrophysical black holes, KS coordinates have no coordinate singularity at the event horizon. KS coordinates are an example of a "horizon-adapted coordinate system" [39, 77].

For a brief discussion of some properties of the Kerr solutions, we follow d'Inverno [37]. The Kerr solution possesses two event horizons, $r_\pm$ and two surfaces of infinite redshift, $S_\pm$. The event horizons occur where the surfaces of constant r become null, which corresponds to where g^{rr} is zero. From this we find the event

horizons are given by roots of

$$\Delta = r^2 - 2Mr + a^2 = 0,$$

which are

$$r_\pm = M \pm \left(M^2 - a^2\right)^{1/2}. \tag{2.6}$$

So the event horizons are always surfaces of constant r, but have smaller radii for larger values of a. (Again, we are only interested in the regime $a^2 \leq M^2$.) Since we will be concerned with solutions exterior to the black hole, we will only need to retain the outer event horizon, and will simply refer to r_+ as the "event horizon."

The location of surfaces of infinite redshift are found where the t-t component of the metric is zero [37]. Inspecting the metric (2.5), we see that this occurs for $\varrho^2 - 2Mr = 0$. This gives us two roots in r,

$$r_{S_\pm} = M \pm \left(M^2 - a^2 \cos^2\theta\right)^{1/2}. \tag{2.7}$$

Thus, as the black hole spin increases, the surface of infinite redshift is "pinched" along the axis of rotation, as shown in in Figure 2.2.

The region between r_+ and S_+ is called the *ergosphere*, in which the asymptotic time translation Killing field $\xi^\mu = (\partial/\partial t)^\mu$ becomes spacelike [100]. In this region, an observer cannot remain stationary with respect to observers at spatial infinity, but must orbit in the direction of the black hole's rotation. For this reason, S_+ is also known as the *stationary limit surface*. The ergosphere allows for some interesting physics, because in this region the energy of a test particle is not necessarily positive. Penrose [80] was the first to point out that, in principle, this implies that energy can be mechanically extracted from the spin of the black hole.

2.1.4 The Membrane Paradigm

The Membrane Paradigm (MP) is a view of black holes intended for applications in astrophysics. It was set out by a series of papers in the late 1970's and early
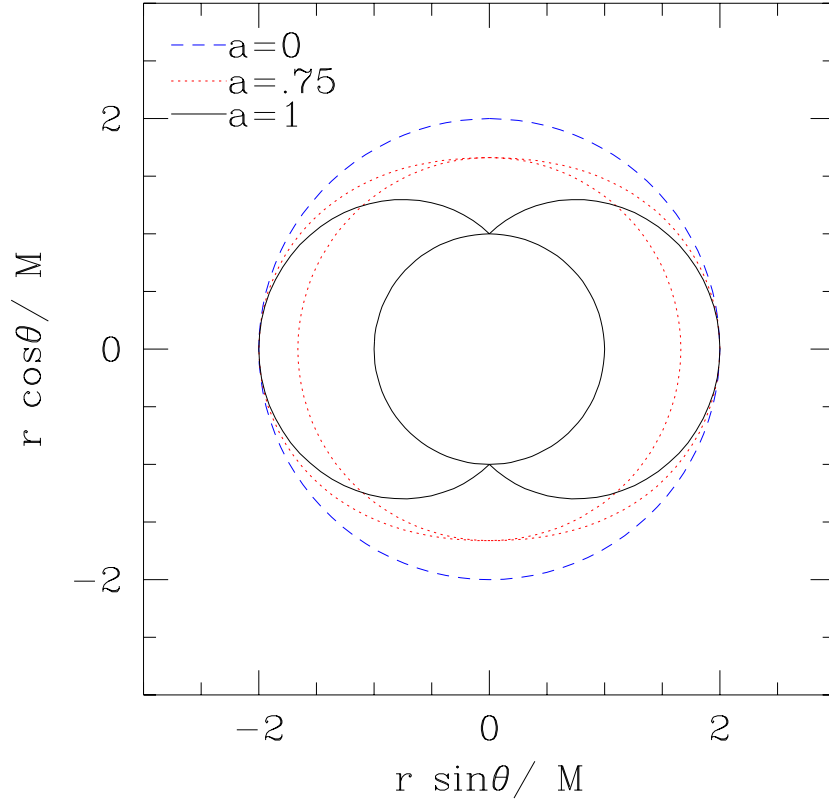
Figure 2.2: Locations of $r+$, the outer event horizon, and S_+, the outer surface of infinite redshift, for three values of a. For $a = 0$ (dashed lines), r_+ and S_+ are both spherical, and coincide. As a increases, r_+ decreases and S_+ becomes more oblate, extended out from r_+ at the equator but coinciding with r_+ at the poles. We show data for two nonzero values of a, $a = 0.75$ (dotted line) and $a = 1$ (solid line), in which the event horizon is the circle on the interior, and S_+ is shown by the curve exterior to the circle.

1980's, and presented cohesively in a book [99]. We will not attempt to go into the mathematical details of the MP, but we mention it because of its significance for astrophysics, for its particular utility in describing the Blandford-Znajek process of section 2.3.2, which we hope to simulate in the future as goal of the scalar accretion study presented in Chapter 6.

In the MP, one considers a boundary layer slightly outside the event horizon to be a material surface, having properties such as electrical resistivity, surface current and charge, temperature and entropy. While it is intended to serve principally as an aid to intuition regarding physical processes in black hole astrophysics, the MP is mathematically rigorous and offers an description *identical* to that provided by the usual curved-spacetime viewpoint, for the region of spacetime exterior to a black hole. (Inside the event horizon, however, the MP completely lacks meaning.)

It is worth noting that the mental images and terminology we use to communicate certain scientific concepts can have a significant impact on the physical intuition we have, and on the sorts of questions we ask in research.

Prior to the mid-1960's, the objects we now refer to as "black holes" were often called "frozen stars." This name arose because, for stationary observers watching the collapse of a star, the evolution would appear to slow down as the gravitational redshift increased, and the evolution would apparently stop when the star reached an "infinite redshift surface." Such an object would forever be "frozen" from the point of view of distant observers. It was known from the previous work of Oppenheimer and Snyder [76] that observers freely falling with the star would see no such "freezing", but rather would rather see the collapse right up until the (and their) very end, when they arrived at the curvature singularity. The term *collapsed star* was used to describe the physics from the "comoving view" of Oppenheimer and Snyder. However, this comoving view was not seen as being relevant for astrophysical applications, because nothing *inside* the surface of infinite redshift could ever

influence the physics *outside.* The "frozen star" viewpoint prevented physicists from realizing that black holes can be dynamical objects which can pulsate, radiate and release energy [98].

Later, the "black hole viewpoint" became popular with the advent of global analysis of black hole spacetimes, in which coordinate systems such as those introduced by Eddington and Finkelstein, rather than Schwarzschild coordinates, became systems of choice for descriptions of stellar collapse. The conformal diagrams popularized by Penrose [79, 81] served as powerful illustrations of the global properties of black hole spacetimes. Rather than "frozen stars", black holes were seen as regions of spacetime from which nothing could get out, and the surface of infinite redshift was given the name "horizon" to describe the disconnectedness of the spacetime inside the Schwarzschild radius from the outside world. Hawking and others provided theorems regarding certain aspects of the dynamics of the horizon. All of the mathematics associated with the "black hole viewpoint" were equivalent to the mathematics of the "frozen star" viewpoint, yet the use of the former charted a course of research that the latter could not provide.

Somewhat later, it was noted that the influence of a nearby gravitating body can distort the horizon of a black hole, and also that a nearby electric charge can produce a change in the fields in the vicinity of the hole *just as if* there were a charge separation (*i.e.* electrical polarization) induced on the horizon itself [48]. Further work filled in more ways in which electromagnetism in the vicinity of the horizon can be likened, even mapped, to the physics nearby a material membrane, having properties like resistivity and surface current [36], and temperature [50].

We will employ the Membrane Paradigm only briefly in this dissertation, to help provide an intuitive understanding of the Blandford-Znajek process (Section 2.3.2), however we re-emphasize that this paradigm provides a view of black holes which is helpful to astronomers in a wide variety of applications.

2.2   Finite Difference Methods

This thesis deals with the application of finite difference techniques. There are many other numerical methods available to researchers; most commonly, spectral methods and finite element methods. Finite difference methods can often be simpler to implement than other methods, particularly for solving systems of equations on a domain with regular boundaries. We present here a brief overview of some relevant aspects of finite difference methods.

Difference Operators

We construct finite difference operators via Taylor expansion in the mesh spacing. For example, suppose we wish to solve the transport equation,

$$\partial_t u = \partial_x u,$$

on a grid using finite difference techniques. This equation also admits closed-form analytic solutions which makes it a useful test case. Instead of the actual solution $u(t, x)$ to the continuum equations, we work with $\hat{u}_j^n$, the solution to the finite difference equations. We desire that $\hat{u}_j^n$ is very nearly the same as $u(n\Delta t, j\Delta x)$ for all n and j, but ensuring some level of accuracy in our finite difference solution requires that we maintain some level of accuracy in the finite difference equations themselves. Consider the partial derivative $\partial_x u$. A finite difference approximation for this might be

$$\frac{\hat{u}_{j+1}^n - \hat{u}_{j-1}^n}{2\Delta x}. \tag{2.8}$$

How accurate of an finite difference expression is this? Let us construct two Taylor expansions about $u(t = n\Delta t, x = j\Delta x)$:

$$\hat{u}_{j+1}^n = u(t, x) + \Delta x \partial_x u(t, x) + 1/2 \Delta x^2 \partial_x^2 u(t, x) + O(\Delta x^3) \tag{2.9}$$

$$\hat{u}^n_{j-1} \quad = \quad u(t, x) - \Delta x \partial_x u(t, x) + 1/2\Delta x^2 \partial_x^2 u(t, x) + O(\Delta x^3) \qquad (2.10)$$

$$(2.11)$$

Subtracting the second equation from the first and dividing by $2\Delta x$ gives us

$$\frac{\hat{u}^n_{j+1} - \hat{u}^n_{j-1}}{2\Delta x} = \partial_x u(t, x) + O(\Delta x^2).$$

We label the accuracy of an operator by the order of the terms which are neglected in the expansion, and thus we say that (2.8) is *second order accurate.*

Convergence

We would like some assurance that the solutions we obtain from the finite difference code are actually good approximations to the solutions of the continuum equations. As we decrease characteristic size h of the mesh spacing, the grid functions come closer to defining quantities on a continuum, and the finite difference operators approach the partial derivatives. Thus we expect the finite difference solutions to *converge* to the "true solutions" in the limit $h \to 0$.

In his 1910 paper, L.F. Richardson [85] described the relationship between the error of a finite difference calculation and the mesh spacing h. Consider a (continuum) differential system denoted by

$$Lu = f \qquad (2.12)$$

where L is some differential operator, f is a specified function, and u is the solution to the equation. Reducing this to a finite difference system involves using a finite difference approximation $\hat{L}$ of L (constructed via the Taylor expansion method mentioned above), with the corresponding $\hat{f}$ ($=f$ restricted to the mesh) and the *finite difference solution* $\hat{u}$:

$$\hat{L}\hat{u} = \hat{f}. \qquad (2.13)$$

21

We will also refer to $\hat{u}$ as a *grid function*. We then define the *truncation error* $\hat{\tau}$ to be

$$\hat{\tau} \equiv \hat{L}u - \hat{f}, \tag{2.14}$$

For centered difference operators $\hat{L}$, the truncation error will be an even power series in the mesh spacing h. The truncation error is related to the *solution error* $\hat{e} \equiv u - \hat{u}$ by

$$\hat{\tau} = \hat{L}\left(\hat{u} + \hat{e}\right) - \hat{f} = \hat{L}\hat{e}.$$

Richardson noted that, in the limit $h \to 0$ for centered difference equations, the solution error $\hat{e}$ will also appear as a even-powered series in the mesh spacing h, are related by

$$\hat{e} = h^2 e_2 + h^4 e_4 + ... \tag{2.15}$$

where e_2, e_4, *etc.* are smooth "error functions" which are *independent* of the mesh spacing. We refer to (2.15) as a *Richardson expansion*.

For problems in which the continuum solution u is not known, we cannot obtain an exact measure of the solution error or the truncation error. Using (2.15) and finite different solutions $\hat{u}^h$ and $\hat{u}^{2h}$ obtained on two different grids with spacings h and $2h$ respectively, we can obtain approximations to these error quantities:

$$\frac{\hat{u}^{2h} - \hat{u}^h}{h^2} = 3e_2 + 15h^2 e_4 + ..., \tag{2.16}$$

where the subtraction is performed on the intersection of $\hat{u}^h$ and $\hat{u}^{2h}$.

We can check the convergence of our numerical code by observing how well the solutions obey the properties of Richardson extrapolation. If the code is converging properly, then three grid functions $\hat{u}^h$, $\hat{u}^{2h}$ and $\hat{u}^{4h}$, obtained on grids with spacings h, $2h$ and $4h$, respectively, should to leading order produce the same error function e_2. Given that

$$\frac{\hat{u}^{4h} - \hat{u}^{2h}}{h^2} = 12e_2 + 15h^2 e_4 + ...,$$

22

we find proper second-order convergence when

$$\hat{u}^{4h} - \hat{u}^{2h} \simeq 4 \left(\hat{u}^{2h} - \hat{u}^{h} \right) .$$

To obtain a measure of the global convergence of the scheme, we first define the L_2 norm $||\hat{u}||_2$ to be

$$||\hat{u}||_2 = \left[\frac{1}{N} \sum_{i=1}^{N} |u_i|^2 \right]^{1/2} ,$$

where N is the number of elements (grid points) in $\hat{u}$. We then define the *convergence factor Q* as

$$Q \equiv \frac{||\hat{u}^{4h} - \hat{u}^{2h}||_2}{||\hat{u}^{2h} - \hat{u}^{h}||_2} , \qquad (2.17)$$

for which global second-order convergence is indicated by $Q = 4$.

The assumption of Richardson expandability is essential to the Berger and Oliger adaptive mesh refinement method described in Chapter 5, because we will use Richardson expansion to obtain an estimate of the local truncation error to determine where new grids should be placed.

Stability

Usually we wish to evolve from some initial state towards some final state, and would like to minimize the amount of computational work in between. One might ask the question "How large of a time step can I take?" The answer depends on the nature of the numerical scheme and the resolution of the grid. This question is closely related to the work of Courant, Friedrichs and Levy (CFL) described in [47] and [82]. The rule of thumb produced by CFL can be summed up in the following: For stability, the *numerical* domain of dependence must include the *physical* domain of dependence. Figure 2.3 shows a picture of this. Strictly speaking, this only applies to truly hyperbolic systems in which characteristics are well-defined.

For the boson star study in Chapter 3, the simulation code uses an explicit scheme called the "leapfrog" scheme, for which the CFL condition will be of im-

Stable   **Unstable**

▦ **Physical Domain of Dependence**

■ **Numerical Domain of Dependence**
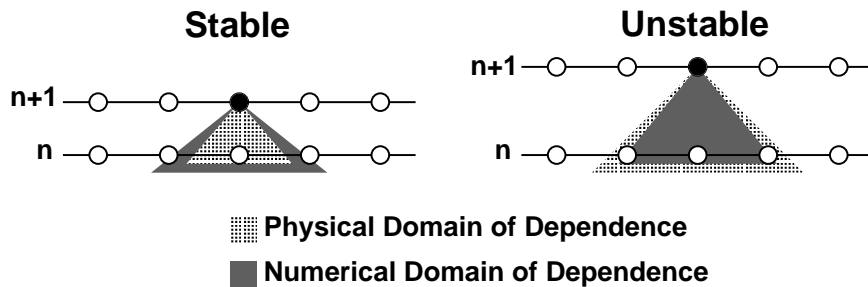
Figure 2.3: Schematic of the CFL condition. This shows an *explicit* numerical scheme, for which the numerical domain of dependence of a grid point at the advanced time level $n + 1$ (black dot) is bounded by the grid points on either side at the previous time n.

portance. For the scalar accretion study of Chapter 6, we will endeavor to use an *implicit* Crank-Nicholson method, for which the numerical domain of dependence is the entire computational (spatial) domain. A more rigorous stability consideration due to Von Neumann (described in [6]) shows the Crank-Nicholson method to be unconditionally stable.

2.3 Topics in Black Hole Accretion

2.3.1 General Review

Shakura and Zunyaev [93] presented the first significant studies of black hole accretion, in which they conceived that a gas cloud with an initial angular momentum would collapse to form an *accretion disk*, with some of the material falling into the black hole. In particular, these studies considered a model of a *thin disk*, in which the height of the disk was very small compared to the disk radius. It was previously assumed that some sort of dissipative mechanism would be active in the disk, perhaps gas viscosity or turbulence, but no one was quite clear on what the source of this dissipation should be. Shakura and Zunyaev bypassed much of this ambiguity via their "α-Model", in which the total effect of whatever dissipative mechanisms

were active in the disk could be summed up by a single viscosity parameter, which they called α. The role of magnetic fields was often neglected in early studies of accretion. For a long time the specific avenue for angular momentum conservation was a major mystery in astrophysics. Recently, John Hawley [51] has shown via three-dimensional numerical simulation that magnetohydrodynamic turbulence provides sufficient transport of angular momentum. We consider here two important processes involving magnetic fields in highly energetic astrophysical systems.

2.3.2 The Blandford-Znajek Process

In the Blandford-Znajek process [13], we have a virtual "circuit" in which magnetic fields lines threading the black hole act like wires. This mechanism is best explained via the Membrane Paradigm of section 2.1.4.

First consider a simple system in which a spinning, spherical conductor is placed in a uniform magnetic field $\vec{B} = B_z \hat{k}$. The fact that the conductor is spinning in this field means that charges will move along the surface, with an overabundance of positive charges accumulating at the equator, and an overabundance of negative charges accumulating near the poles, until some force balance is set up between the magnetic force and the induced electric force. Thus the spinning sphere becomes a battery. We can connect a resistive load to this battery by adding wires which touch and slip along the poles equator and poles as shown in figure 2.4, and drive a current through the load, thus "extracting energy" from the spinning conductor to the load.

Now instead of a typical conductor, imagine that we are dealing with the membrane-like horizon of a black hole, and instead of wires, we have magnetic field lines along which charged plasma can stream. By "hooking up" some resistive load to these "wires", we can extract energy from the induced electromotive force on the black hole horizon. This is the essence of the Blandford-Znajek process, a schematic
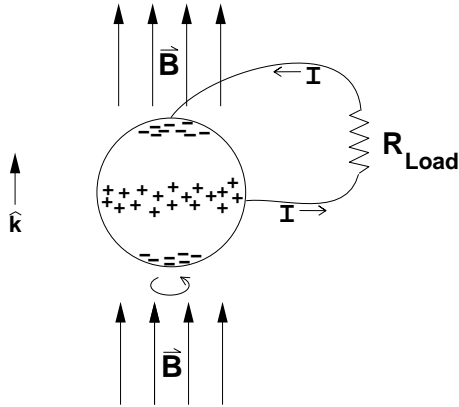
Figure 2.4: A spinning spherical conductor as a battery. The uniform magnetic field $\vec{B} = B_z \hat{k}$ induces a charge separation between the equator and poles, which when connected via wires can drive current I through a resistive load R_{Load}.

of which is shown in Figure 2.5.

Imagine that in some region close to the black hole, magnetic fields are strong enough that a force-free magnetosphere is set up, *i.e.* charges can only flow along magnetic field lines, *i.e.*

$$F_{\mu\nu} J^\nu = 0.$$

Through some process such as particle-antiparticle pair creation, we obtain a situation in which positive charges flow into the hole along the poles, and negative charges flow in at the equator.

At some distance away from the black hole, the "force-free" approximation will fail, and electric equipotential surfaces will deviate from magnetic field lines. These surfaces will "connect up" over the poles, and we will have a net electric field in the vertical direction. Blandford and Znajek speculated that the resistive "load" in this system might therefore take the form of jets of charged particles, which are accelerated via these vertical field lines. This provided a natural explanation for the highly-collimated, high-speed jets which are observed to originate near some compact astrophysical sources.
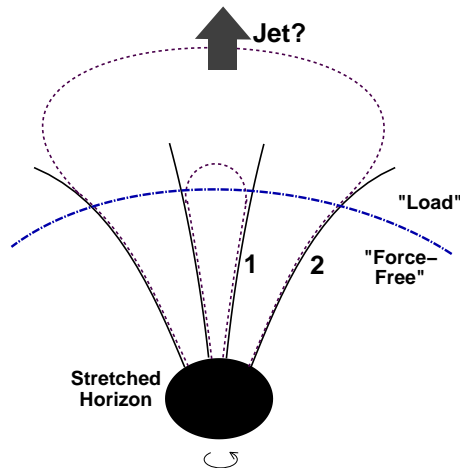
Figure 2.5: A schematic of the Blandford-Znajek mechanism. Positive charges stream inward along magnetic field line 1, and negative charges stream inward along field line 2. Equipotential surfaces are shown as dotted lines. (The author's rendering of a figure in [99].)

2.3.3 Magnetic Torques at the Marginally Stable Orbit

Early models of accretion [93], [75] were performed within the thin-disk model with what is called a "no-torque" boundary condition at the marginally stable orbit (MSO), which is generally considered to be the inner edge of the accretion disk. For the no-torque condition, fluid which reaches the MSO is assumed to freely fall into the black hole, and have no effect on the exterior part of the accretion disk. In other words, the sort of viscous torques which were assumed to be operating throughout the disk (such as in Shakura and Sunyaev's α-model) were assumed to be completely negligable at and inside the MSO. The no-torque inner boundary condition was justified via an argument that infalling gas would quickly become causally disconnected from the rest of the disk by nature of a low sound speed [75]. From this assumption, one can derive expressions for accretion efficiency (conversion of rest mass into radiation) which range from 5% for gas falling into Schwarzschild black holes to 42% for gas falling into maximally-rotating ($a^2 = M^2$) Kerr black

holes [75]. A short time ago, Charles Gammie [42] began to seriously consider the effect of magnetic fields on accretion efficiency. Gammie knew that magnetic fields could exert a torque, and that perhaps the no-torque boundary condition was not applicable to astrophysical, magnetized accretion disks. In fact, he found that the accretion efficiency can be greatly enhanced by the presence of magnetic fields, and can even exceed unity. In other words, Gammie found scenarios in which energy was being extracted from the black hole via the magnetic torque. Eric Agol and Julian Krolik further explored the implications of magnetic torques operating at the marginally stable orbit [3]. A most recent contribution on this subject is the work of J. Hawley and Krolik [53], who show via numerical simulation that there can be *significant* (magnetic) torque at the marginally stable orbit, and that this torque is in fact *continuous* across the "inner boundary" of the accretion disk. The scalar accretion study considered in Chapter 6 of this thesis was in part aimed at obtaining results regarding the significance of magnetic torques at the inner boundary. The new work by Hawley and Krolik appears to provide the answers we were originally searching for, however we still hope to find many interesting and unexpected phenomena in the charged scalar system.

Chapter 3

Critically-Perturbed Boson Stars

Note: Most of the results and discussion given in this chapter are from a paper which M.W. Choptuik and I recently submitted to Phys. Rev. D. [56].

3.1 Introduction

Our current interest is a critical-phenomena-inspired study of the dynamics associated with "boson stars" [62, 86, 34], a class of equilibrium solutions to the Einstein-Klein Gordon system for massive complex fields, which are supported against gravitational collapse by the effective pressure due to the dispersive nature of a massive Klein-Gordon field. Studies of boson stars began with the works of Kaup [62] and Ruffini and Bonnazola [86], who demonstrated that stable equilibrium configurations exist for self-gravitating massive Klein-Gordon fields. These configurations are supported against gravitational collapse by the effective pressure due to the dispersion relation of the Klein-Gordon field. Later this work was extended by Colpi *et al.* [34] to include a nonlinear self-interaction term which can give rise to an additional pressure, and can allow for larger boson stars having masses and sizes more relevant to astrophysical applications. Predictions from particle physics regarding

the existence of one or more scalar or pseudo-scalar particles kindled greater interest in the study of boson stars as astrophysical objects, perhaps as a contribution to dark matter in the universe. Some astrophysical aspects of boson stars have been investigated by Lee and Koh [66] and Dąbrowski and Schunck [35]. Stability studies of boson stars continued with Gleiser and Watkins [43], as well as Lee and Pang [67], who showed that there exists a critical value of the central density which marks the transition between boson stars which are stable with respect to infinitesimal radial perturbations and those which are not. Dynamical stability studies were carried out by Seidel and Suen [89] in which radial perturbations to equilibrium configurations were applied by adding or removing mass from a section of the star. They then solved for the resulting evolution numerically, and found that a boson star on the unstable branch will either form a black hole or radiate scalar material and form a boson star on the stable branch. They also showed that perturbed stable boson stars will oscillate with a characteristic frequency which depends on the mass of the star. Along with Balakrishna, Seidel and Suen later extended this work to include the effects of self-interacting fields and "excited" states in which the field contains one or more nodes [9]. They found that all excited states are unstable and either form black holes or radiate scalar material until a stable "ground state" (zero node) boson star is formed. Their stability study will be extended in this chapter, in which we consider large radial perturbations of a boson star which drive it to the threshold of black hole formation. For further reviews on the subject of boson stars, see Jetzer [61] or Mielke and Schunck [71].

As mentioned in Chapter 2, a paper closely related to this work is that of Brady *et al.* [15], which described a dynamical study of critical solutions of a massive real scalar field. Those authors demonstrated scenarios in which black holes could be formed with arbitrarily small mass (Type II transitions), *and* those in which the black holes formed had a finite minimum mass (Type I transitions). The boundary

between these regimes seemed to be the relative length scale of the pulse of initial data compared to the Compton wavelength associated with the boson mass. Initial data which was "kinetic energy dominated" evolved in a manner essentially similar to the evolution of a massless scalar field. Initial data pulses having widths larger than the length scale set by the boson mass were "potential dominated", providing a characteristic scale for the formation of the critical solutions. Brady *et al.* found that the resulting Type I critical solutions corresponded to a class of equilibrium solutions discovered by Seidel and Suen [90], which are called "oscillating soliton stars." These soliton stars share many characteristic with the complex-valued boson stars, such as the relationship between the radius and mass of the star. Both types of "stars" have a maximum mass, and show the same overall behavior as "real" (fermion) stars in terms of the turn-over in their respective stability curves. Interestingly, although the soliton stars are not static—they are periodic (or quasi-periodic)—many of the same macroscopic properties seen in fluid stars are still observed.

In this chapter, we construct critical solutions of the Einstein equations coupled to a massive, *complex* scalar field dynamically, by simulating the implosion of a spherical shell of *massless* real scalar field around an "enclosed" boson star. The massless field implodes toward the boson star and the two fields undergo a (purely gravitational) "collision." The massless pulse then passes through the origin, explodes and continues to $r \to \infty$, while the massive complex (boson star) field is compressed into a state which ultimately either forms a black hole or disperses. We can thus play the "interpolation game" using initial data which result in black hole formation, and initial data which give rise to dispersal: specifically, we vary the initial amplitude of the *massless* pulse to tune to a critical solution. We analyze the black hole threshold solutions obtained in this manner, and discuss the similarities between our critical solutions for the self-gravitating complex massive scalar field and boson stars on the unstable branch. To further this discussion, we extend the

work of Gleiser and Watkins [43] and compare the results of the simulations with those of linear perturbation theory.

The layout of the remainder this chapter is as follows: In Section 3.2, we describe the mathematical basis for our numerical simulations. In Section 3.3, we present results from our simulations, in which the Type I character of the critical solutions is demonstrated, along with the close similarities one finds between the features of the critical solutions and those of boson stars. In most of the critical solutions we find a halo of mass near the outer edge of the solution which is not a feature of boson star equilibrium data. Inside this halo, however, the critical solutions match the boson star profiles very well. In Section 3.4, we give a synopsis of our linear stability analysis of boson star quasinormal modes, from which we obtain the boson star mode frequencies as functions of the central value of the modulus of the complex field. Section 3.5 concerns the radial profiles of the perturbative modes *per se*, and includes a comparison of the mode shapes and frequencies obtained from perturbation theory with our simulation data. The modes obtained by these two different methods agree well with each other, although the additional oscillatory mode in our simulation data is only shown to agree with the corresponding boson star mode in terms of the oscillations in the metric and not in the field (possibly as an artifact of our simplistic approach to extracting this mode from the simulation). In Section 3.6 we provide further discussion regarding the properties of the halos surrounding the critical solutions. Conclusions are given in Section 3.7. The appendices of this dissertation give tables of mode frequencies versus the central field value of the boson star, details about our finite difference code, and details of our linear stability analysis, which includes a description of our algorithm for finding the frequencies of boson star modes.

3.2 Scalar Field Model

A boson star is described by a complex massive scalar field ϕ, minimally coupled to gravity as given by general relativity. We work solely within the context of classical field theory, and choose units in which G and c are unity. Furthermore, since all lengths in the problem can be scaled by the boson mass m [34], we choose $m = 1$. To the usual boson star model, we add an additional, massless real scalar field, ϕ_3, which is also minimally coupled to gravity. This additional scalar field will be used to dynamically "perturb" the boson star.

The equations of motion for the system are then the Einstein equation and Klein-Gordon equations:

$$G_{\mu\nu} = R_{\mu\nu} - \frac{1}{2}g_{\mu\nu}R = 8\pi\left(T_{\mu\nu}^C(\phi) + T_{\mu\nu}^R(\phi_3)\right) \tag{3.1}$$

$$\Box\phi - m^2\phi = 0 \tag{3.2}$$

$$\Box\phi_3 = 0 \tag{3.3}$$

where

$$8\pi T_{\mu\nu}^C(\phi) = \partial_\mu\phi\partial_\nu\phi^* + \partial_\mu\phi^*\partial_\nu\phi - g_{\mu\nu}\left(\partial_\sigma\phi\partial^\sigma\phi^* + m^2|\phi|^2\right), \tag{3.4}$$

$$8\pi T_{\mu\nu}^R(\phi_3) = 2\partial_\mu\phi_3\partial_\nu\phi_3 - g_{\mu\nu}\partial^\sigma\phi_3\partial_\sigma\phi_3, \tag{3.5}$$

and $\Box$ is the D'Alembertian operator. While more general potentials in (3.2) have been employed recently [9, 88], we will restrict our discussion to the simplest case, *i.e.* merely the $m^2\phi^2$ potential. We also stress that the complex scalar field, ϕ, and the massless, real scalar field, ϕ_3 are coupled *only* through gravity—in particular we do not include any interaction potential $V_I(\phi, \phi_3)$.

Restricting our attention to spherical symmetry, we write the most general spherically-symmetric metric using Schwarzschild-like "polar-areal" coordinates

$$ds^2 = -\alpha^2(t, r)dt^2 + a^2(t, r)dr^2 + r^2 d\Omega^2, \tag{3.6}$$

33

and generally make use of the "3+1" formalism of Arnowitt, Deser and Misner [8] which regards spacetime as a foliation of spacelike hypersurfaces parameterized by t (cf. Section 2.1.1.

We write the (spherically-symmetric) complex field, $\phi(t,r)$, in terms of its components

$$\phi(t,r) = \phi_1(t,r) + i\phi_2(t,r) \qquad (3.7)$$

where $\phi_1(t,r)$ and $\phi_2(t,r)$ are each real. Again, since our model includes no self-interaction (anharmonic) potential for the complex field, ϕ_1 and ϕ_2 are only coupled through the gravitational field.

We then define

$$\Phi_1(t,r) \equiv \phi_1' \qquad \Phi_2(t,r) \equiv \phi_2' \qquad (3.8)$$

$$\Pi_1(t,r) \equiv \frac{a}{\alpha}\dot{\phi_1} \qquad \Pi_2(t,r) \equiv \frac{a}{\alpha}\dot{\phi_2}, \qquad (3.9)$$

$$\Phi_3(t,r) = \phi_3' \qquad \Pi_3(t,r) = \frac{a}{\alpha}\dot{\phi_3}. \qquad (3.10)$$

where $' \equiv \partial/\partial r$ and $\dot{} \equiv \partial/\partial t$.

With these definitions, the equations we solve are the Hamiltonian constraint,

$$\frac{a'}{a} = \frac{1-a^2}{2r} + \frac{r}{2}\left[\Pi_1{}^2 + \Pi_2{}^2 + \Pi_3{}^2 + \Phi_1{}^2 + \Phi_2{}^2 + \Phi_3{}^2 + a\left(\phi_1{}^2 + \phi_2{}^2\right)\right], \quad (3.11)$$

(where $\Pi_1{}^2$ should be read as $(\Pi_1)^2$), the slicing condition,

$$\frac{\alpha'}{\alpha} = \frac{a^2 - 1}{r} + \frac{a'}{a} - a^2 r(\phi_1{}^2 + \phi_2{}^2), \qquad (3.12)$$

and the Klein-Gordon equations,

$$\dot{\Pi}_k = 3\frac{\partial}{\partial r^3}\left(\frac{r^2\alpha}{a}\Phi_k\right)' - \alpha a\phi_k(1 - \delta_{3k}), \qquad (3.13)$$

where $k = 1, 2, 3$ and δ_{3k} is a Kronecker delta used to denote the fact that ϕ_3 is a massless field.

34

We also have equations which are used to update the spatial gradients of the scalar fields, as well as the scalar fields themselves. These follow directly from the definitions (3.8) and (3.9):

$$\dot{\Phi}_k = \left(\frac{\alpha}{a}\Pi_k\right)'$$ (3.14)

$$\phi_k = \int_0^r \Phi_k \, d\tilde{r}$$ (3.15)

Equations (3.11)–(3.15) are solved numerically using the second order finite difference method described in Appendix B.

Initial conditions for our simulations are set up as follows. First, initial data for the massive field are constructed from the boson star *ansatz*

$$\phi(t, r) = \phi_0(r)e^{-i\omega t},$$ (3.16)

where we let $\phi_0(r)$ be real. Substitution of this *ansatz* into the full set of equations (3.11)-(3.15), yields a system of ordinary differential equations (ODEs), whose solution, for a given value of the central field modulus, is found by "shooting", as described in [86]. Once the boson star data is in hand, we add the perturbing massless field by freely specifying Φ_3 and Π_3. At this point, all matter quantities have been specified; the initial geometry, $a(0, r)$ and $\alpha(0, r)$ is then fixed by the constraint and slicing equations (3.11) and (3.12).

In relating the simulation results which follow, it is useful to consider the individual contributions of the complex and real fields to the total mass distribution of the space-time, in order that we can meaningfully and unambiguously discuss, for example, the exchange of mass-energy from the real, massless field to the massive, complex field. By Birkhoff's theorem, in any vacuum region, the mass enclosed by a sphere of radius r at a given time t is given by the Schwarzschild-like mass aspect function $M(t, r) = r(1 - 1/a^2)/2$. However, at locations occupied by matter, $M(t, r)$ cannot necessarily be usefully interpreted as a "physical" mass. In polar-areal coordinates, the mass aspect function is related to the local energy density

$\rho(t, r)$ by

$$\frac{\partial M(t, r)}{\partial r} = r^2 \rho(t, r), \tag{3.17}$$

with $\rho(t, r)$ given in our case by

$$\rho(t, r) = \frac{1}{2a^2} \left[\Pi_1{}^2 + \Pi_2{}^2 + \Phi_1{}^2 + \Phi_2{}^2 + a^2 \left(\phi_1{}^2 + \phi_2{}^2 \right) \right] + \frac{1}{2a^2} \left[\Pi_3{}^2 + +\Phi_3{}^2 \right]. \tag{3.18}$$

Here, we have explicitly separated the contributions from the complex and real fields. Since $\partial M / \partial r$ is given by a linear combination of the contributions from each field, we can decompose $\partial M / \partial r$ so that, in instances where there is no overlap in the supports of the distinct fields, we can unambiguously refer to the mass due to one field or the other. That is, we can refer to the individual contributions of each field to the total mass as being physically meaningful masses in their own rights. Then, by integrating the contribution of *each* field to $\partial M / \partial r$ over some range of radius $(r_{\min} \cdots r_{\max})$, (where there is *some* region of vacuum starting at $r_{\min}$ and extending inward, and *some* region of vacuum starting at $r \geq r_{\max}$ and extending outward), and demanding that none of the other type of field is present in the domain of integration, we can obtain a measure of the mass due to each field.

Motivated by such considerations, we define an energy density for the complex field, ρ_C, as

$$\rho_C(t, r) = \frac{1}{2a^2} \left[\Pi_1{}^2 + \Pi_2{}^2 + \Phi_1{}^2 + \Phi_2{}^2 + a^2 \left(\phi_1{}^2 + \phi_2{}^2 \right) \right], \tag{3.19}$$

with a corresponding mass aspect function, $M_C(t, r)$, given by

$$M_C(t, r) = \int_0^r \tilde{r}^2 \, \rho_C \, d\tilde{r} \,. \tag{3.20}$$

Similarly, the energy density due to the real field is defined as

$$\rho_R(t, r) \equiv \frac{1}{2a^2} \left[\Pi_3{}^2 + +\Phi_3{}^2 \right], \tag{3.21}$$

with a corresponding mass aspect function, $M_R(t, r)$ given by

$$M_R(t, r) = \int_0^r \tilde{r}^2 \, \rho_R \, d\tilde{r}.$$

We again emphasize that in regions where the supports of the different fields overlap (and in non-vacuum regions in general) it may not be possible to ascribe physical meaning to the individual mass aspect functions defined above. (However, even in such instances, these functions are still useful diagnostics.) Most importantly, where the supports of the fields *do* overlap, and only in these regions, it is possible for mass-energy to be exchanged from one scalar field to the other—*through the gravitational field*—while the sum $M_C + M_R = M$ (measured in an exterior vacuum region) is conserved. The quantities given above allow us to measure this exchange of mass by looking at the profiles $M_C(t, r)$ and $M_R(t, r)$ before and after a time when the fields are interacting. This is shown in the next section.

As a further consideration, we point out that the $U(1)$ symmetry of the complex field implies that there is a conserved Noether current, J^μ, given by

$$J^\mu = \frac{i}{8\pi} g^{\mu\nu} (\phi \partial_\nu \phi^* - \phi^* \partial_\nu \phi). \tag{3.22}$$

The corresponding conserved charge or "particle number" N is

$$N = \int_0^\infty r^2 \sqrt{-g} J^t.$$

We may also wish to regard N as a function of t and r by integrating the above function from zero to some finite radius, in which case

$$\frac{\partial N(t, r)}{\partial r} = r^2 \left(\Pi_1 \phi_2 - \Pi_2 \phi_1 \right). \tag{3.23}$$

Some authors have considered the difference $M_C - mN$ to be a sort of "binding energy" of the complex field [61], however this quantity does not correspond to any transition in the stability of boson stars, and we have not found it to be very useful in understanding the dynamics of our simulations.

Finally, following Seidel and Suen [89], we define a radius $R_{95}(t, r)$ for the boson star implicitly by $M_C|_{R_{95}} = 0.95\, M_C|_{r \to \infty}$. Alternatively, we will also consider a radius $R_{63}(t, r)$ which encloses $(1 - e^{-1}) \sim 63\%$ of $M_C|_{r \to \infty}$, and which will include the "bulk" of a boson star but will neglect the "tail".

3.3   Simulation Results

We choose the initial data for the complex field to be a boson star at the origin, with a given central density $\phi_0(0)$. For the massless field $\phi_3(0, r)$, we choose one of the families in Table 3.1. We generate critical solutions by tuning the amplitude A of $\phi_3(0, r)$ (holding the position r_0 and width Δ constant) using a bisection search, until the resulting solution is arbitrarily close (i.e. within some specified precision) to the point of unstable equilibrium between dispersal and black hole formation.

Figure 3.1 shows a series of snapshots from a typical simulation in which the parameter p ($p \equiv A$), is slightly below the critical value $p^\star$, for a boson star on the stable branch with a mass of $M = 0.59 M_{Pl}^2/m$, where M_{Pl} is the Planck mass. (The boson mass m has units of inverse length, so the corresponding physical mass is $m\hbar/c$, and we use $\hbar = 1$.) The shell of massless field, a member of initial data Family I, implodes through the boson star and explodes back out from the origin, and the gravitational interaction between the fields forces the boson star into a new state, a "critical solution." We see from this animation, and from Figure 3, that dispersal from the critical state does not mean that the boson star returns to its original stable configuration, but rather that the star becomes strongly disrupted and "explodes." That is to say, if we were to follow the evolution beyond $t = 475$, the massive field would continue to spread toward spatial infinity. At some late time, after a large amount of scalar radiation has been emitted, the end state would probably be a stable boson star with very low mass.

The gravitational interaction between the two fields results in an exchange of energy from the massless field to the massive field, as shown in Figure 3.2. Figure 3.3 shows some timelike slices through the simulation data, giving a plot of the maximum value of a, the value of $|\phi|$ at the origin, and the radius R_{95} as functions of time. These are given to help elucidate the point that the critical solution oscillates about some local equilibrium, before dispersing or forming a black hole. The lifetime of
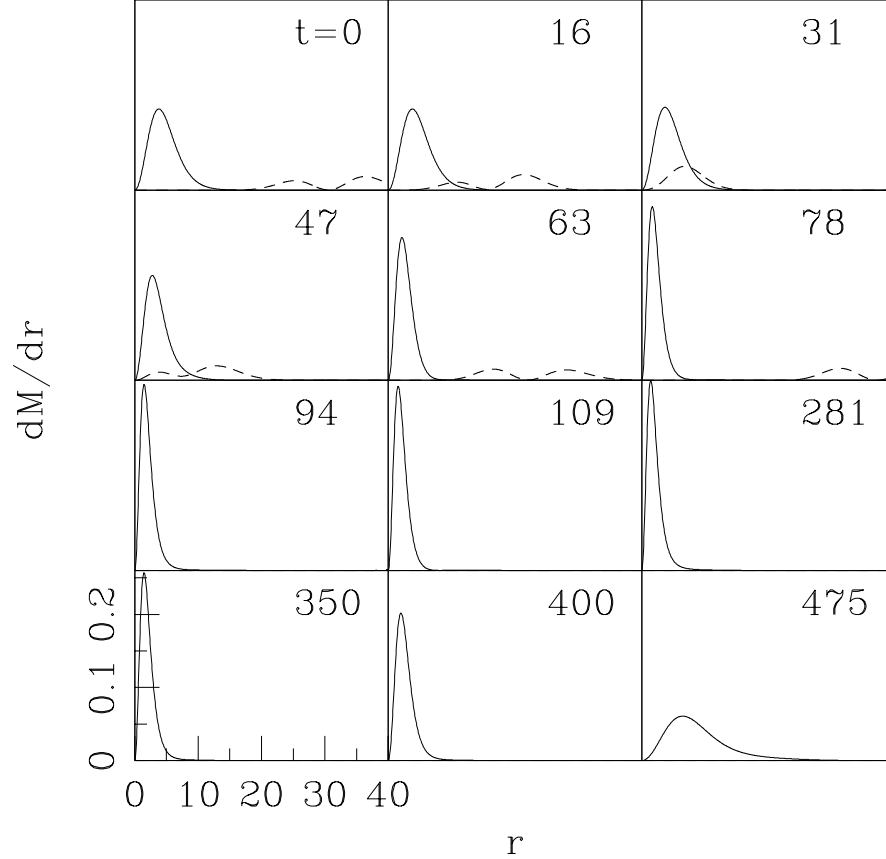
Figure 3.1: Evolution of a perturbed boson star with $\phi_0(0) = 0.04 \times \sqrt{4\pi}$ and mass $M_C = 0.59 M_{Pl}^2/m$. This shows contributions to $\partial M/\partial r$ due to the massive field (solid line) and massless field (dashed line). We start with a stable boson star centered at the origin, and a pulse of massless field given by Family I with $r_0 = 30$ and $\Delta = 8$. (We see two peaks in dM/dr of massless field because it is only the gradients of ϕ_3, not ϕ_3 itself, which contribute to $M_R(r, t)$ for a massless field.) In the evolution shown above, the pulse of massless field enters the region containing the bulk of the boson star ($t \simeq 15$), implodes through the origin ($t \simeq 30$) and leaves the region of the boson star ($t \simeq 50$). Shortly after the massless pulse passes through the origin, the boson star collapses into a more compact configuration, about which it oscillates for a long time before either forming a black hole or dispersing. (The case of dispersal is shown here.) Note that the perturbing field ϕ_3 passes through the boson star and exits the region containing most of the star, even before the massive field reaches its denser, critical state. Thus the massless field is *not* part of the critical solution *per se*. Black hole formation (always with a finite black hole ADM mass in our study) can take place at times long after the massless pulse has left the neighborhood of the boson star.

39

Table 3.1: Families of initial data. For both families, the initial data, $\phi(0, r) = \phi_1(0, r) + i\phi_2(0, r)$, for the massive complex field is given by a boson star, obtained by solving (3.11)–(3.13) numerically according to the *ansatz* (3.16) (with the parameter ω found via "shooting"). The initial real massless field profile, $\phi_3(0, r)$, is given in closed form by the "gaussian" and "kink" initial data. For each family, we also choose $\partial_t \phi_3(0, r)$ such that the pulse is initially in-going, i.e. $\Pi_3(0, r) = \Phi_3(0, r) + \phi_3(0, r)/r$.

Family	Complex Field $\phi_1 + i\phi_2$			Real Field ϕ_3		
	Name	Parameters	Profile	Name	Parameters	Profile
I	Boson Star	$\phi_0(0)$	$\phi_0(r)$	Gaussian	A, r_0, Δ	$A \exp\left(-\left(\dfrac{r - r_0}{\Delta}\right)^2\right)$
II	Boson Star	$\phi_0(0)$	$\phi_0(r)$	Kink	A, r_0, Δ	$\dfrac{A}{2}\left(1 + \tanh\left(\dfrac{r - r_0}{\Delta}\right)\right)$

the critical solution increases monotonically as $p \to p^\star$. Figure 3.4 shows that the scaling law expected for Type I transitions is exhibited by these solutions.

Figure 3.5 shows the mass *vs.* radius for some critical solutions along with the equilibrium curve for boson stars. We notice that there are great similarities, at least for relatively high mass configurations, between the critical solutions and unstable boson stars in the ground state. (We do not perform studies involving boson stars with much lower masses, because of the dynamic range required for the spatial resolution of the finite difference code. Also, for a given $|p - p^\star|$, such low-mass critical solutions have much shorter lifetimes than larger-mass solutions; thus it can be more difficult to measure time-averaged properties.) When we include nearly all of the complex-scalar mass in our comparisons, as shown in Figure 3.5(a), we see that the time-averaged properties of the critical solutions with lower masses, *i.e.* those further from the transition to instability, deviate from the curve of equilibrium configurations, and that the deviation increases as mass decreases. When we consider only the bulk of the boson star, however, we see very good agreement between the dynamically generated critical solutions and the unstable boson stars, computed from the static *ansatz*, as shown in Figure 3.5(b). The comparison between low-mass
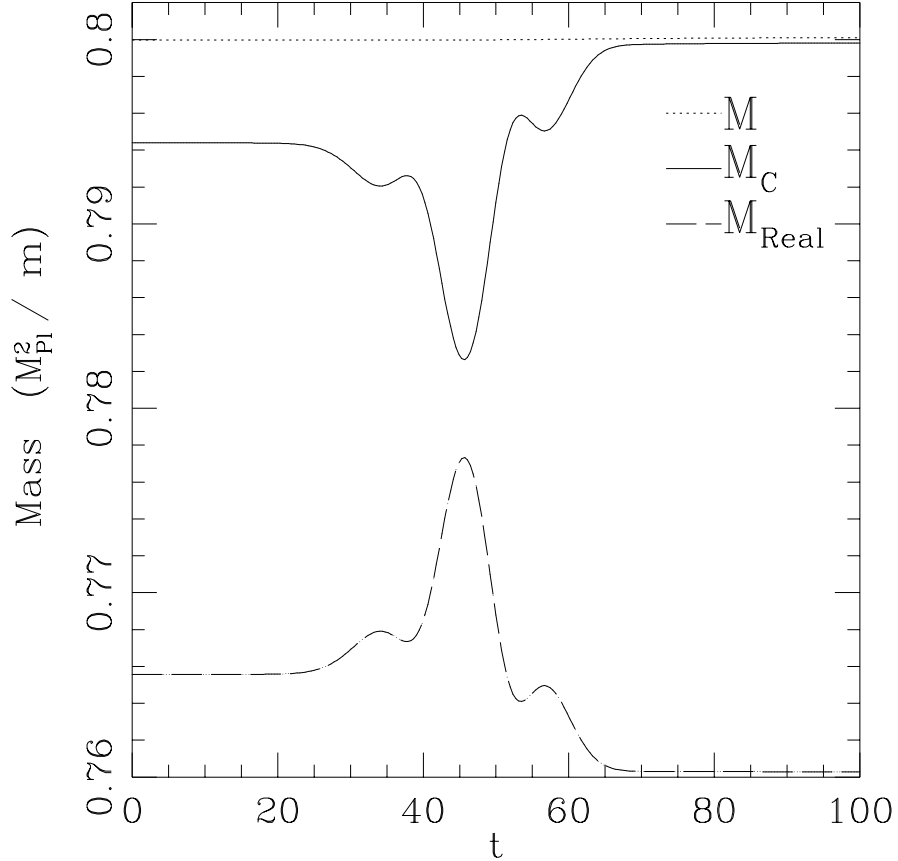
Figure 3.2: Exchange of energy between the real and complex scalar fields. For this simulation, initial data from Family I was used, with $\phi_0(0) = 0.04 \times \sqrt{4\pi}$, $r_0 = 40$ and $\Delta = 8$. The solid line shows the mass of the complex field, shifted upward on the graph by $0.21 M_{Pl}^2/m$. The long-dashed line shows the mass of the real field, shifted upward by $0.55 M_{Pl}^2/m$. The mass ΔM exchanged from the massless field to the massive field in this simulation is nearly 0.0053, or about 2.5% of the mass of the real field (9% of the boson star mass). The amount (and percentage) of mass transfer goes to zero as we consider boson star initial data approaching the transition to instability (see, e.g. Figure 7). The dotted line near the top of the graph shows the total mass enclosed within $r = 100$. Throughout the simulation, both the total mass $M = M_C + M_R$ and the particle number N (of the complex field) are conserved to within a few hundredths of a percent.

41
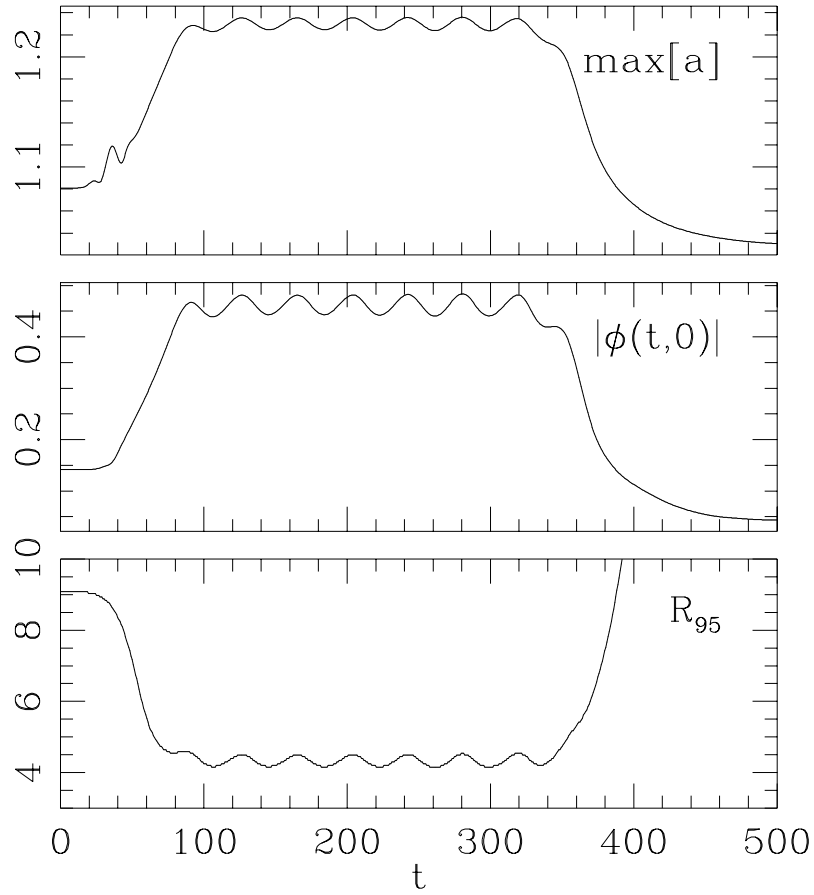
Figure 3.3: Quantities describing a near-critical solution. Here we show timelike slices through the data shown in Figure 3.1, an evolution that ends in dispersal. Top: Maximum value of the metric function a (for each spacelike hypersurface parameterized by t). The local maximum at $t \simeq 40$ is due to the presence of the pulse of massless field. Middle: Central value $|\phi(t,0)|$ of the massive field. Bottom: Radius R_{95} which contains 95% of the mass-energy in the complex field. Again, we see evidence that after the remaining in critical regime for a while, the star can "explode", leaving a diffuse remnant with low mass.
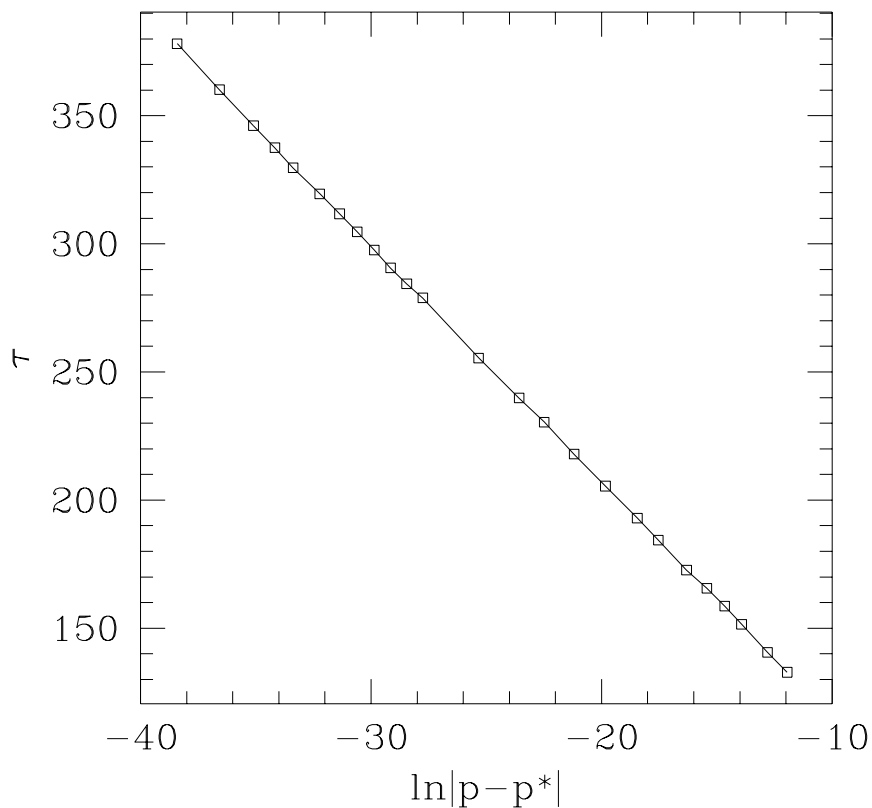
Figure 3.4: Lifetime τ of a typical set of near-critical solutions *vs.* $\ln|p - p^\star|$. We use initial data from Family I. The lifetime of the critical solution obeys a simple scaling relation. Using super-critical solutions, we measure τ to be the time from $t = 0$ until black hole formation occurs. The relationship shown in the graph can be described by $\tau = -\gamma \ln|p - p^\star|$, where for the data shown in this graph, $\gamma \simeq 9.2$ The value of γ can be related to the imaginary part of the Lyapunov exponent σ of the unstable mode ($\sim e^{i\sigma t}$) by $\Im(\sigma) = 1/\gamma \simeq 0.109$. This value is the same as that obtained from a linear perturbation analysis of the specific boson star to which we believe this configuration is asymptoting (See Section 3.5). We note that in the limit $p \to p^\star$, the mass of the black hole formed is finite (and close to the mass of the progenitive unstable boson star), *i.e.* the system exhibits Type I critical behavior.

43
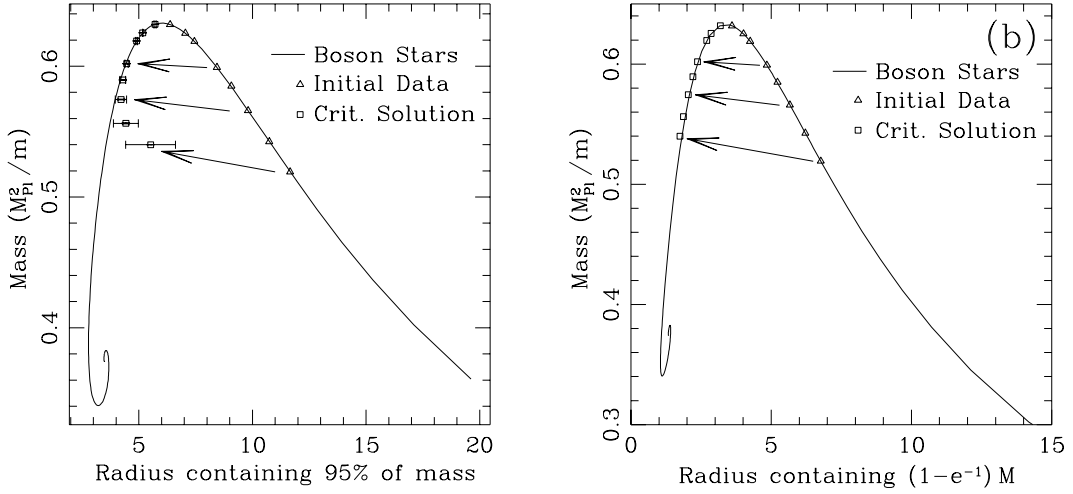
Figure 3.5: Mass *vs.* radius for equilibrium configurations of boson stars (solid line), initial data for the complex field (triangles), and critical solutions (squares). Arrows are given to help match initial data with the resulting critical solutions. Points on the solid line to the left of the maximum mass $M_{\mathrm{max}} \simeq 0.633 M_{Pl}^2/m$ correspond to unstable boson stars, whereas those to the right of the maximum correspond to stable stars. If one takes time averages of properties such as mass, central density $|\phi(t, 0)|$ and radius R_{95} during the critical regime, one finds values which match the profile of a boson star on the unstable branch. The squares show the time average of each critical solution during the oscillatory phase. Graph (a) shows mass M versus R_{95} the radius containing 95% of M, whereas graph (b) shows M versus the radius containing $(1 - e^{-1}) M$. The agreement between the critical solutions and boson stars shown in graph (a) deteriorates with decreasing mass, however the comparison shown in graph (b), which neglects the "tail" of the critical solutions and boson stars, shows much better agreement for all masses. (We show the tail region in Figure 3.6.) In this simulation the massive field radiates only a small amount due to the perturbation by the massless field, and so the stable boson star is essentially driven to "pop" across the stability curve by the impinging massless pulse.

44

critical solutions and boson stars, shown in Figure 3.5, can be further illuminated by looking at a profile of the mass distribution as shown in Figure 3.6.

We see that there is a small halo near the outer edge of the solution ($r = 8$), and it is this which throws off our measurement of R_{95} used for Figure 3.5. Despite the effect this has on the measurement of the radius R_{95} of the star, we can still obtain a good fit of a boson star to the interior of the critical solution in the low-mass regime. We provide further discussion of these halos in Section 3.6.

It is also worth noting that the critical solution best corresponds to a boson star in the "ground state", *i.e.* a solution without any nodes in the distribution of the fields ϕ_1 or ϕ_2. Boson stars in excited states (*i.e., having* nodes in ϕ_1 and ϕ_2) have mass distributions which differ significantly from the critical solutions we obtain [9].

We wish to explain these simulation results in terms of the quasi-normal modes of boson stars. Previous work in critical phenomena [15, 24, 30, 38, 45, 46, 64, 74] leads us to surmise that there is a single unstable mode present in the system which is excited when the boson star moves into the critical regime. The oscillatory behavior during the critical regime may be explainable in terms of the superposition of a stable oscillatory mode with the unstable mode. In the next section, we attempt to confirm these hypotheses by means of perturbation theory.

3.4   Boson Star Stability Study via Linear Perturbation Theory

We follow the work of Gleiser and Watkins [43]. For the perturbation calculations, we find it helpful to define the following metric functions:

$$
\begin{aligned}
e^{\nu(t,r)} &\equiv \alpha^2 \\
e^{\lambda(t,r)} &\equiv a^2
\end{aligned}
$$
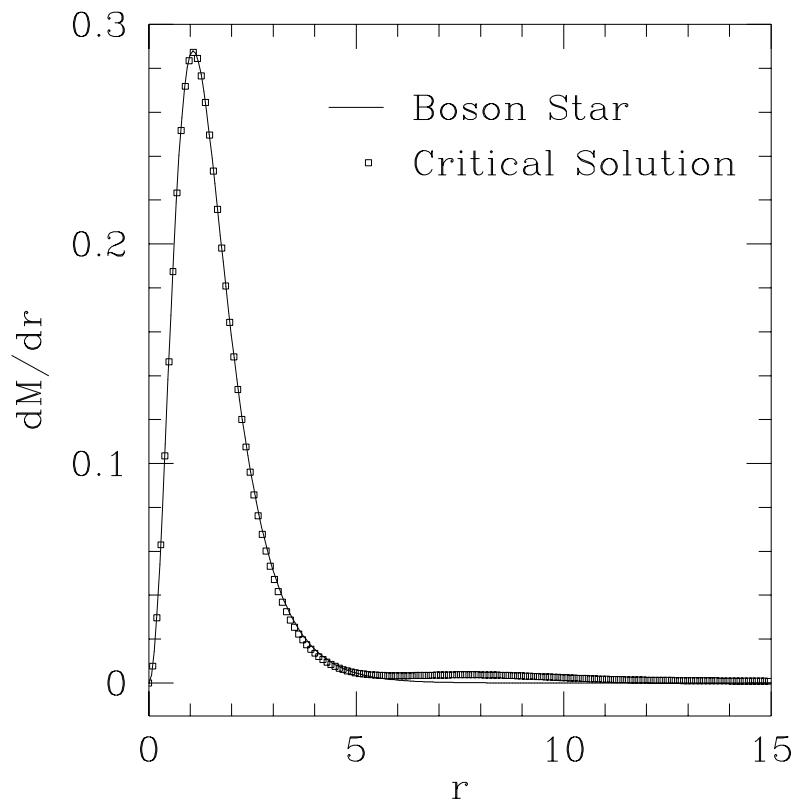
Figure 3.6: Comparison of highly unstable (low-mass) critical solution and boson star. Squares show a critical solution resulting from a boson star having $\phi_0(0) = 0.26 \times \sqrt{4\pi}$. (The data has been reduced for graphing purposes; the actual spatial resolution in the simulation is four times finer than that shown in the figure.) The solid line shows a "best fit" (unstable) boson star we constructed by finding the time average of $|\phi(t,0)|$ in the critical solution and using this as the value for $\phi_0(0)$ in the ODE integration routine which solves for the equilibrium (boson star) solutions. We see that there is a small halo near the outer edge of the solution ($r = 8$). The halo has the same relative magnitude when viewed in terms of the particle number distribution $\partial N/\partial r$. We discuss the halo phenomena further in Section 3.6.

46

and to rewrite the complex field $\phi(t, r)$ as

$$\phi(t, r) = [\psi_1(t, r) + i\psi_2(t, r)]e^{-i\omega t}, \tag{3.24}$$

where ψ_1 and ψ_2 are real. (Note that this is a different decomposition of the field ϕ than (3.7), the one used in the previous sections.)

In these variables, the equilibrium quantities are

$$\lambda(t, r) = \lambda_0(r) \tag{3.25}$$

$$\nu(t, r) = \nu_0(r) \tag{3.26}$$

$$\psi_1(t, r) = \phi_0(r) \tag{3.27}$$

$$\psi_2(t, r) = 0. \tag{3.28}$$

For the perturbation, we expand about the equilibrium quantities by first introducing four perturbation fields—$\delta\lambda(t, r)$, $\delta\nu(t, r)$, $\delta\psi_1(t, r)$ and $\delta\psi_2(t, r)$—and then setting:

$$\lambda(t, r) = \lambda_0(r) + \delta\lambda(t, r) \tag{3.29}$$

$$\nu(t, r) = \nu_0(r) + \delta\nu(t, r) \tag{3.30}$$

$$\psi_1(t, r) = \phi_0(r)(1 + \delta\psi_1(t, r)) \tag{3.31}$$

$$\psi_2(t, r) = \phi_0(r)\delta\psi_2(t, r). \tag{3.32}$$

These expressions are substituted into the relevant evolution and constraint equations (details in Appendix C), after which the resulting system can be reduced to the following system of two coupled second-order ordinary differential equations for $\delta\phi_1$ and $\delta\lambda$:

$$
\begin{aligned}
\delta\psi_1'' = \quad & - \left(\frac{2}{r} + \frac{\nu_0' - \lambda_0'}{2} \right) \delta\psi_1' - \frac{\delta\lambda'}{r\phi_0^2} + e^{\lambda_0 - \nu_0}\delta\ddot{\psi}_1 \\
& - \left[\frac{\phi_0'}{\phi_0} \left(\frac{\nu_0' - \lambda_0'}{2} + \frac{1}{r} \right) + \left(\frac{\phi_0'}{\phi_0} \right)^2 + \frac{1 - r\lambda_0'}{r^2\phi_0^2} + e^{\lambda_0 - \nu_0}\omega^2 - e^{\lambda_0} \right] \delta\lambda
\end{aligned}
$$

$$+ \quad 2e^{\lambda_0} \left[1 + e^{-\nu_0}\omega^2 + e^{-\lambda_0} \left(\frac{\phi_0'}{\phi_0} \right)^2 + r\phi_0\phi_0' \right] \delta\psi_1 \qquad (3.33)$$

$$\delta\lambda'' = \quad - \quad \frac{3}{2}(\nu_0' - \lambda_0')\delta\lambda' + \left[4\phi_0'^2 + \lambda_0'' + \frac{2}{r^2} - \frac{(\nu_0' - \lambda_0')^2}{2} - \frac{2\nu_0' + \lambda_0'}{r} \right] \delta\lambda + e^{\lambda_0 - \nu_0}\delta\ddot{\lambda}$$

$$- \quad 4(2\phi_0\phi_0' - re^{\lambda_0}\phi_0^2)\delta\psi_1'$$

$$- \quad 4 \left[2\phi_0'^2 - re^{\lambda_0}\phi_0^2 \left(2\frac{\phi_0'}{\phi_0} + \frac{2\nu_0' + \lambda_0'}{2} \right) \right] \delta\psi_1. \qquad (3.34)$$

To perform the stability analysis (normal-mode analysis), we assume a harmonic time dependence, $i.e.$,

$$\delta\psi_1(t, r) = \delta\psi_1(r) \, e^{i\sigma t}$$

$$\delta\lambda(t, r) = \delta\lambda(r) \, e^{i\sigma t}.$$

Note that (3.33) and (3.34) contain only second derivatives with respect to time, and because there are good reasons to assume σ^2 is purely real [61, 43], we only need to determine whether σ^2 is positive or negative to determine stability or instability, respectively.

Using the method described in Appendix C, we find the distribution for the squared frequency σ_0^2 of the fundamental mode, with respect to ϕ_0, which is shown in Figure 3.7.

Superposed with the fundamental mode, we may have other modes at higher frequencies. Figure 3.8 shows the relation between first harmonic frequencies and $\phi_0(0)$.

3.5 Comparison of Perturbation Analysis and Simulation Data

We wish to compare the results of our perturbation theory calculation with the oscillations of stable boson stars. Two differences exist between the conventions used in the perturbation theory calculation and those used in the boson star simulation
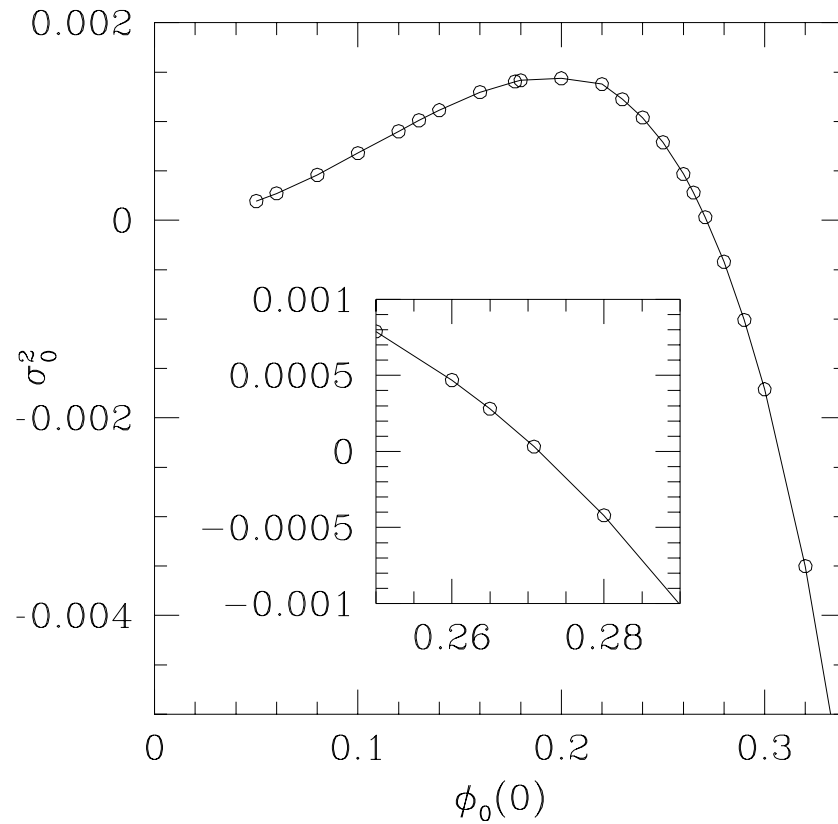
Figure 3.7: Mode frequencies of boson stars: fundamental mode. This plot shows a graph of σ_0^2, the squared frequency of the fundamental mode, versus the value of ϕ_0 at the origin. Note that, as the inset shows, σ_0^2 crosses zero when $\phi_0(0) \simeq 0.27$, which corresponds to a boson star with the maximum possible mass. (The circles show actual values obtained, and the solid line simply connects these points.)
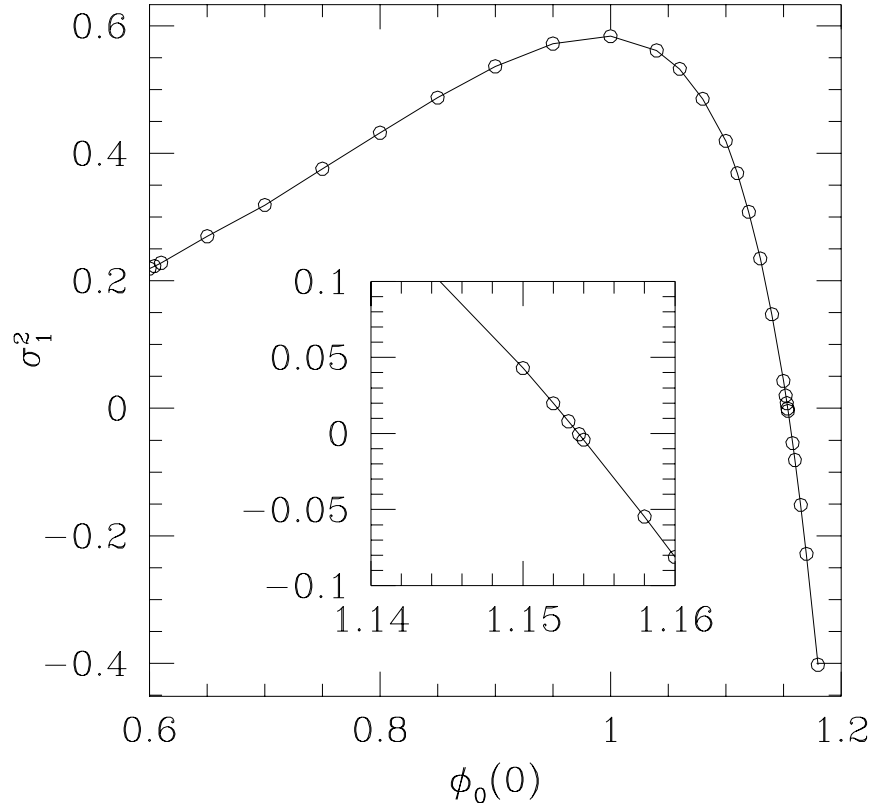
Figure 3.8: Mode frequencies of boson stars: first harmonic mode. This plot shows a graph of σ_1^2, the squared frequency of the first harmonic mode, versus the value of ϕ_0 at the origin. Note that, as the inset shows, σ_1^2 crosses zero when $\phi_0(0) \simeq 1.15$, which corresponds to the first local minimum on the unstable branch of the mass *vs.* radius curve (see Figure 3.5). (The circles show actual values obtained, and the solid line simply connects these points.)

data. The first difference is in the choice of the time coordinate. In the perturbation theory code, we choose a lapse of unity at the origin, whereas in the simulations we set the lapse to unity at spatial infinity. Thus we have the following mapping from the perturbation theory calculations to the simulations:

$$\sigma^2\Big|_{\text{Perturbative}} \rightarrow \frac{\sigma^2}{\alpha^2}\Big|_{\text{Simulation}}$$

The other significant difference is in the way the complex field $\phi(t,r)$ is decomposed into constituent real fields. Thus we cannot directly compare ϕ_1 and ψ_1, for example. We can, however, compare the modulus $|\phi|$ of the field. For the simulation data, the perturbation in $|\phi|$ can be taken directly from $(\phi_1^2 + \phi_2^2)^{1/2}$. For the data obtained from perturbation theory, the perturbation in $|\phi|$ will be, to first order, $\phi_0 \delta\psi_1$.

Before proceeding to the comparisons *per se*, we wish to point out that determining the unstable mode via numerical simulation of the full *nonlinear* system was very easy to do in comparison to the *linear* perturbation theory calculations.

3.5.1 Modes of Stable Boson Stars

We provide this subsection as a "warm-up" for the comparison of critical solutions and unstable boson stars. Consider the simulation data for which initially $\phi_0(0) = 0.05 \times \sqrt{4\pi}$. The boson star oscillates about a point of stable equilibrium. We take data from this equilibrium state and subtract it from the data at all times of the simulation, in order to extract the oscillatory mode. In the simulation, we find a period (in $\alpha(0)$) of about $T = (968.75 - 109.38, t)/4 = 214.8425$. The oscillation frequency is given by $\sigma = 2\pi/T$, from which we find $\sigma^2 = 8.553017 \times 10^{-4}$. The average value of $1/\alpha(t,0)^2$ during this interval is $\langle 1/\alpha^2 \rangle = 1.6281$. Thus the squared oscillation frequency to compare with the perturbation theory results is $\sigma^2/\alpha^2 = 0.00139$.

51

We choose simulation data at a local maximum in the oscillation cycle to compare with the perturbation theory results. At this time, the amplitude of the oscillation is $\Delta|\phi(t,0)| = 5.592091 \times 10^{-4}$. From the perturbation theory code, we find the proper solution is obtained using $\sigma^2 \simeq 0.00140$ and $\delta\lambda''(0) \simeq 2.5 \times 10^{-4}$. Thus the square of the oscillation frequency obtained from the simulation is in agreement with the value of $\simeq 0.0014$ obtained from the simulations.

We can graph the functions obtained and find good agreement between the simulation data and perturbation theory, as shown in Figures 3.9 and 3.10.

3.5.2 Unstable modes

To measure the unstable mode, we again perform a series of simulations in which we allow a gaussian pulse from an addition real, massless Klein-Gordon field to impinge on a stable boson star.

By tuning the amplitude of this pulse (holding constant the width of the pulse and its initial distance from the boson star), we can generate a family of slightly different near-critical solutions depending on the amplitude of the initial gaussian pulse, and can tune down the initial magnitude of the unstable mode. By subtracting these slightly different near-critical solutions, we obtain a direct measurement of the unstable mode.

Considering a specific example, we start with a stable boson star which has an initial field value at the origin of $\phi_0(0) = 0.04 \times \sqrt{4\pi}$. By driving it with a gaussian pulse tuned to machine precision, we can cause this stable star to become a critical solution which persists for very long times, oscillating about a local equilibrium. The average value of $|\phi(t,0)|$ is $\langle|\phi(t,0)|\rangle \simeq 0.463$. We measure the unstable mode by subtracting data of a run which contained a gaussian pulse with an amplitude that differed by 10^{-14} from that of the pulse tuned to machine precision. We can then measure the growth factor of the unstable mode by taking the L_2 norm of this

Figure 3.9: Fundamental mode of stable boson star. The dashed (red) line shows $\phi_0 \delta\psi_1$ from the perturbation theory calculations. To obtain the solid (green) line, we took the simulation data and subtracted the Klein-Gordon field at one instant of time from the data at another instant. We see that, to the eye, the two graphs are indistinguishable. When we begin the discussion of unstable modes, we will show the differences between perturbation theory and simulation results.

Figure 3.10: Fundamental mode of stable boson star. Perturbation in metric function a. The dashed (red) line shows the perturbation to the metric function a as found via perturbation theory calculations. To obtain the solid (green) line, we took the simulation data and subtracted the metric function a at one instant of time from the data at another instant.

difference at various times, taking the logarithm, and fitting a straight line to it. From this, we obtain $\sigma \simeq 0.109\,i$, or $\sigma^2 \simeq -0.0118$. Because of the differences in time coordinate between the simulations and perturbation theory calculations, we need to compute σ^2/α^2 in order to compare with the perturbation calculations. We find the average value of $1/\alpha(t,0)^2$ for the times listed above to be $\langle 1/\alpha(t,0)^2 \rangle \simeq 3.80$, and thus we find $\sigma^2/\alpha^2 \simeq -0.0450$. We choose to compare these perturbation theory results with data from a time in the simulation for which the difference in field values (for the two evolutions tuned slightly differently) is $\Delta|\phi(t,0)| \simeq 8.4 \times 10^{-13}$. We use this value in the perturbation theory solver and arrive at $\sigma^2 \simeq -0.045$, in good agreement with the value from the simulation. In Figures 3.11 and 3.12, we compare the graphs of the solutions for the unstable mode. In Figure 3.13 we show a comparison of the squared frequency values obtained from the linear perturbative analysis and those as measured in our simulations.

3.5.3 Oscillatory modes

We can also look at the oscillatory mode during the critical regime. We study the behavior of such a mode using the same technique we used to examine the fundamental mode of the unstable boson star: we subtract the data at one instant of time from the data at all other instants. Again, as a specific example, we use the same initial boson star as that used in the previous section. During the critical portion of the evolution, we notice an oscillation period of about $T \simeq 38.4$, and thus we obtain $\sigma = 2\pi/T \simeq 0.0261$. During this period, the average value of $1/\alpha^2(t,0)$ is about 3.80, and thus we find $\sigma^2/\alpha^2 \simeq 0.102$. We take data from a moment in the middle of the oscillation period, and subtract it from the data at other times. We can then compare the perturbation theory results with simulation data at a local peak of the oscillation. For the local peak we chose at time $t = t_p$, the difference in modulus of the field was $\Delta|\phi_{(t_p},0)| \simeq 0.0197$. Inserting this value into the
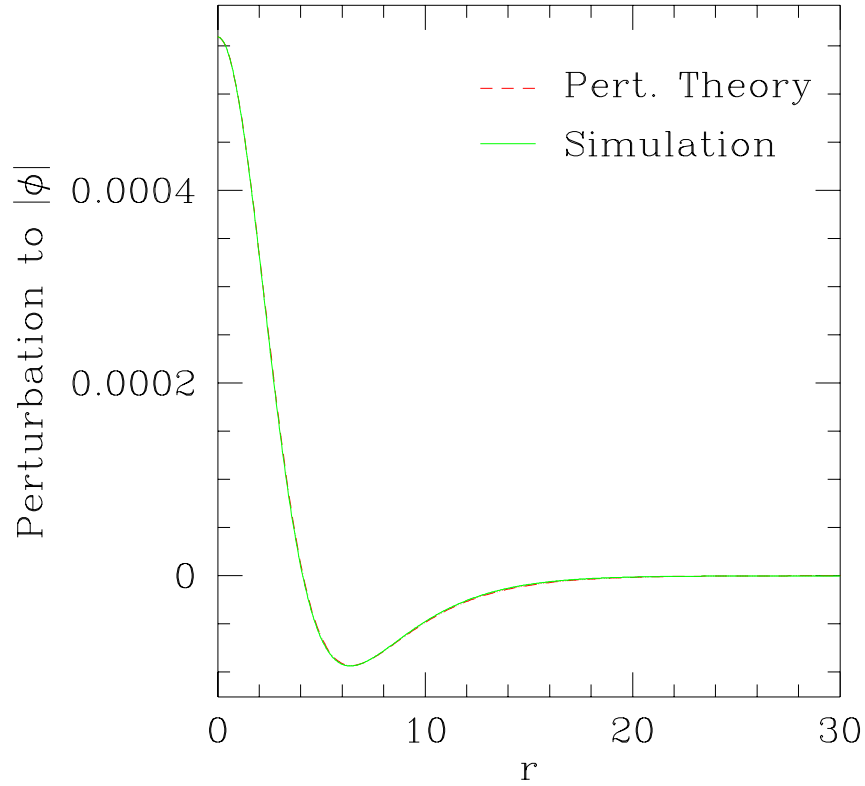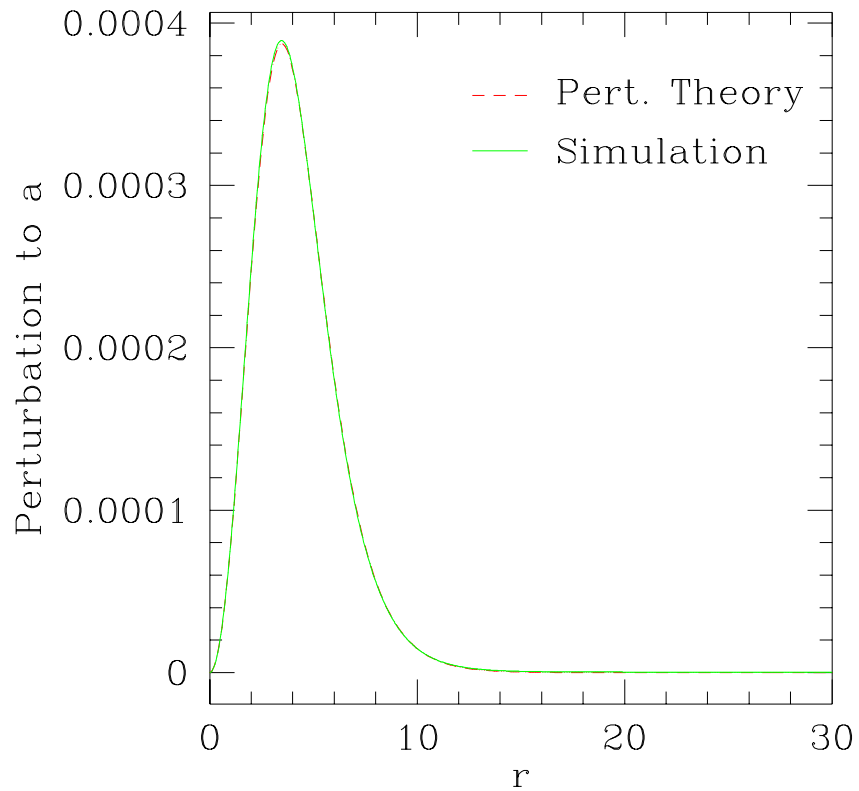
Figure 3.11: Fundamental mode of unstable boson star. (a) The solid line shows $\phi_0 \delta \psi_1$ from the perturbation theory calculations. The squares shows the difference between $|\phi|$ for two simulations for which the critical parameter p differs by 10^{-14}. (The data has been reduced for graphing purposes; the actual spatial resolution in the simulation is four times finer than what is shown in the figure.) Differences between the simulation data and perturbation theory results are below 1.1×10^{-15}. If a line were drawn connecting the squares, it would be indistinguishable, to the eye, from the perturbation theory line. Thus we provide a second graph (b) showing the difference of these results, where the scale is relative to the maximum value of $\delta|\phi|$.
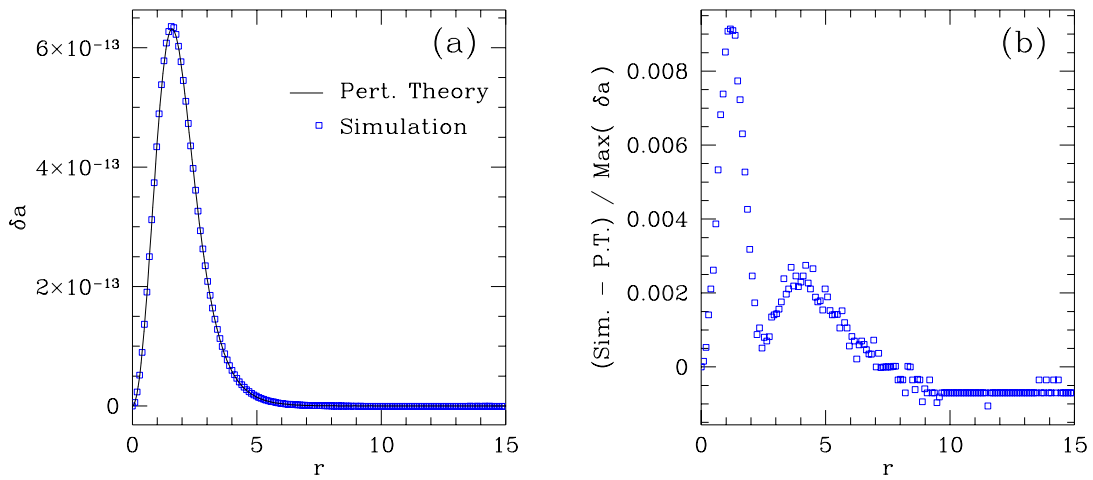
Figure 3.12: Fundamental mode of unstable boson star. (a) The solid line shows the perturbation to the metric function a, as found from the perturbation theory calculations. The squares shows the difference between the metric function a for two simulations for which the critical parameter p differs by 10^{-14}. (In the simulations, the spatial resolution was four times that shown in the figure.) (b) A plot of the difference between the mode obtained from the simulation and the mode obtained via perturbation theory, where the scale is relative to the maximum value of δa.
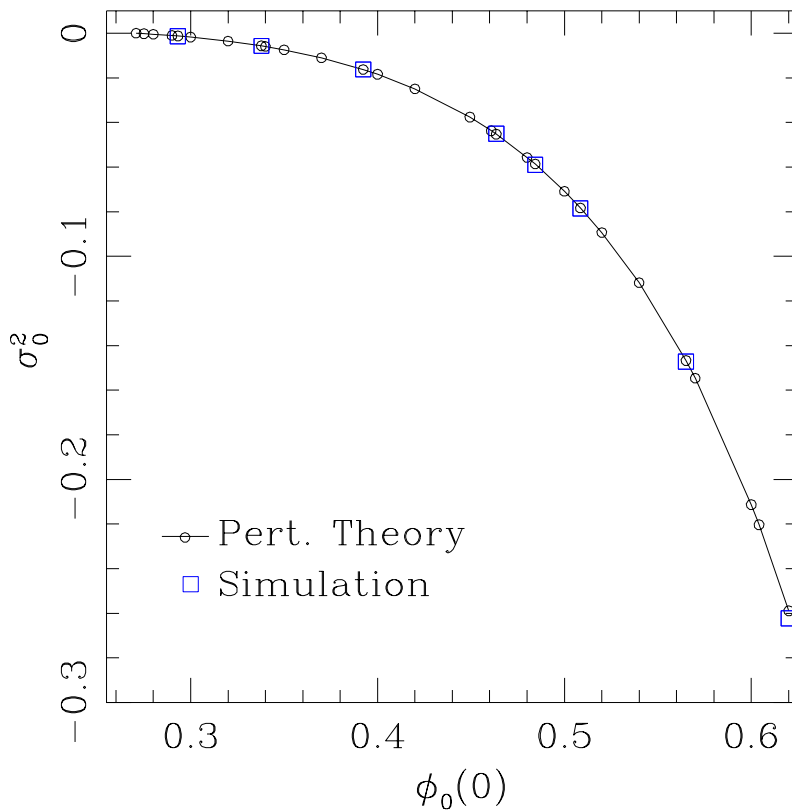
Figure 3.13: Comparison of squared frequencies/Lyapunov exponents for unstable modes. The circles show a subset of the perturbation theory data as displayed in Figure 3.7. The squares show the measurements obtained from our simulations. (The solid line simply connects the circles.) We note that the agreement between the two sets is good even for the more unstable, low-mass solutions. We also point out that the measurements of our simulations were performed along $r = 0$, *i.e.*, in the interior of the halo found in the low-mass solutions, which seems to strengthen the remarks at the end of Section 3.3, namely that, aside from the halo at the exterior of the critical solution, the critical solutions (of all masses) seem to correspond to unstable boson stars.

perturbation theory code, we find $\sigma^2 \simeq 0.102$ for this configuration. Thus we again find excellent agreement between the squared oscillation frequencies computed in perturbation theory and via simulation.

In Figures 3.14 and 3.15, we compare the functions obtained from the perturbation theory calculation with those from the simulation. We note that the agreement for the metric functions is very good for all radii, but the agreement in the fields begins to decline beyond $r = 5$. Why do the graphs of $|\phi|$ not agree well for the first harmonic? This could be a consequence of our simplistic method of extracting this mode. While our method of simply subtracting different frames has worked well for our test cases of oscillations of stable boson stars, the first harmonic of the unstable star has a higher frequency and thus our graph could be subject to sampling effects. A better method would be to perform a Fourier transform in time for each grid point, and construct the higher harmonics in the field accordingly. There may be a simple resolution to the discrepancy in the graphs of $|\phi|$, (3.7) and agreement in the graphs of the metric, our analysis does seem to indicate that the oscillations observed for this data in fact correspond to the first harmonic quasinormal mode of a boson star, however the analysis of the matter field needs further attention.

Finally, we must remark that we have been unable, using the fundamental and first harmonic modes of an unstable boson star, to construct a solution possessing a halo similar to that shown in Figure 3.6. We do *not* expect higher modes to be of any use here, because the halo is observed to oscillate with the same (single) frequency as the rest of the star. Since, as we described at the end of Section 3.3, the halo seems to be radiated away over time, we might not expect it to be described by the quasinormal modes (which conserve particle number) we have constructed.
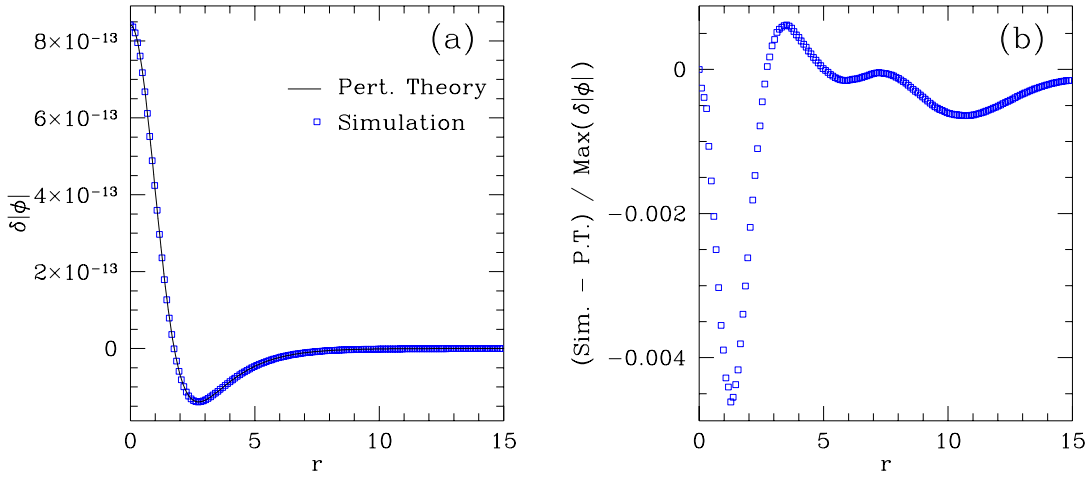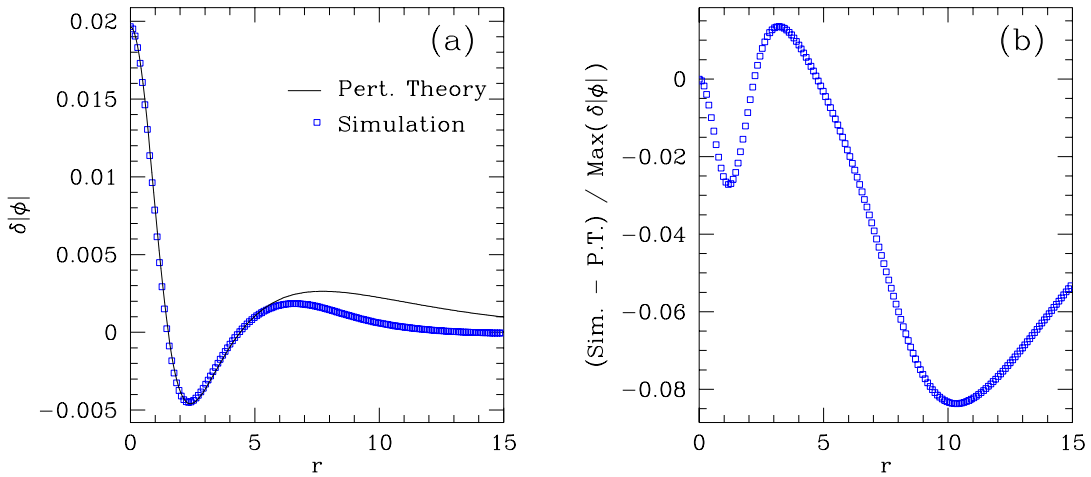
Figure 3.14: First harmonic of an unstable boson star. (a) The solid line shows $\phi_0 \delta\psi_1$ from the perturbation theory calculations. To obtain the squares, we took the simulation data and subtracted the Klein-Gordon field at one instant of time from the data at another instant. (The data in the simulations had a spatial resolution four times finer than what is shown in the figure.) (b) The squares show the difference between mode obtained from simulation and the mode obtained via perturbation theory, scaled relative to the maximum value of $\delta|\phi|$. As we describe in the text, the lack of agreement beyond $r \simeq 6$ may be an artifact of simplistic data analysis. The next figure shows that the metric quantities, which depend directly on the matter distribution (and thus on $|\phi|$), show a favorable comparison between the simulations and perturbation theory.
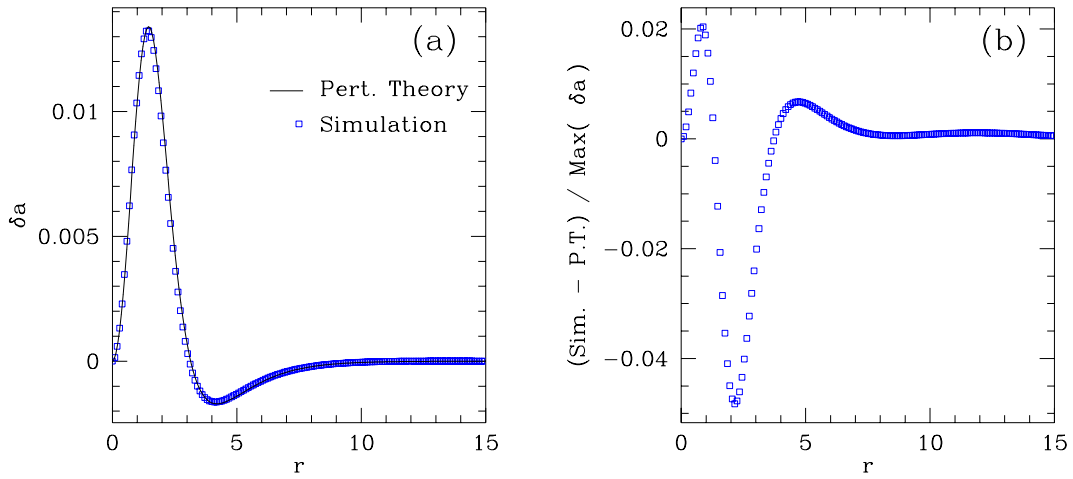
Figure 3.15: First harmonic of an unstable boson star. (a) The solid line shows the perturbation to a as found from perturbative calculations. To plot the squares, we took the simulation data and subtracted the metric function a at one instant of time from the data at another instant. (The spatial resolution in the simulation was four times finer than what is shown in the figure.) (b) The squares show the difference between the simulation data and the results of linear perturbation theory, scaled relative to the maximum value of δa. The close fit between these results indicates that the oscillations observed in the critical solutions correspond to stable oscillatory modes in an unstable boson star.

3.6 Halos

We have strong evidence that the critical solutions correspond to unstable boson stars, but the principal point of disagreement is existence of a "halo" of massive field which resides in the "tail" of the solution. It is our contention that this halo is not part of the true critical solution, but rather, is an artifact of the collision with the massless field.

In particular, the halo seems to be a remnant of the original (stable) boson star which is not induced to collapse with the rest of the star to form the true critical solution. We find that such a halo is observable in nearly all but the most massive (least unstable) critical solutions we have considered, and that its size tends to increase as less massive (more unstable) solutions are generated. The fact that the halo thus *decreases* as we approach the turning point only makes sense—a stable boson star very close to the turning point needs very little in the way of a perturbation from the massless field to be "popped" over to the unstable branch, and the final, unstable configuration, will, of course, be very close to the initial state.

Additionally, we note that in all cases we have examined, the field comprising the halo oscillates with nearly the same (single) frequency as the rest of the solution. This indicates that the halo is not explainable in terms of additional higher-frequency modes.

As one might expect, the properties of the halo are not universal, *i.e.* they are quite dependent on the type of initial data used. In contrast, the critical solution interior to the halo is largely independent of the form of the initial data. To demonstrate this, we use two families of initial data, given by a "gaussian" of Family I in Table 3.1 and a "kink" of Family II. A series of snapshots from one such pair of evolutions is shown in Figure 3.16. We find different amounts of mass transferred from the massless to the massive field for the kink and gaussian data, as shown in Figure 3.17, yet the central values of the field oscillate about nearly the same value

at nearly the same frequency. Both calculations start with identical boson stars with $|\phi(0,0)| = 0.04 \times \sqrt{4\pi}$. In the critical regimes, this becomes $\langle |\phi(t,0)| \rangle = 0.130 \times \sqrt{4\pi}$ for the solution obtained from the gaussian data, and $\langle |\phi(t,0)| \rangle = 0.135 \times \sqrt{4\pi}$ for the kink data. As already noted, the oscillation periods are also quite similar, differing by about 3%, and the masses interior to the halo are also quite comparable. In particular, it seems quite remarkable that the differences in mass interior to the halo for the two families are much smaller than the mass transferred from the real field in either case.

If we consider the inner edge of the halo to be where $\partial |\phi|/\partial r = 0$ at some finite radius (*e.g.*, $r \simeq 5$ in Figure 3.6), and look at the data between $r = 0$ and the inner edge of the halo, we find good agreement between this data and the profile of a boson star. This can be seen in both Figures 3.6 and 3.18.

We suspect that the halo is radiated over time (via scalar radiation, or "gravitational cooling" [91]) for all critical solutions. We find, however, that the time scale for radiation of the halo is comparable to the time scale for dispersal or black hole formation for each (nearly) critical solution we consider. Thus, while we see trends which indicate that the halo is indeed radiating, we are not able to demonstrate this conclusively for a variety of scenarios. With higher numerical precision, one might be able to more finely tune out the unstable mode, allowing more time to observe the behavior of the halo before dispersal or black hole formation occur.

3.7   Conclusions

We have shown that it is possible to induce gravitational collapse and, in particular, Type I critical phenomena in spherically-symmetric boson stars in the ground state, by means of "perturbations" resulting from gravitational interaction with an ingoing pulse from a massless real scalar field. Through this interaction, energy is transferred from the real to the complex field, and complex field is "driven" and
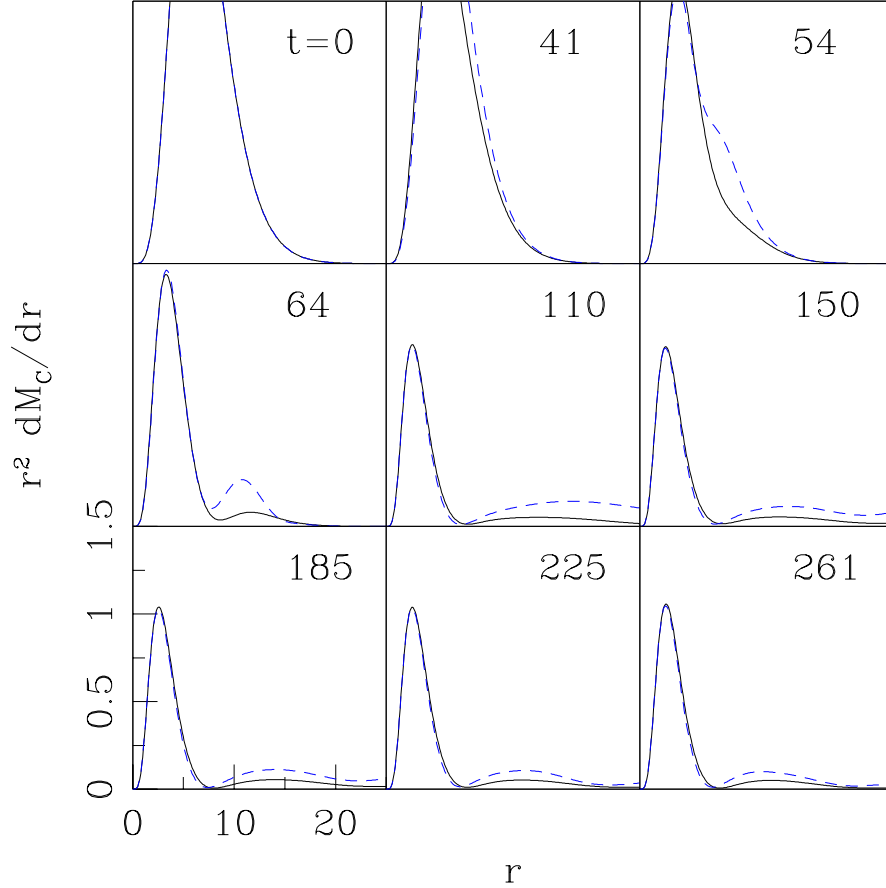
Figure 3.16: Evolution of $r^2 dM_C/dr$ for for two different sets of initial data. Both sets contain the same initial boson star, but the massless field ϕ_3 for one set is given by a "gaussian" of Family I (solid line) with $r_0 = 30$, and $\Delta = 8$ whereas for the other set ϕ_3 is given by a "kink" of Family II (dashed line) with $r_0 = 35$ and $\Delta = 3$. The variable A is varied (independently for each family) as the parameter p to obtain the critical solution. (Note that after $t \simeq 60$, the massless field has completely left the domain shown in the figure.) We have multiplied dM_C/dr by r^2 to highlight the dynamics of the halo; thus the main body of the solution appears to decrease in size as it moves to lower values of r. The kink data produces a larger and much more dynamical halo, but interior to the halo, the two critical solutions match closely — and also match the profile of an unstable boson star. Thus, the portion of the solution which is "universal" corresponds to an unstable boson star.
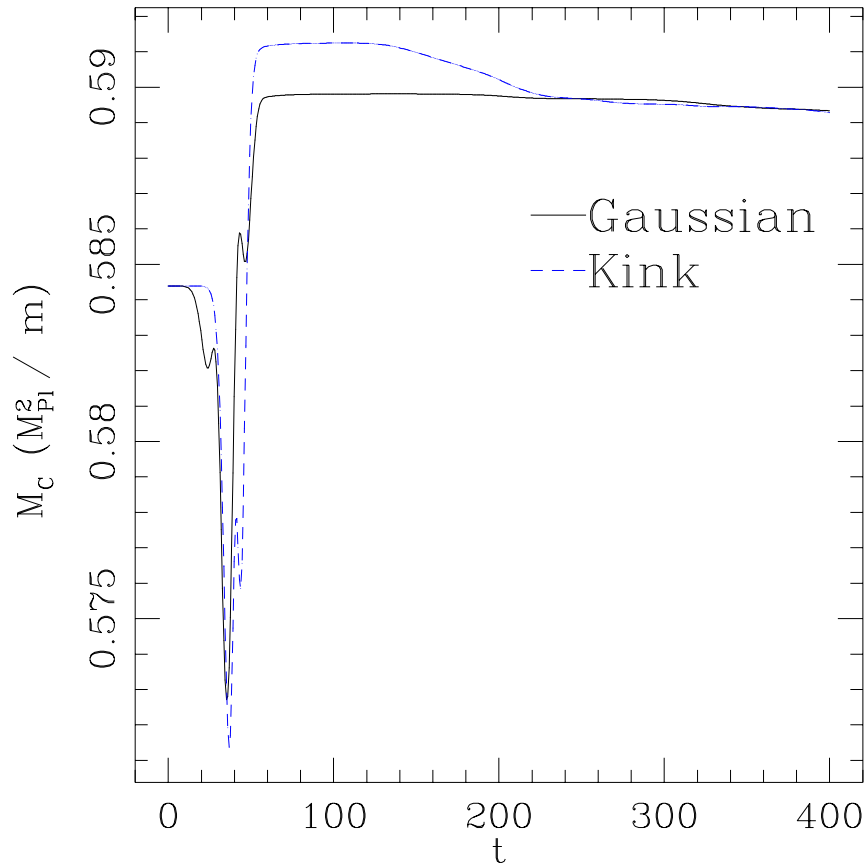
Figure 3.17: M_C *vs.* time for the two evolutions shown in Figure 3.16. Mass transfer from the real to the complex field occurs from $t \simeq 30$ to $t \simeq 60$, *i.e.* while the supports of the fields overlap. There is more mass transferred using the kink data, and yet the mass falls off rapidly. The mass of the kink data acquires a value very close to the mass of the gaussian data, which is itself decreasing slowly with time. We see that, beyond $t \simeq 250$, the difference in mass between the two solutions is very small compared with the amount of mass transferred from the real field.
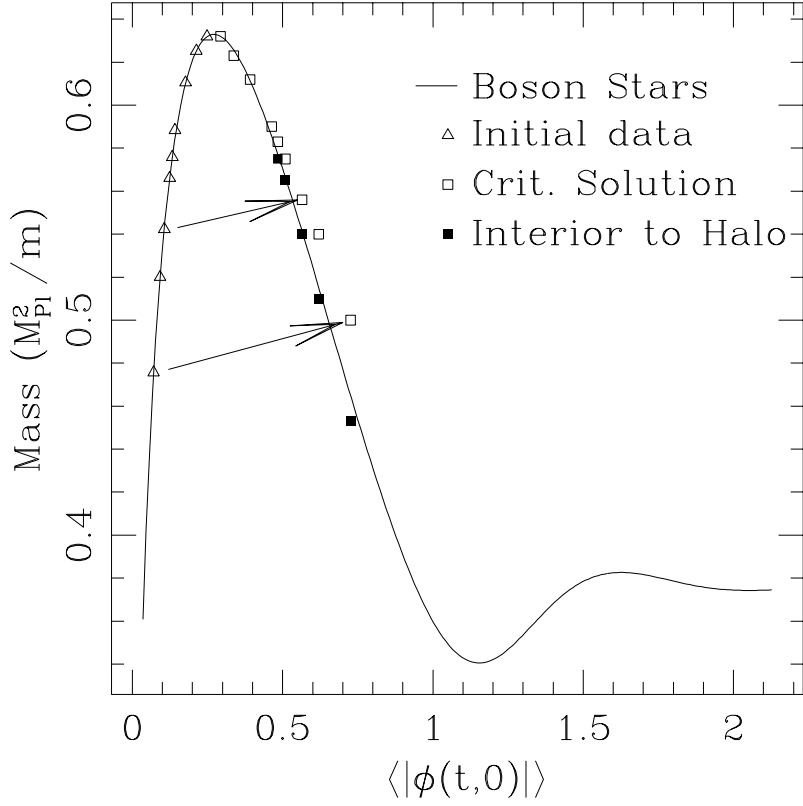
Figure 3.18: Mass *vs.* $\langle|\phi(t,0)|\rangle$, the time average of the central value of the field for equilibrium configurations of boson stars (solid line), initial data (triangles) and critical solutions (open and filled squares). Arrows are given to help match initial data with the corresponding critical solution. Points on the solid line to the left of the maximum mass $M_{\max} \simeq 0.633 M_{Pl}^2/m$ correspond to stable boson stars, whereas those to the right of the maximum correspond to unstable stars. The data is the same as that used for Figure 3.5, with data from one further evolution added at the bottom of the mass range. The open squares show the time average of the mass and $|\phi(t,0)|$ of some critical solutions, and the filled squares show the same quantities evaluated between $r = 0$ and the inner edge of the halo, defined to be the point where $\partial|\phi|/\partial r = 0$ for finite r. The mass of the critical solution is in general greater than the mass of the initial data, however the mass inside the halo of the critical solution is less than the mass of the initial data.

"squeezed" to form a critical solution. The massless field is not directly involved in the critical behavior observed in the complex massive field; the critical solution itself appears to correspond to a boson star, which, at any finite distance from criticality in parameter space, exhibits a superposition of stable and unstable modes.

Specifically, for initial data consisting of a boson star with nearly the maximum possible mass of $M_{\max} \simeq 0.633 M_{pl}^2/m$, the resulting critical solution oscillates about a state which has all the features of the corresponding unstable boson star in the ground state, having the same mass as the initial star. This result is reminiscent of the study by Brady *et al.* [15], who found that the Type I critical solutions for a real massive scalar field corresponded to the oscillating soliton stars of Seidel and Suen [89]. For boson stars with a mass somewhat less than $M_{\max}$, *e.g.*, $0.9 M_{\max}$ or less, however, we find less than complete agreement between the critical solution and an unstable boson star of comparable mass. This is evidenced by the presence of an additional spherical shell or "halo" of matter in the critical solution, located in what would be the tail of the corresponding boson star. Interior to this halo, we find that the critical solution compares favorably with the profile of an unstable boson star. Additionally, we have shown that the halo details depend on the specifics of the perturbing massless field, and we conjecture that, in the infinite time limit, the halo would be radiated away.

In order to extend the comparison between the critical solutions and boson stars, we have verified and applied the linear perturbation analysis presented by Gleiser and Watkins [43], extending their work by providing an algorithm to obtain modes with nonzero frequency. We have used this algorithm to give quantitative distributions of mode frequency *vs.* central density of the boson star for the first two modes, as well as to solve for the modes to compare with our simulation results. We have found that the unstable mode in the critical solutions have the same growth rate as the unstable mode of boson stars, and that the mode shapes also compare quite

favorably. We noted that the unstable mode of these boson stars was determined *much more easily* by solving the full nonlinear set of evolution equations, rather than via linear perturbation theory. The oscillations observed in the critical solution also indicated agreement with first harmonic mode obtained via perturbation theory, however the oscillatory mode in $|\phi|$ showed poor agreement at large radii, and awaits more careful analysis.

Future work may include simulations of the critical solutions of low mass using higher numerical precision to further tune away the initial amplitude of the unstable mode, thus allowing more time to observe the the small halo (*i.e.*, whether it is in fact being radiated away). We would also hope to obtain better agreement between simulation and perturbation theory for the first harmonic mode of the field $|\phi|$, perhaps using a more sophisticated method of extracting modes from the simulation. Another direction worthy of note would be to begin the simulation with a pulse of the complex field (instead of specifically a boson star) tune the height of the pulse to find the critical solutions via interpolation, and then compare the resulting critical solutions with our results obtained by perturbing boson stars.

Finally, we find it worthwhile to investigate similar scenarios for neutron stars. While there have been studies regarding the explosion of neutron stars near the minimum mass (*e.g.*, [33], [96]), we would like to see whether neutron stars of *non-minimal mass* can be driven to explode via dispersal from a critical solution. This may take the form of a neutron star approaching the onset of instability via slow accretion, or by being driven across the stability graph via violent heating from some other matter source, in a manner similar to the perturbations of boson stars we have considered in this chapter.

Chapter 4

Multi-Scalar Stars

A class of general relativistic solitons is considered in which multiple real scalar fields are expressed as Fourier cosine series with arbitrary temporal phase differences between the fields. For the special case of two scalar fields, a one-parameter family of solutions is found spanning from oscillating soliton stars (relative phase $\delta = 0$) to boson stars ($\delta = \pm\pi/2$). Numerical evolution of these solutions confirms their stability.

4.1 Introduction

In 1991, Seidel and Suen [90] showed the existence of non-topological solitons for a matter model without an explicit conserved Noether current: a minimally-coupled real-valued scalar field. Calling these "oscillating soliton stars", they constructed these solutions for the case of spherical symmetry by expanding the field and metric variables as Fourier cosine series, with expansion coefficients depending only on radial position. They then demonstrated, via direct numerical evolution, that the solutions obtained are stable and indeed persist with the required periodicity. In this chapter, we present an extension of Seidel and Suen's work on oscillating soliton

stars, in which multiple scalar fields are considered.

The matter model we are interested in is that of n Klein-Gordon fields without self-interaction, minimally coupled to general relativity. Such a model has a Lagrangian density given by

$$\mathcal{L} = R\sqrt{-g} - \frac{\sqrt{-g}}{2} \sum_{i=1}^{n} \left(\phi_i{}^{;a}\phi_{i;a} - m_i^2 \phi_i^2 \right) \tag{4.1}$$

We work in spherical symmetry, using the "polar/areal" coordinate system

$$ds^2 = -\alpha^2(t,r)dt^2 + a^2(t,r)dr^2 + r^2 d\Omega^2 \tag{4.2}$$

The complete evolution of the field and metric is given in terms of the Klein-Gordon equation and two constraints from Einstein's equations. The equations can be written as:

$$\begin{aligned}
\ddot{\phi}_i &= \frac{(\alpha^2)^{\cdot}}{2\alpha^2}\dot{\phi}_i + \frac{(\alpha^2)'}{2a^2}\phi_i' + \frac{2}{r}\frac{\alpha^2}{a^2}\phi_i' \\
&+ \frac{\alpha^2}{a^2}\left[\phi_i'' + \frac{(a^2)'}{2a^2}\phi_i' + \frac{(a^2)^{\cdot}}{2\alpha^2}\dot{\phi}_i \right] - m_i^2 \alpha^2 \phi_i,
\end{aligned} \tag{4.3}$$

$$\begin{aligned}
(\alpha^2)' &= (\alpha^2)\left(\frac{a^2-1}{r} \right) + \\
&\quad 4\pi G r \sum_{i=1}^{n} (a^2 \dot{\phi}_i{}^2 + \alpha^2 \phi_i'^2 - m_i^2 \alpha^2 a^2 \phi_i^2),
\end{aligned} \tag{4.4}$$

$$\begin{aligned}
(a^2)' &= - a^2\left(\frac{a^2-1}{r} \right) \\
&\quad + 4\pi G r a^2 \sum_{i=1}^{n} \left(\frac{a^2}{\alpha^2}\dot{\phi}_i{}^2 + \phi_i'^2 + a^2 m_i^2 \phi_i^2 \right),
\end{aligned} \tag{4.5}$$

where an overdot is used to denote $\partial/\partial t$ and a prime to denote $\partial/\partial r$.

70

We start by considering only one scalar field, *i.e.* $n = 1$. We note that the "slicing condition" (4.4) and the "Hamiltonian constraint" (4.5) are unchanged if we decompose ϕ into two identical fields ($n = 2$), ϕ_1 and $\phi_2 = \phi_1$, such that

$$\phi = \frac{1}{\sqrt{2}} \left(\phi_1 + \phi_2\right). \tag{4.6}$$

Also, the Klein-Gordon equation (4.3) is unchanged if we multiply ϕ by a constant. (Thus we can absorb the factors of $4\pi G$ in (4.4) and (4.5) by letting $\sqrt{4\pi G}\phi \rightarrow \phi$.)

Since a soliton solution corresponding to (4.3)-(4.5) is the oscillating soliton star, we see that a trivial multi-scalar soliton solution can be obtained by constructing an oscillating soliton star with a single field, as described in Seidel and Suen's paper [90] and then performing the decomposition (4.6).

On the other hand, if we wish to model a boson star, then we have one massive complex scalar field $\tilde{\phi}$, for which the real and imaginary parts behave like two real-valued scalar fields: $\tilde{\phi} = \phi_1 + i\phi_2$. The boson star ansatz is $\tilde{\phi} = \hat{\phi}(r)\exp(\pm i\omega t)$, where $\hat{\phi}(r)$ is real. This implies

$$
\begin{aligned}
\phi_1 &= \hat{\phi}(r)\cos(\omega t) \\
\phi_2 &= \hat{\phi}(r)\cos(\omega t + \delta),
\end{aligned}
\tag{4.7}
$$

where $\delta = \mp\pi/2$.

Comparing the soliton star and the boson star, we find that both solutions can be obtained by using two real-valued scalar fields. For the soliton star, the fields will have equivalent radial and temporal dependence; whereas for the boson star, the fields have equivalent radial dependence, and the temporal dependence is the same to within a phase.

4.2   Phase-Shifted Boson Stars

The work described in this chapter began in the midst of our numerical evolutions of boson stars. The question arose, "What happens if we solve for the boson star

initial data, then 'manually' change the phase relationship of the two fields, keeping their radial dependence unchanged, and then, finally, re-solve for the metric variables using the new matter configuration?" For future reference, we term such a configuration a "phase-shifted boson star." This was in part motivated by a desire to study oscillating soliton stars, and by our initial difficulty in constructing the proper initial data. Taking the boson star initial data and manually removing the phase shift between the two fields resulted in what might be termed a "poor man's soliton star." Such a system demonstrates a stable, quasi-periodic behavior as shown in Figure 4.1.

We then considered solutions in which we again took the boson star initial data $\hat{\phi}(r)$ and distributed it to ϕ_1 and ϕ_2 using some different value of δ, such as $\delta = \pi/6$. The evolution for such a system can be seen in Figure 4.2.

For each of the many values of δ we tried, we found an apparently stable solution which oscillated in some nearly periodic manner for very long times. These results led Choptuik to conjecture [28] that there may exist a *continuous family* of periodic soliton-like solutions, parameterized by the phase δ.

While our "phase-shifted boson stars" already constitute such a family, we wished to construct periodic multi-scalar solutions *directly* via a periodic *ansatz* of the form used by Seidel and Suen for their oscillating soliton stars.

4.3   Constructing Periodic Solutions

The method used for constructing the solutions is a natural extension of that used in [90]. We expand the fields and metric variables in the following manner:

$$\phi_i(t, r) = \sum_{j=1}^{\infty} \phi_{i,2j-1}(r) \cos[(2j-1)\omega t + \delta_i] , \qquad (4.8)$$
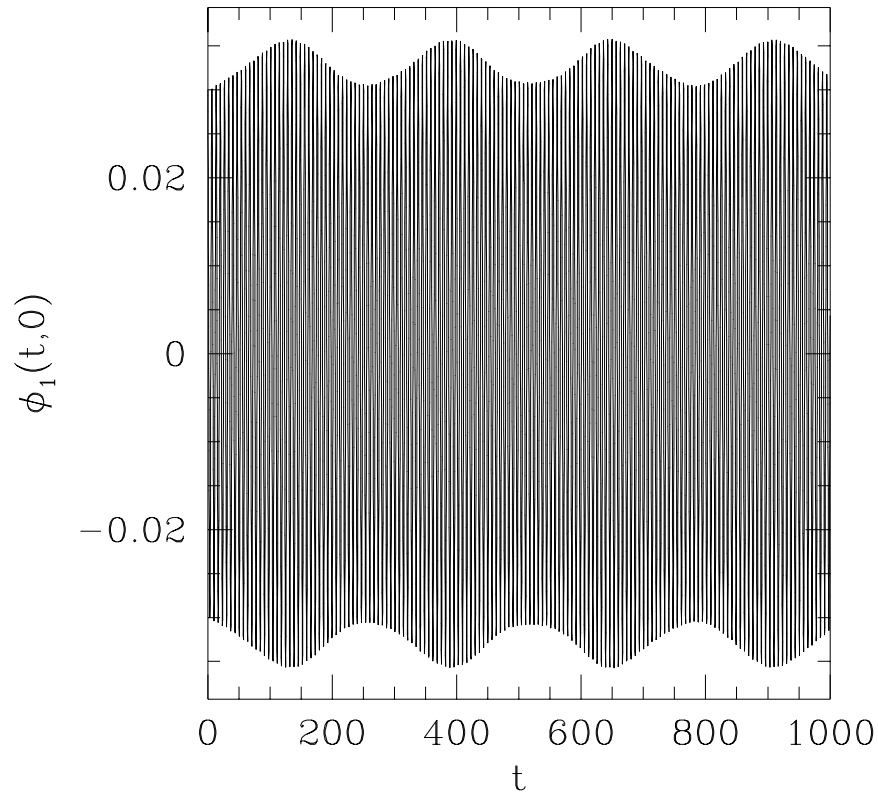
Figure 4.1: Central value of the fields $\phi_1(t,0) = \phi_2(t,0)$ vs. time t, for the "poor man's soliton star" obtained via solving for boson star initial data and altering ϕ_2 by setting $\phi_2(0,r) = \phi_1(0,r)$. One can see (*e.g.* near $t = 800$) that the solution is not completely periodic, but it is nevertheless long-lived. Stable evolutions of this system have been obtained for $t > 20000$.
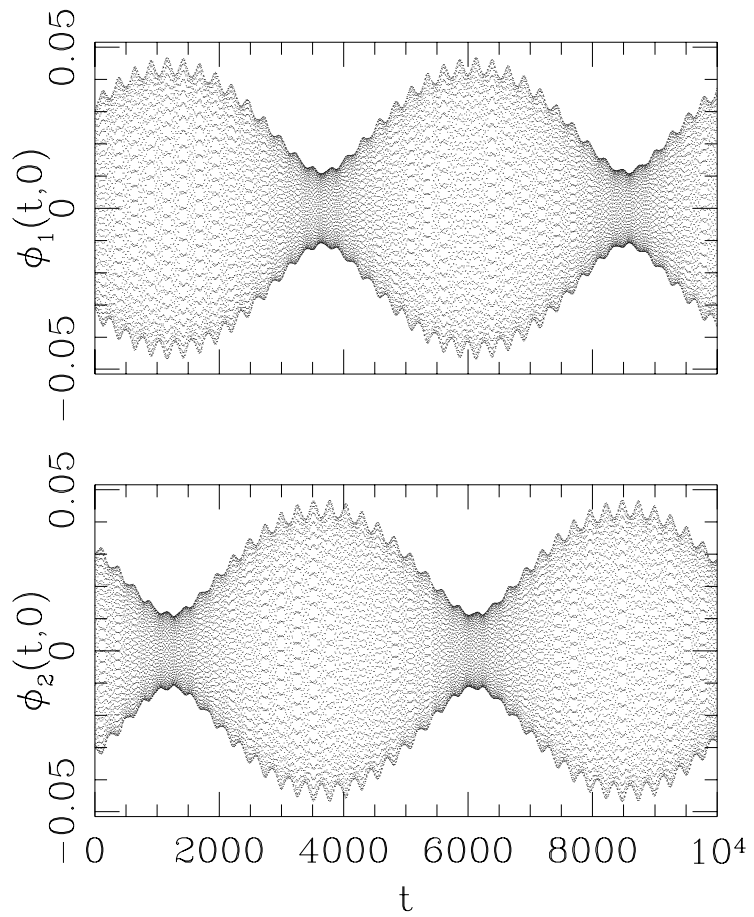
Figure 4.2: Central value of the fields $\phi_1(t, 0) = \phi_2(t, 0)$ vs. time t, for the phase-shifted boson star with $\delta = \pi/6$. Note the trade-off of energy between the two fields.

$$\alpha^2(t,r) = 1 \;+\; \alpha_{1,0}(r)$$
$$+\; \sum_{i=2}^{n}\sum_{j=1}^{\infty}\alpha_{i,2j}(r)\cos[2j\omega t + 2\delta_i]\,, \qquad (4.9)$$

$$a^2(t,r) = 1 \;+\; a_{1,0}(r)$$
$$+\; \sum_{i=2}^{n}\sum_{j=1}^{\infty}a_{i,2j}(r)\cos[2j\omega t + 2\delta_i]\,. \qquad (4.10)$$

We insert the above expressions into Eqs. (4.3)-(4.5), expanding the resulting equations in terms of sines and cosines, and obtain a set of ordinary differential equations (ODEs) by requiring that the coefficients of a given Fourier mode sum to zero. Regularity at $r = 0$ requires $(\partial/\partial r)\phi_{i,j}(0) = 0$ as well as local flatness, $a_{i,j}(0) = 0$. Asymptotic flatness requires $a_{i,j}(r)$ and $\phi_{i,j}(r)$ go to zero sufficiently rapidly as $r \to \infty$. Since the $\alpha_{i,j}(r)$ are part of the lapse, and thus represents freedom in choosing a coordinate system, we require only that they asymptotically approach constant values as $r \to \infty$. The equations (4.3)-(4.5) along with the above boundary conditions constitute an eigenvalue or "shooting" problem. The eigenvalues we shoot for are $\alpha_{i,j}(0)$, given $\phi_{i,j}(0)$. (We choose $\omega = 1$ because ω can be absorbed into the choice of the time coordinate, $t \to t/\omega$, $\alpha \to \alpha\omega$.) This would ordinarily constitute a *multidimensional* parameter space search for the eigenvalues $\alpha_{i,j}(0)$, however coordinate freedom allows us to reduce the parameter space to *one* dimension by choosing $\alpha_{i\geq 2,j}(0) = 0$. This choice has the additional benefit of allowing for a simple boundary condition on the derivatives $\phi''_{i,j}$ at $r = 0$, which we need in order to do the integration: Our choice $\alpha_{i\geq 2,j}(0) = 0$ means that the $\phi''_{i,j}(0)$ completely decouple from one another in Eq. (4.3) in the limit $r \to 0$, and we obtain the equation

$$\phi''_{i,j}(0) = \left(\frac{1}{3}\,\phi_{i,j}\,\frac{\alpha_{1,0}}{1 + \alpha_{1,0}}\right)\Bigg|_{r=0}.$$

In practice we must truncate the sums in (4.8)-(4.10) at some finite maximum value of j, denoted by $j_{\max}$. The resulting system of equations is in general underdetermined, but we solve only the $3nj_{\max} + 4$ equations corresponding to the lowest modes, treating the other modes as higher order corrections which we neglect.

We now return to the previous example of boson stars and oscillating soliton stars, both of which we can obtain by setting $n = 2$ in the expansions (4.8)-(4.10), and setting $m_i = m$ and all $\phi_{i,j}(r)$ for a given j equal to each other, as in $\phi_{i,j}(r) = \hat{\phi}_j(r)$. This has the effect of making all $\alpha_{i,j}(r)$ equal to the same $\hat{\alpha}_j(r)$ for a given j, and similarly $a_{i,j}(r) = \hat{a}_j(r)$. We also set $\delta_1 = 0$ and define $\delta \equiv \delta_2$. Both the soliton star of [90] and the boson star require $\hat{\phi}_{j \geq 3}(0) = 0$. This means that the only free parameters are $\hat{\phi}_1(0)$ and δ, leaving $\alpha_{1,0}$ as an eigenvalue for which to shoot. Thus by construction, for a given $\hat{\phi}_1(0)$, one will obtain a soliton star if one sets $\delta = 0$, and a boson star for $\delta = \pm \pi/2$.

One wonders how well the truncated series expansion matches the ideal solution one would obtain given an infinite number of modes. Clearly one would hope that the series would converge rapidly enough to justify taking only a few terms. Figure 4.3 demonstrates the convergence of the series (4.10) for different values of δ, given $j_{\max} = 2$.

The relation between between total mass and radius of the star is shown in Figure 4.4, for various values of δ. The inset shows the relation between the maximum mass of the star and the phase angle δ.

We see that there exist great similarities between boson stars and oscillating soliton stars, and that both are members of a larger family of two-scalar solutions. A question arises, however, regarding the stability of the general two-scalar stars: Do these configurations persist and maintain their periodicity in the face of perturbations? To answer this question, we opt for a numerical solution of Eqs.(4.3)-(4.5).
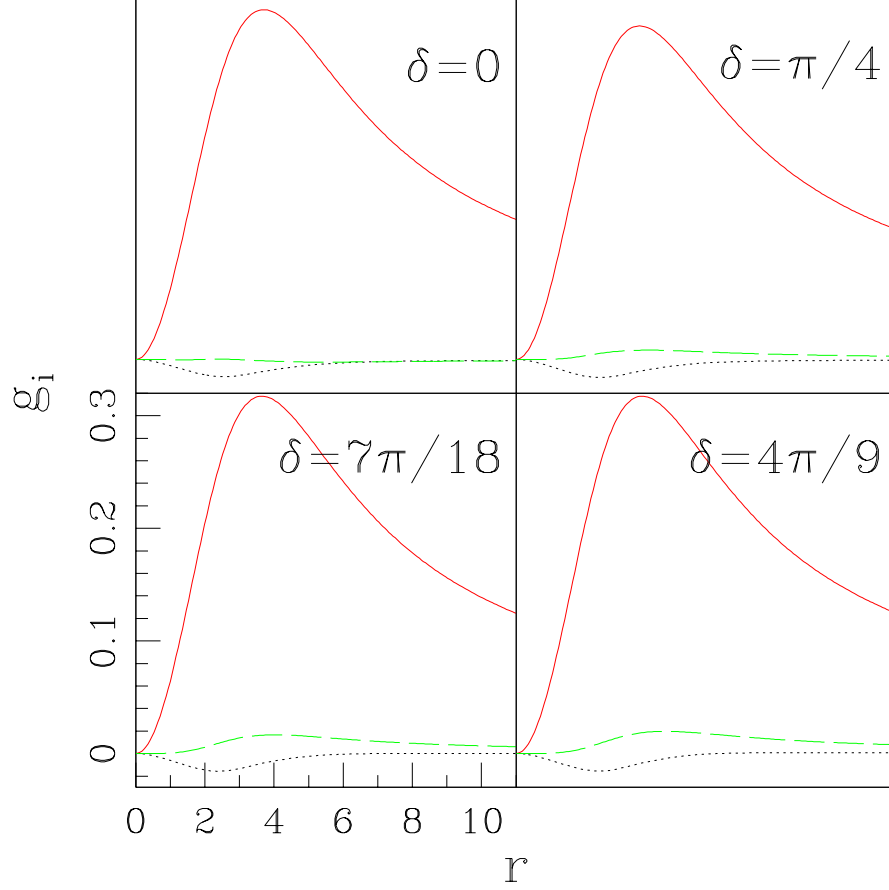
Figure 4.3: Convergence of the multi-scalar star series for the metric coefficient functions g_i, for four values of the phase shift δ. The solid (red) line shows g_0, the short dashed (blue) line shows g_2, and the long-dashed (green) line shows g_4. Thus the expansion seems to converge rapidly. For a boson star ($\delta = \pi/2$), there is only one oscillatory mode. For this case, we find $\phi_3(r) \to 0$ as $\delta \to \pi/2$, but we do not find the higher-order coefficient functions, e.g. $g_2(r)$, $g_4(r)$, vanishing as $\delta \to \pi/2$. The total contributions to the metric functions a^2 and α^2 given by (4.10) and (4.9) contain the coefficient functions multiplied by quantities which go as $\cos(\omega t) + \cos(\omega t + 2\delta)$, which *do* go to zero as $\delta \to \pi/2$.
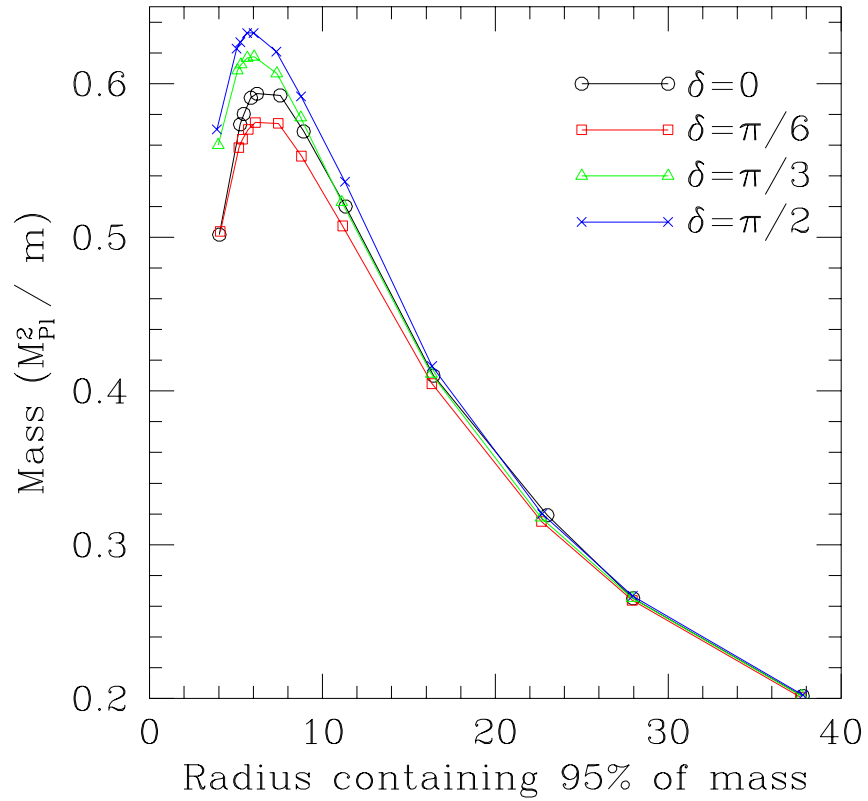
Figure 4.4: Comparison of mass *vs.* radius for a family of two-scalar stars parameterized by the temporal phase shift δ. We see that boson stars ($\delta = \pi/2$) are similar to oscillating soliton stars ($\delta = 0$) in terms of mass and radius.

4.4   Numerical Evolution of the Solutions

We use the same numerical code as used for the boson star study of Chapter 3. Having obtained the initial data by integrating the ODEs described above, we define new variables

$$\Phi_i \equiv \phi_i', \qquad \Pi_i \equiv \frac{a}{\alpha}\dot{\phi}_i \qquad (4.11)$$

In terms of these new variables, the relevant evolution equations are

$$\dot{\Phi}_i = \left(\frac{\alpha}{a}\Pi_i\right)' \qquad (4.12)$$

$$\dot{\Pi}_i = \frac{1}{r^2}\left(\frac{r^2\alpha}{a}\Pi_i\right)' - m_i^2\alpha a\phi_i \qquad (4.13)$$

and we solve for the fields ϕ_i and the metric variables by integrating along each spatial hypersurface the equations $\phi_i' = \Phi_i$ and

$$a' = a\frac{1-a^2}{2r} + \frac{1}{2}ra\sum_{i=1}^{n}\left(\Pi_i{}^2 + \Phi_i{}^2 + a^2 m_i^2\phi_i^2\right) \qquad (4.14)$$

$$\alpha' = \alpha\left(\frac{a^2-1}{r} + \frac{a'}{a} - ra^2\sum_{i=1}^{n}m_i^2\phi_i^2\right) . \qquad (4.15)$$

The boundary conditions at $r = 0$ are the same as those stated previously with the exception that we choose the lapse α such that the coordinate t measures proper time as $r \to \infty$. As in Chapter 3, we use as an outer boundary condition the Sommerfeld condition for a massless field. We ran our simulations with different values of computational domain size $r_{\max}$, trying to test for any periodicity or other effects that might be a function of the outer boundary, but we found the results to be essentially independent of $r_{\max}$, even for times which are large compared to the time for information to cross the grid (e.g. $0 \le t \le 2000$ with $r_{\max} \sim 50$). We attribute this to the fact that there is very little scalar radiation from these compact objects.

4.5 Simulation of Multi-Scalar Stars

When we evolve the initial data, we find that the resulting solutions deviate sharply from the periodic *ansatz*. This is shown in Figure 4.5. We are still investigating the cause of this disagreement. We note, however, that the numerical solutions do follow quasi-periodic evolutions over long time scales, further promoting the idea that quasi-periodic two-scalar solutions may be common.

4.6 Conclusion

We have demonstrated the existence of at least one family of multi-scalar solutions we call "phase-shifted boson stars" which are obtained by solving the ODEs associated with boson stars and then altering the phase between the real and imaginary parts of the field. These solutions may not be strictly periodic or strictly stable, but they are very long-lived and demonstrate periodicity over these long time scales. Direct construction of strictly periodic solutions via a Fourier cosine series similar to that of Seidel and Suen [90] yields series which converge rapidly, and for a special subclass produce a one-parameter family in the phase shift δ, spanning oscillating soliton stars at $\delta = 0$ to boson stars at $\delta = \pi/2$. For other values of δ, we do not find agreement between numerical evolution of the initial data and the periodic *ansatz*, rather we find a *different* quasi-periodic, long-lived solution. The cause of this alternate evolution is still under investigation.
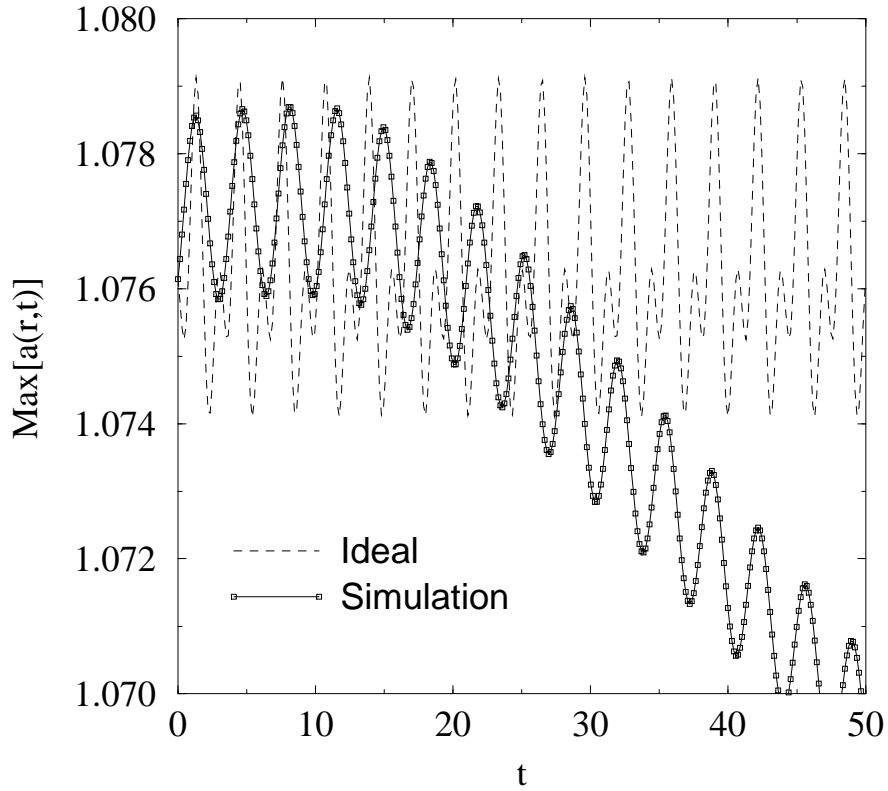
Figure 4.5: Results from evolution of a two-scalar star for initial data with $\phi_i(0,0) = 0.04$, $\delta = \pi/4$, showing the maximum value of a on each spacelike hypersurface parameterized by t. Dashed lines show the "ideal" solution obtained by evaluating (4.3)-(4.5) as a function of t. The solid lines show the results of simulation on the domain $0 \leq r_{\mathtt{max}} \leq 75$. We see that the simulation data differs markedly from the periodic *ansatz* solution.

Chapter 5

Toward Automatic Adaptive Mesh Refinement (AMR)

5.1   AMR In General

One of the most common techniques for obtaining approximate solutions to time-dependent partial differential equations (PDEs) is the use of finite difference techniques, in which the spatial domain is discretized into a grid or *mesh*, and the partial derivatives are replaced with algebraic relationships between neighboring (closely-spaced) grid points. The relative closeness of the grid points is called the *resolution*, and it is in general the case that high resolution provides for high accuracy — that is, good approximation to the underlying PDEs — but at the cost of a long time for the computation to be performed.

Adaptive Mesh Refinement (AMR) is a class of techniques which involve varying the resolution throughout the simulation domain, and which, in principle, provide a given degree of *accuracy* in a shorter amount of *time* than that required for the application of finite differencing on a single, uniformly spaced mesh — what we will call "unigrid" algorithms. In the discussion to follow, we will mainly refer to

methods which have been developed for systems of *hyperbolic* differential equations. There is a host of literature and methods devoted to the solution of elliptic and parabolic equations via adaptive mesh techniques, however we will not delve into such matters here.

5.2 The Desire for 'Adaptivity'

For any sophisticated simulation in which a high level of accuracy is required, some sort of adaptivity in the way the various physical quantities are represented on the domain is desirable for two main reasons.

1. Computational Necessities. Any computer system will have finite resources, and furthermore may charge the user a fee in proportion to the use of these resources. If the user wants to run a unigrid simulation to generate a highly accurate representation of a physical system, he might desire a very large grid which would require storage allocation in excess of what is available on many computer systems, and even if the program fit in memory, it may take months to run the simulation. A user's goal would probably be to run a program which produces the desired amount of accuracy, executes in a minimum amount of time, and consumes a minimum of the storage resources on the system. AMR minimizes storage requirements by only placing finely-spaced grid points where they are needed, and when they are needed, and also minimizes computation time by minimizing the number of grid points (and hence the number of pointwise operations).

2. Unanticipated Resolution Requirements. It is often the case that the resolution requirements of a simulation (for a fixed local accuracy) may not be known *a priori*. A unigrid code in which data evolve toward the formation of unanticipated small-scale features may leave the user no recourse but to terminate the execution and re-run the simulation with a higher resolution, thereby wasting time and other computing resources. Thus it would be desirable to have an algorithm

83

which dynamically responds to the need to maintain accuracy in the simulation.

For several years, AMR has been an attractive idea for researchers in numerical relativity [70], yet the implementation of AMR schemes has proceeded rather slowly from the pioneering work of Choptuik [23, 24]. During the Binary Black Hole Grand Challenge project, it was noted by Choptuik [21] that simulation codes in numerical relativity have tended to be fairly homogeneous from a "high-level" perspective, in that nearly all the codes being developed at the time used low-order (second-order) finite difference techniques on a single mesh, and had a basic structure of the form [21]

```
Read initial state
for NUM_STEPS
        for NUM_UPDATES or until convergence
                Update(Grid Function(s)) → Grid Function(s)
        end for
end for
Write final state
```

Choptuik pointed out that most of labor in developing these sorts of simulation codes goes into the construction of stable, accurate updates. He promoted the idea of using the AMR algorithm of Berger and Oliger (described below) as a way to allow relativists to concentrate on the development of stable unigrid codes for a serial architecture. The Berger and Oliger method would then allow for parallelism and adaptivity to be provided automatically by the main program driver.

Berger and Oliger AMR, in General

The 1984 paper of Berger and Oliger [11] describes an AMR algorithm in which the spatial domain is decomposed into a collection of uniform, rectangular grids of various degrees of resolution, placed throughout the computational domain at arbitrary orientations relative to one another. These grids can (and do) overlap, *i.e.* parts of different grids may contain the same subset of the domain. Each uniform

grid is evolved separately, with boundary information supplied by other grids or physical boundary conditions. Because the uniform grids are evolved separately, the Berger and Oliger algorithm allows users to concentrate on writing update routines for unigrid applications.

In this scheme, we start with a single uniform grid we call the *base* grid, which covers the entire domain and does not change throughout the simulation. We place other grids "on top of" the base grid (*i.e.* we define new grids which cover a subset of the space covered by the base grid) which have finer resolution, in order to resolve features in the simulation. We can place other, finer grids on top of these grids as determined by the accuracy requirements of the code. The criterion that determines when and where new grids are needed is an approximation of the local solution error, obtained via Richardson expansion. Recall from Chapter 2 that, *for sufficiently smooth functions* and for centered difference schemes, we can expect the error to be given as an even power series in the mesh spacing h, where the coefficient functions in this series are independent of h and thus we can obtain local approximations to these error functions by comparing data from two grids of different resolution. Berger and Oliger used the term "truncation error" to refer to what we have called "solution error", and thus in this chapter we will use their terminology in order to maintain consistency with related literature.

We begin on the base grid and integrate forward in time two steps. We also start with the same initial data on a grid with twice the mesh spacing as the base grid. Keeping the CFL factor $\lambda \equiv \Delta t / \Delta x$ the same as that used for the base grid, we evolve this coarse grid one step forward in time. The difference between the data on the coarse grid at this time and the data on the base grid (restricted to the coarse grid locations) gives a measure of the local truncation error. Those locations in the spatial domain which contain truncation errors larger than some user-defined threshold value are "flagged" as points where finer resolution is needed.

85

At this point there needs to be an algorithm for determining how the flagged points will be covered by finer grids. Such an algorithm is called a "clustering algorithm", because by it we seek to cluster the flagged points into large regions which can be covered by finer grids. Great care must be given to how this algorithm will place the new grids, in order that maximum computational efficiency be achieved [12]. Covering a wide distribution of flagged points with only one or two large grids may be simple and direct but will waste large amounts of time computing data at locations which do not require high resolution (perhaps defeating the very purpose of using AMR). Too many small grids covering a collection of points may mean high communication costs, as well as require extra regridding work in later iterations. It is often helpful to define a grid slightly larger than the region of those points which need the fine resolution, such that the grid also covers nearby regions which may require refinement in the near future. If this "buffering" is done effectively, it will mean fewer flagged points in the future and thus less work for the clustering algorithm at a later time. After the points have been appropriately clustered, new grids are defined to cover the points appropriately. We call this "regridding."

We do not perform the tasks of measuring truncation error, clustering and regridding at every time step, but rather only at certain intervals (*e.g.* every four time steps), primarily because these tasks take nontrivial time away from the actual work of simulation. The assumption underlying this is that the features in the simulation will not change "too rapidly."

If the gridfunctions begin to lose their smoothness properties, the Richardson expansion starts becoming a poor measure of the truncation error, and a typical result of this is the allocation of fine grids which cover nearly the entire domain. Since this is an undesirable outcome, we require that the numerical evolution scheme be *dissipative* in order to try to enforce smoothness in the gridfunctions.

5.3   AMR vs. Higher-Order Unigrid

While AMR is one means of providing high accuracy in short time, another route which some researchers have taken is to use finite difference operators which are *better* approximations to the underlying partial derivatives. This is achieved by extending the Taylor series expansion of these derivatives to higher order, and the most common extension is to fourth order. While it can be rather difficult to construct such higher-order operators which still yield a stable evolution, the payoff provided by higher order schemes has been enough to lure some researchers to implement such evolution codes [59]. The payoff is in terms of the convergence behavior: For every doubling of the resolution in a second-order accurate code, the truncation error goes down by a factor of 4, but for the same refinement using a fourth-order accurate code, the truncation error goes down by a factor of 16. Thus even fairly modest resolution can with fourth-order codes provide extremely accurate solutions *for sufficiently smooth* phenomena. It is even to be expected in a variety of scenarios that higher-order unigrid will yield better results (*i.e.* faster results for a desired accuracy) than (second-order) AMR. If the AMR scheme is only second order, it will have to extend to very high levels of refinement to match the results from a well-resolved fourth-order unigrid code.

Given this observation, and the difficulties involved with developing a sophisticated AMR code, some have asked the question, "Why should we use AMR when fourth-order unigrid offers much better convergence?" An initial response stems from the fact that adaptive methods are in some sense designed to resolve small features in a simulation which may not be easily predictable from the initial data. AMR provides the functionality to track and resolve small-scale phenomena which might never appear in a unigrid simulation. Higher-order unigrid can do an excellent job for smooth data, but it still cannot resolve any features smaller than the (static) mesh spacing.

We should also point out that, given a sufficiently general AMR algorithm in which we can take unigrid implementations and use them more or less directly within the AMR code, and assuming that one can construct appropriate higher-order interpolation operators for this AMR code, then one should be able to incorporate *any* unigrid technique within the AMR code. Constructing the higher-order interpolation operators may be nontrivial, and one might find challenges along the boundaries of fine grids, but there is nothing in principle to prevent the inclusion of higher-order techniques within the AMR algorithm. Thus the development of high-order unigrid codes and AMR codes, while these may at present appear to be disparate and competing efforts, can in principle work together to provide significant increases in computing power.

5.4 The Need for Efficient Parallelization

Modern large-scale simulation packages are typically run on large-scale computer systems, which in recent times has meant some form of parallel computing model. Current parallel computing platforms can range from the distributed-memory-distributed-processing architecture of a cluster of PCs to a sophisticated distributed-shared-memory system like the SGI Origin 2000. Parallel computing is an excellent way for an application to gain enormous increases in speed, but only if that application *parallelizes well*, *i.e.* that the overall computation speed scales almost linearly with the number of processors.

Typical mesh-based simulations lend themselves well to "data-parallel computing", for which one performs domain-decomposition or "partitioning" on the data set and sends one piece of the data set to each processor. (For a distributed memory system, the size of each piece is then limited by the amount of memory available to a processor.) For unigrid applications, this partitioning can be fairly simple or even trivial, but for an adaptive computation the partitioning can be highly-nontrivial,

due to the need for even "load balancing" across all processors. This load balancing is essential if the computation speed is to scale with the number of processors.

Partitioning and load balancing aside, a principal difficulty for parallel grid-based simulations (adaptive or otherwise) lies in the need for different processors to communicate with each other. Typically this is seen along the boundaries of the individual subdomains being simulated on each processor. Communication cost scales not only with the topology of the grid, but also with the number of processors. Communication costs are typically determined on the basis of the *latency* and *bandwidth* of the network [84]. The *latency* of a communications network is the so called "startup cost" required to establish a connection to send a message. The latency is independent of the length of the message. *Bandwidth* refers to the capacity of a communications channel (a specific path through the network) to transmit information, and is typically given in bits per second (bps).

Given a system with fixed bandwidth and latency, one can imagine there is some optimum problem size for a given number of processors, or conversely an optimum number of processors for a given problem size [84]. Taking the latter view, we can see that if we were to break up the domain into very tiny pieces and distribute it on many, many processors, the communication costs would prohibit a timely solution of the problem. Alternatively, if we divide the domain into only a few pieces on a few processors, the inter-processor communication cost will be low, but then we would not be taking advantage of the parallel supercomputer. From this, we can understand that for large computations on many processors, the inter-processor communication can be so costly that one can begin to see *negative* or *inverse* scaling, i.e. the user would be better off re-running the simulation on fewer processors.

For grid-based-simulation codes, the need is not so much for one processor to communicate with other *processors*, but simply to access the *memory* to obtain data

which were computed using other processors. Thus (as realized by Cray and others) as long as the "memory link" is fast enough, the inter-processor communication *per se* is not much of an issue. However, shared-memory architectures like the older Cray supercomputers are falling out of fashion. On PC clusters, if one wants to access the memory on another motherboard, *i.e. in a different machine*, one has to do so through the processor(s) on the other motherboard, via a network connection.

For an adaptive mesh code, communication costs are not easy to anticipate. One could imagine a scenario (admittedly extreme) in which an adaptive mesh code, because of high amounts of inter-processor communications, could actually take *longer* to execute than the corresponding unigrid code which renders a solution at the same accuracy as the adaptive code.

In summary, if one wants to write a parallel AMR code, great care is required in writing the code to help ensure load balancing and the use of the most efficient communications as possible.

5.5   Towards Automatic, Parallel AMR

Both AMR and parallelism are very desirable qualities to have in a simulation code, but both require significant effort to implement. We note, however, that many of the same tasks will be performed by any AMR simulation. These include the allocation and deallocation of memory for new grids, interpolation of coarsely-resolved data onto fine grid cells (what we call "prolongation"), truncation error estimation and clustering (for Berger and Oliger codes), message passing between processors, parsing of parameters, and general input and output. Given the generic aspects of these tasks (*i.e.* they are largely independent of the physical problem being modeled), one can imagine a computing environment in which these functions are provided as part of the package, thus freeing the user to concentrate on the physics at hand. In particular, one might desire an environment in which a user

supplies a set of finite difference equations, initial data, and boundary conditions written for the solution of his or her problem on a single uniform grid, but in which all the above-mentioned necessary components of a parallel AMR code are then generated automatically.

5.6   An Implementation of Berger and Oliger's Method

For our implementation of Berger and Oliger's method, we require that new grids share boundaries with (collections of) coarse grid cells. This means that we do not allow grids with arbitrary orientation, but rather only grids with boundaries parallel to those of the base grid.

5.6.1   Shadow Hierarchy

In addition to the integration of the equations of motion on the grid hierarchy, we also continuously evolve the data on a precise copy of the grid hierarchy in which all grids are coarsened by a factor of two. We call this coarsened copy of the grid hierarchy a *shadow hierarchy* [27], and the original hierarchy the *base hierarchy* or *main hierarchy*. The shadow hierarchy is used at regridding times to estimate the local truncation error. The usual implementation of the Berger and Oliger method amounts to the definition of a shadow hierarchy at each regridding time, so we choose to be spared the effort of allocating and de-allocating storage every regridding time and simply allow the shadow hierarchy to exist at all times. More importantly, the shadow hierarchy eliminates the need to duplicate *fine grid* storage at regridding times, which is a requirement of the original implementation of the Berger and Oliger method. Thus we save memory and computing time. The price we pay for this is that we evolve data on the shadow hierarchy at *all* times, not just the regridding times, but the hope is that the time we save in not duplicating fine grid storage at each regridding time makes up for this cost. The 2 : 1 refinement between

the base and shadow hierarchies requires a refinement ratio of $2^p : 1$ between each grid level, where p is some integer. In our software, p is required to be 1.

5.6.2   Refinement of Initial Data

Providing proper specification of the data and grid structure at the initial time is at least as complicated as the AMR evolution of the data. We wish to ensure that we begin the simulation with sufficient mesh refinement to adequately resolve all the features of the initial data, such that the evolution does not acquire large amounts of truncation error from the first evolution step. The initial regridding algorithm can be summarized by the following pseudo-code:

gfs = All grid functions to be evolved (reside on Main and Shadow hierarchies)
l = Current level in do loop
l_f = Finest level currently allocated
$l_{\max}$ = Finest level allowed in the simulation
te = local truncation error, a grid function
G_l = List of locations for new grids, obtained from clustering algorithm

Assign initial data on Main, level = 0
Assign initial data on Shadow, level = 0

$l := 0$, $l_f := 0$
Repeat until (l_f does not change) or ($l = l_{\max}$)
    $l := l + 1$
    Take two steps on Main at level l
    Take one step on Shadow at level l
    Measure truncation error: te = gfs(Shadow) - gfs(Main)
    Flag bad points: flags = where (te > Threshold)
    Cluster flagged points for placement of new grids: G_l = Cluster(flags)
    if (G_l not empty) then
        $l_f := l_f + 1$
        Allocate new grids on l_f at locations specified by G_l
        Assign initial data on Main, level = $0...l_f$
        Assign initial data on Shadow, level = $0...l_f$
    end if
end Repeat

Figures 5.1 and 5.2 show a series of steps in the refinement of initial data consisting of a sharply-peaked gaussian.

5.7   Our Software

We are working to provide what we call a *generic driver* for parallel AMR applications. This generic driver is intended to run a simulation using user-provided subroutines for (unigrid) integration of the equations of motion.

5.7.1   Infrastructure Provided by GrACE

The main set of routines for handing the operations on grids, and all aspects of parallelism, is provided in a package called GrACE written by Manish Parashar. In earlier versions, GrACE was known as DAGH [78]. GrACE is an object-oriented set of programming abstractions which provides the abstract programming interfaces for the allocation and de-allocations of grids, maintenance of the grid hierarchy, prolongation and restriction, and other operations involving grids. The clustering algorithm supplied by GrACE is due to Paul Walker [101]. A similar clustering code written by Reid Guenther [44] has been shown by Dae-Il Choi [20] to yield results similar to those of Walker's code.

5.7.2   Example: Solving 2D wave equation

The wave equation provides a natural hyperbolic system from which users may develop their own simulations. (We choose the wave equation rather than the transport equation mainly because the intended applications typically involve simulation of wave-like phenomena.) The examples we provide are in two spatial dimensions, but the extension to three such dimensions is straight forward. We give three different implementations for the solution of the 2D wave equation, and these go by the names `wave2d`, `wave2d1o`, and `amrwave2d1o`. The `wave2d` example is a unigrid
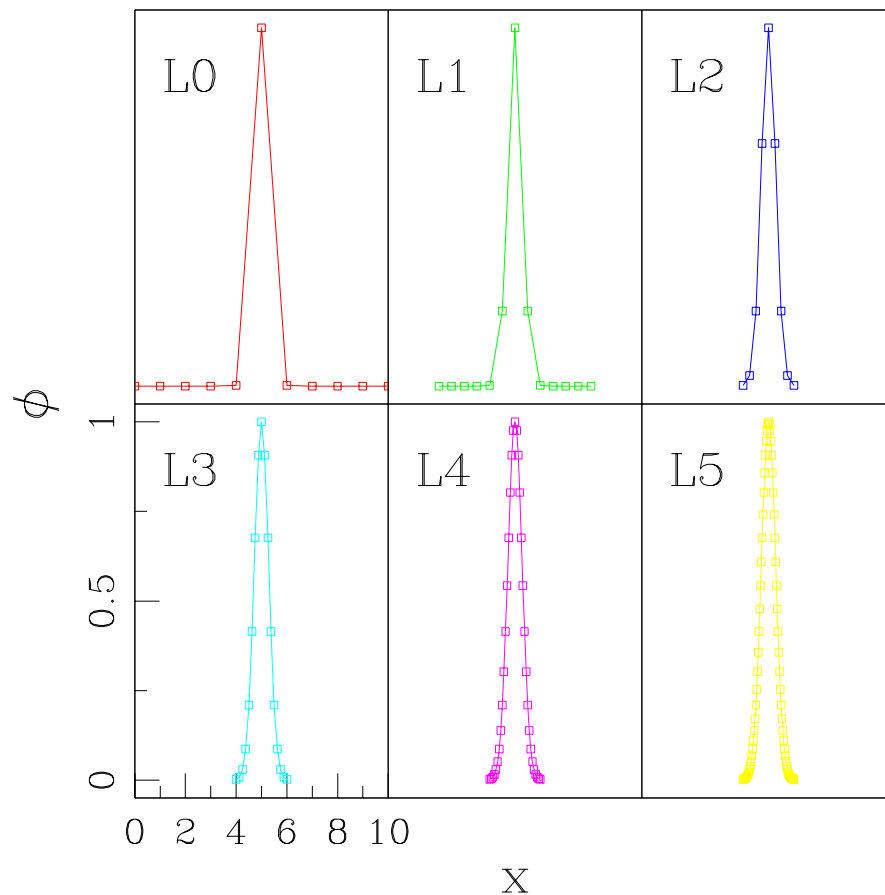
Figure 5.1: Initial grid refinement of a sharply peaked gaussian ϕ. Here we see six different levels of refinement for the initial time in the evolution of sharp gaussian pulse, on the domain $(0,0) \leq (x,y) \leq (10,10)$. Data is shown on the main hierarchy, with refinement levels are denoted by Ll, where $l = 0$ is the base grid and $l = 5$ is the finest grid. Currently the computing infrastructure supplied by GrACE (see section 5.7.1) is configured such that new grids are required to share boundaries with the coarsest grid cells, hence the grids for levels 3, 4, and 5 span a domain which is twice the width of a level 0 grid cell. (This requirement will be relaxed in a forthcoming version of GrACE.) The corresponding truncation error measured on each grid is shown in Figure 5.2.
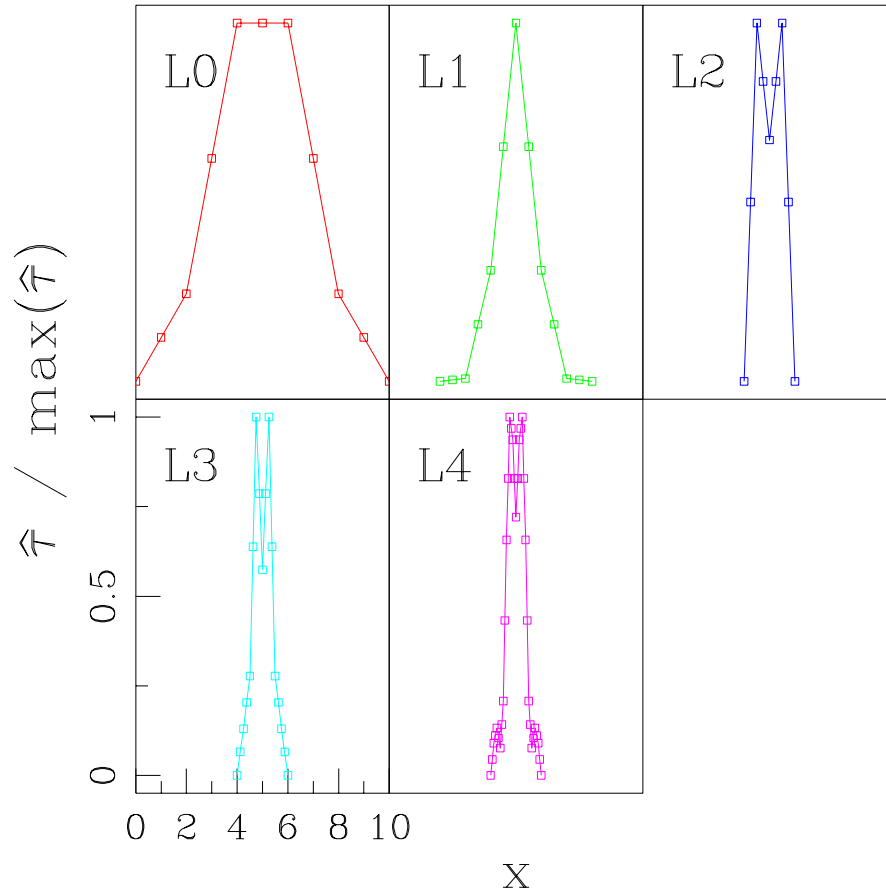
Figure 5.2: Truncation error $\hat{\tau}$ for the initial grid refinement of a sharply peaked gaussian shown in Figure 5.1. The truncation error threshold, used for flagging data points in need of further refinement, was $\hat{\tau} = 0.7 \max(\hat{\tau})$, where $\max(\hat{\tau})$ is the maximum value of the truncation error on each grid. Since the evolution scheme is second-order accurate, we expect the leading order truncation error to go as $\partial^3 \phi / \partial x^3$, yet we see from this figure that the truncation error we obtain does not fit the profile of the third derivative of a gaussian (which should be an *odd* function, and the above graph shows *even* functions), and thus the computer code is not yielding the expected results. This requires further study.

implementation of the usual wave equation expressed in terms of second-order partial derivatives. This can be executed on one or many processors via MPI. For the Berger and Oliger system, it is absolutely essential to employ an evolution scheme which is dissipative, in order to maintain the necessary smoothness of grid functions and to avoid "over-gridding", *i.e.*, applying fine resolution to large areas of the domain (where such resolution is unnecessary) as a result of poor truncation error estimation. In practice, we often prefer numerical schemes in which the dissipation is added explicitly, and we know how to add dissipative terms such as B.5 for hyperbolic systems cast in *first-order* form. With this in mind we provide a recasting of `wave2d` into first-order form, called `wave2d1o`. This implementation endowed with the necessary AMR routines is called `amrwave2d1o`.

Figure 5.3 shows a 1D slice through a 2D AMR evolution using `amrwave2d1o`. Full 2D visualization capabilities for AMR data are still under development. Manish Parashar wrote a set of routines for use with the AVS visualization package [1] which do provide visualization of 2D AMR data, however this software package is not readily available to many researchers.

5.7.3 Implementation of 'Generic Driver'

The generic driver should ideally be able to take a set of user-supplied update and initialization routines which were written for a sequential, unigrid application and generate a complete parallel AMR code. The caveat to this statement is that it should be able to take an *appropriately written* set of user-supplied routines and generate a parallel AMR code. Essentially, this means routines which are written to operate on a uniform subset of the computational domain and which check (internally) to determine if this subset includes real, physical boundaries. In practice, it may take some work for a user to modify an existing sequential unigrid to run in parallel, but from there the transition to parallel AMR could be quite smooth.
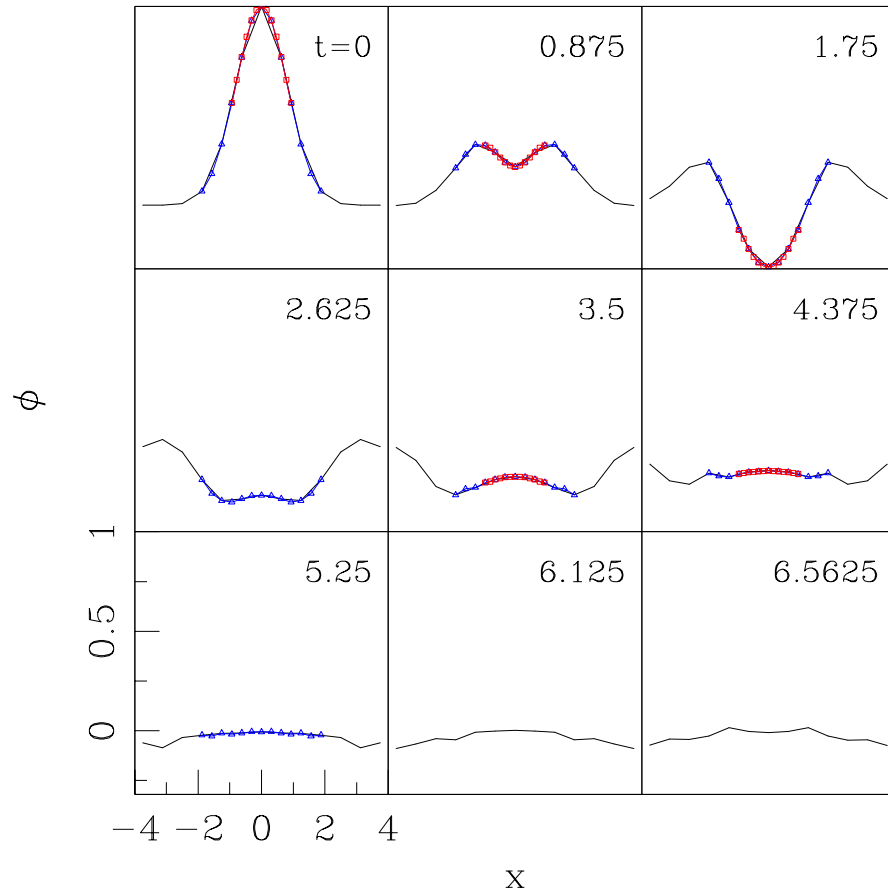
Figure 5.3: Animation of a 1D slice through a 2D evolution of the wave equation. This shows the evolution of the massless scalar field ϕ (in Cartesian flat space) from an initial gaussian pulse with $\dot{\phi} = 0$. Three levels of refinement are shown: Level 0 (base grid) data is shown as a solid (black) line, where we have omitted showing the data points themselves to more clearly show the data on additional levels. Level 1 data is shown as (blue) triangles, and Level 2 data as (red) squares. The domain is $(0,0) \le (x, y) \le (10, 10)$, and we take the 1D slice along $y = 5$.

We intend to integrate the generic driver with the compiler for the Rapid Numerical Prototyping Language (RNPL), a programming language developed by Robert Marsa and Matthew Choptuik [69]. RNPL is designed to allow users to write unigrid, sequential finite difference simulation codes with minimal effort. RNPL provides automatic support for routine tasks such as I/O and memory management, and allows the user to focus on the "physics" of interest. Thus RNPL allows for significant reductions in development time. The user specifies initial data, boundary conditions, and update routines in a symbolic form, and the RNPL compiler generates a complete simulation code (in Fortran, C or C++). An ultimate goal of our project is to have the RNPL compiler generate a fully functional parallel AMR application from RNPL source code.

5.8 Present and Future Projects

The specific goal of this project is for full integration with RNPL, so that authors of RNPL source can generate parallel AMR applications automatically. Currently the `amrwave2d1o` code serves as a minimal 'generic' driver, in which the user can replace the update routines and some function calls in the code with their own expressions.

Prior to my work on this project, previous implementations by Mijan Huq, Manish Parashar, Dae-Il Choi, Robert Marsa, Matthew Choptuik and Tom Goodale were available. Huq and Parashar wrote a 2D wave equation solver, as did Choi. Parashar and Goodale later provided a dual 2D/3D wave equation solver. Marsa and Choptuik had written a package called `bbh_dagh`, which used Parashar's DAGH library (the predecessor to GrACE) and included a parallel unigrid code for solving the 2D wave equation, using many of the constructs in the `bbhutil` library which are shared with RNPL. My work consisted of selecting from these different packages the most useful routines and rewriting many of them to serve the purposes of a generic driver.

The result is `bbh_grace` [55], an update of Marsa and Choptuik's `bbh_dagh` distribution which includes Parashar's newest GrACE library, provided in a form which can automatically configure itself on a variety of computing platforms. This includes a 2D wave equation solver featuring parallel AMR, using a three-level leapfrog update scheme (previous implementations featured only two-level schemes such as MacCormack predictor-correctors). I rewrote the initial regridding routines of Choi to provide a clear interface with the recursive integration routines of Parashar, and to allow for a three-level update scheme. I made two improvements to the existing dissipation operator, first by removing a cause of asymmetry induced by the "weighted-average" operator being used, and secondly by replacing this (first-order-accurate) operator with the second-order-accurate Kreiss-Oliger dissipation operator. I isolated elements of the code which would be "user-supplied" in the "generic driver" scenario, in which the user supplies only unigrid updates and initialization routines and automatically obtains a parallel AMR code. I expanded the capabilities of GrACE by writing an additional reliable interface for visualization of 1D slices through the 2D data (an interface to Matthew Choptuik's `ser` [22], which offers many features for data analysis not provided by `xgraph` [49], which was the only 1D visualization package with which GrACE was designed to interface), and a utility to provide visualizations of the global grid structure as a function of time. I began developing documentation to supplement the existing GrACE/DAGH documentation. I added a feature for overriding the clustering algorithm to obtain regridding directives from a file, which I used to perform convergence testing of AMR evolutions. I interacted regularly with Parashar, and provided constructive feedback regarding the features of GrACE and the previous parallel AMR implementations mentioned above. As a first step toward integration with RNPL, I wrote a simple generic driver, using template files (which obey a simple, expandable and generic HTML-like language I developed) and employed this with great efficiency

toward the creation of a 2D parallel AMR hydrodynamics solver (albeit one which was not perfectly flux-conservative) using existing sequential hydrodynamics update routines. This demonstrated viability of the generic driver idea. In summary, I developed a cohesive and portable package which serves as a prototype for generic parallel AMR applications, containing many of the features and utilities desired by developers of computational physics applications. However, this code still has difficulties which remain to be fully resolved; as we saw in Figure 5.2, the truncation error estimation, a key aspect of the Berger and Oliger scheme, is not yielding the expected results. This is perhaps the most significant piece of work which needs to be completed in the near future.

Two additional features which we consider necessary for the generic driver are the provision of 1D coordinate grid functions (*e.g.* x, y) for update routines and a "characteristic function" or "mask" to encode information about boundary conditions and other special points on the grid. We would also like to provide a generic interface which is Fortran 77 compliant (the present version of GrACE provides subroutine headers for Fortran 90) and a simple interface to GrACE's checkpointing capabilities. These efforts are all underway and should be incorporated into the software shortly.

Visualization remains an issue. It is our desire to provide visualization tools for `bbh_grace` which can be obtained by many researchers at minimal cost. Preliminary work involving the Iris Explorer [19] package using its curvilinear lattice data format has been promising. A first step in this direction may be the development of a program which collates the various data files generated in an `amrwave2d1o` run and outputs a single Explorer lattice file. A group led by John Shalf at NCSA is developing a publically-available software package for visualization of AMR data. This package is called LCA Vision [94], and it is compatible with the IEEE output which `bbh_grace` can output using GrACE's output routines.

The goal of providing an environment for automatic development of parallel AMR applications has not yet been realized, but the work presented here represents a nontrivial step toward the fulfillment of this goal.

Chapter 6

Scalar Accretion

This section of the dissertation represents work in progress to simulate the dynamics of the Maxwell-Massive-Klein-Gordon (MMKG) system around a spinning black hole. Such a system may have features similar to those found in magnetohydrodynamic accretion accretion studies [53, 63]. Currently we are working toward an axisymmetric simulation on a Kerr background.

It has long been known that evolution of a linear scalar test field in the Kerr spacetime can be solved via separation of variables [18]. The governing PDEs are thereby reduced to a system of ODEs, greatly simplifying the problem. Similarly, Maxwell's equations in vacuum can be also solved on a Kerr background by separation of variables [97]. The reader may therefore wonder why we may be interested in using finite difference techniques to solve for the evolution of scalar and electromagnetic fields on a Kerr background. In our system the scalar field acts as a source for the electromagnetic fields, and vice versa. The coupling between these fields is *nonlinear*. The author is not aware of any solution to this coupled system using separation of variables. Beyond this, the solution of this problem serves as a valuable stepping stone toward the solution of the magnetohydrodynamic equations in the vicinity of the black hole (which is not expected to be obtainable via separation of
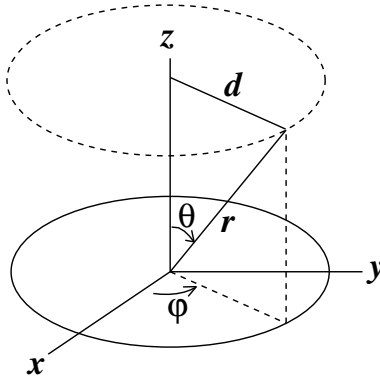
Figure 6.1: Relationship between spherical coordinates $(t, r, \theta\varphi)$ and cylindrical coordinates (t, d, z, φ) (We choose the letter d because r and ρ are already employed in the form of Kerr-Schild metric.).

variables except for a few simple cases).

6.1 Mathematical Preliminaries

6.1.1 Equations of Motion

We use the Kerr metric in spherical Kerr-Schild coordinates (t, r, θ, φ) to derive the equations of motion for the scalar and Maxwell fields, because the Kerr metric takes on a fairly simple form in these coordinates. Having obtained the equations of motion, we will want to perform the simulation in cylindrical Kerr-Schild coordinates (t, d, z, φ) (see Figure 6.1) because the numerical treatment of the axis is less difficult in these coordinates than in spherical coordinates. Thus we will find it helpful to hold both coordinate systems in mind, with the transformations

$$d = r \sin \theta \quad z = r \cos \theta$$

relating the two systems.

In spherical coordinates, then, the metric takes the form

$$
g^{\mu\nu} = \begin{pmatrix}
-1/\alpha^2 & \beta/\alpha^2 & 0 & 0 \\
\beta/\alpha^2 & 1/b^2 + a^2\sin\theta/\rho & 0 & a/\rho^2 \\
0 & 0 & 1/\rho^2 & 0 \\
0 & a/\rho^2 & 0 & 1/\left(\rho^2\sin^2\theta\right)
\end{pmatrix}
$$

For the case of $a = 0$, this is the same form of the metric used in Chapters 3, and 4 (with variable a in Chapters 3 and 4 replaced by the letter b to avoid confusion with the black hole spin parameter). For the Kerr background, we have the relations

$$
\alpha^2(r,\theta) = \left(1 + \frac{2Mr}{\rho^2}\right)^{-1} = \frac{\rho^2}{\rho^2 + 2Mr}
$$

$$
b(r,\theta) = \frac{1}{\alpha}
$$

$$
\beta(r,\theta) = \frac{2Mr}{\rho^2 + 2Mr}.
$$

The square root of the determinant of the metric is

$$
\sqrt{-g} = \alpha b \rho^2 \sin\theta.
$$

The equations of motion for the scalar field $\psi(t,r,\theta,\varphi)$ and the gauge field $A_\mu(t,r,\theta,\varphi)$ are given by

$$
\Box\psi = U(|\psi|)\psi - ieA_\mu g^{\mu\nu}(2\partial_\nu\psi + ieA_\nu\psi) - ie\nabla_\nu A^\nu\psi \tag{6.1}
$$

$$
\Box A_\mu + R_\mu{}^\nu A_\nu = ie\left(\phi^*\partial_\mu\phi - \phi\partial_\mu\phi^*\right) + 2e^2 A_\mu\phi\phi^*. \tag{6.2}
$$

Because the Kerr geometry is a vacuum spacetime, we know from Einstein's equation that the Ricci tensor that appears in (6.2) is zero. We choose the "Lorentz gauge" in (6.1) such that $\nabla_\nu A^\nu = 0$. This gauge condition then becomes a constraint that must be satisfied in addition to the equations of motion.

The equations of motion for the complex scalar field and the Maxwell field are fairly lengthy when fully written out as a system of first-order partial differential

equations in cylindrical coordinates. The inclusion of these equations, roughly a page each in LaTeX format, is not thought to benefit the reader in a significant way. The simulation code is currently not properly evolving the comparatively simple equations for one massless, uncharged real scalar field on the Kerr background. Thus we do not find it necessary or relevant to present the equations here.

6.1.2 Boundary Conditions

At the event horizon, the causal structure of the spacetime implies that we require no explicit boundary condition. Rather, we simply solve the equations of motion, using appropriate "forward" difference operators for spatial derivatives. We discuss these further below.

The outer boundary is more problematic. If we were simply considering a massless scalar field we could use the outgoing Sommerfeld condition for the scalar and electromagnetic fields. Since the scalar field has a nontrivial potential, both it and the electromagnetic fields to which it couples will not be well described by the Sommerfeld condition. Given that this simulation is a multidimensional one, the option of using a very distant outer boundary (as we did in Chapter 3) is not feasible. Another option involves varying the shift β, making $\beta(r, \theta) \to 1$ as $r \to \infty$. This sort of "montonically increasingly boosted" coordinate system has been shown to be very successful for a flat background spacetime [58], and it seems possible that this method would also work well on a curved background. The current simulation code is not equipped to use a shift other than the shift of KS coordinates, so this option has not been implemented. For the time being, while we improve other aspects of the code as well, the grid functions are simply held fixed at the outer boundary (*i.e.* we impose Dirichlet conditions at the outer boundary).

6.1.3 Initial Data

Our initial data can be specified largely arbitrarily, however it must satisfy certain constraints. One constraint is the Lorentz gauge condition,

$$\nabla_\nu A^\nu = g^{\nu\mu}\partial_\nu A_\mu + \Gamma^\nu_{\nu\mu}g^{\mu\sigma}A_\sigma = 0, \tag{6.3}$$

which must be satisfied on the initial spacelike hypersurface. We solve (6.3) using a simple prescription: To avoid solving an elliptic equation on the spacelike hypersurface, we solve for $\partial_t A_0$ using existing data for the other fields — which at the initial time would be freely specified. Since we are using the four-vector potential A_μ, we expect the magnetic field $B^i = \epsilon^{ijk}D_i A_j$ to satisfy the constraint $D_i B^i = 0$. In the work of J. Hawley and Evans [52], the authors note that for numerical evolutions involving smooth functions (such as scalar fields on a background spacetime), this expectation is warranted, however more sophisticated methods such as their "constrained transport" scheme are necessary for systems where the data are not expected to be smooth (*e.g.* in magnetohydrodynamic systems). Our final constraint is Guass' Law

$$D_i E^i = \rho_e, \tag{6.4}$$

where E^i is the electric field related to the Maxwell tensor $F_{\mu\nu}$ and the four-vector potential A_μ by

$$
\begin{aligned}
E^i &= F^{0i} \\
&= \delta^i_\gamma n_\mu \perp^\gamma_\nu F^{\mu\nu} \\
&= \delta^i_\gamma n_\mu \perp^\gamma_\nu g^{\mu\lambda}g^{\nu\sigma} F_{\lambda\sigma} \\
&= \delta^i_\gamma n_\mu \perp^\gamma_\nu g^{\mu\lambda}g^{\nu\sigma} (\nabla_\lambda A_\sigma - \nabla_\sigma A_\lambda)
\end{aligned}
$$

$n_\mu = (-\alpha, 0, 0, 0)$ is the normal unit one-form to the spacelike hypersurface, $\perp^\gamma_\nu$ is the projection tensor onto the spacelike hypersurface, and $\rho_e = j^0$, where

$$j^\mu = ie\,(\phi^*\partial^\mu\phi - \phi\partial^\mu\phi^*) + 2e^2 g^{\mu\nu}A_\nu\phi\phi^*.$$

106

York and Piran [102] discuss a method for solving (6.4) by decomposing E^i on the initial slice into longitudinal and transverse (divergence-free parts), $E^i = E^i_L + E^i_T$, allowing us to solve 6.4 as a Poisson equation

$$D_i E^i_L = D^i D_i U$$

where U is a scalar function. Thus we are required to solve an elliptic equation at the initial time. We intend to develop a multigrid solver to obtain the solution to this elliptic equation. For early computations, we will attempt to construct very simple initial data which satisfies the constraints in closed form, if possible.

With the initial data specified, we can then evolve all the fields independently ("free evolution") and use the constraints (6.3), (6.4) to check that the evolution is proceeding consistently, or we can solve the constraints on each spacelike hypersurface ("constrained evolution") to insure that the evolution proceeds as self-consistently as possible.

What sort of initial data would correspond to reasonable astrophysical scenarios? We might like to construct a sort of scalar MHD accretion disk, with the scalar field circling the black hole about the equatorial plane, and magnetic fields threading the disk and hole vertically. We would also need to specify initial time derivatives for the data. Given the available definitions of "velocity" for the scalar field (cf. Section 1.4.2), we would not expect to be able to construct a uniform "Keplerian" scalar accretion disk, but we may be able to construct at least a uniform mass distribution for the field, using the "boson star *ansatz*" $\psi \sim \exp(i\omega t)$. As an initial step, we simply consider axisymmetric initial data for an uncharged, massless scalar field. Then, having verified that the code operates properly for this simple case, we will add additional features such as mass and charge.

6.2 Numerical Methods

The simulation code, as it now stands, is intended to solve the Maxwell-Massive-Klein-Gordon equations in axisymmetry. The specifications are as follows: We use a Crank-Nicholson update scheme with Kreiss-Oliger dissipation (as described in the appendix). We excise a subset of the interior of the event horizon (including the singularity), and refer to the boundary of this excised region as the "inner boundary" of the computational domain. At the inner boundary, we impose no explicit boundary condition, but rather solve the usual equations of motion using "forward" and "backward" difference operators. As advocated by Choptuik [29], we use forward and backward difference operators which share the same leading order truncation error as the centered difference operators (2.8) used throughout the rest of the domain [29]. For example, the forward difference operator in the d-direction has the form

$$\partial_d u\big|_{d=i\Delta d, z=j\Delta z} \simeq \frac{-4u_{i,j} + 7u_{i+1,j} - 4u_{i+2,j} + u_{i+3,j}}{2\Delta z} \ .$$

Along the z-axis, we perform no finite difference operations because of the coordinate singularity, and instead interpolate between the points on either side of the axis.

The information regarding which difference operations should be performed (forward differencing, excision, interpolation, *etc.*) is encoded into the grid by means of a *characteristic* or *mask* function. This is simply a function defined over the entire grid, which contains different numeric (integer) values to denote points which should be excised, backwards differenced, and so on.

6.3 Status and Future Work

We are finding numerical instabilities near the inner boundary for $z < 0$, for the simplest case of a massless, uncharged real scalar field. The evolution near the inner

boundary for $z > 0$ seems to proceed properly, and we are investigating the cause of this error (and asymmetry) in the calculations. We hope to resolve this shortly, and then include the dynamics for the full Maxwell-Massive-Klein-Gordon system shortly thereafter. We currently have a 2D code for non-axisymmetric evolution of a scalar field in the equatorial plane of a Kerr background, which we hope to integrate with little difficulty with the axisymmetric code for a full 3D evolution.

Chapter 7

Conclusions

We have considered the dynamics of scalar fields in scenarios which have some correspondence to certain astrophysical systems. We studied the nonlinear dynamics of fairly simple systems composed of scalar fields in spherical symmetry, and yet we found a rich set of previously unknown phenomena. For the case of boson stars, we showed that it is possible to induce Type I critical behavior by imploding a spherical shell of massless real scalar field. We showed that there is mass exchanged between the two fields, and the complex (boson star) field enters a critical state which corresponds to an unstable boson star *modulo* the presence of a "halo" in the tail of the critical solution. This halo is presumed to be a remnant of the original (stable) boson star, and does not seem to be part of the "attractor", the critical solution. One interesting point raised by this work concerns the behavior of neutron stars under similar conditions: If the critical solutions (which can either implode to form black holes or explode) correspond to boson stars on the unstable branch, then unstable boson stars can explode; and if unstable boson stars can explode, then perhaps unstable neutron stars — which share macroscopic stability features with boson stars — can also explode.

The boson stars we considered are composed of complex fields in which the

real and imaginary parts act like two real scalar fields which are completely uncoupled, except via gravity. We showed that if we modify the temporal phase between these two component fields, it is possible to construct other star-like objects, which we have termed "multi-scalar stars". These objects persist as stable quasi-periodic solutions for very long times. We found, however, that the direct construction of truly periodic solutions via a Fourier cosine series *ansatz* did not yield the expected evolutions, but instead different periodic (or quasi-periodic) solutions. This requires further attention, yet our results, along with the seminal work by Seidel and Suen [90], indicate that stable, long-lived star-like solutions are more common than previously assumed.

The work regarding adaptive mesh refinement (AMR) represents nontrivial progress toward the goal of a computing environment in which authors of simulation codes for sequential, unigrid processing can add parallel AMR features essentially *automatically*. The work on initial data generation is the principal contribution in this area, however additional development tools have been created to help future developers of this computing environment. There is a problem with the truncation error estimation, which can which can result in costly overgridding. Further development and testing is necessary to produce a "programming systems product" [17] which will be useful to researchers worldwide.

Lastly we considered the simulation of a charged scalar field on a Kerr background. This was intended as a test problem for the AMR system, as a possible "toy model" of hydrodynamical accretion, and as a new dynamical study in its own right. We look forward to pursuing this investigation in the future, working towards the goal of simulating magnetohydrodynamical accretion in curved spacetimes.

Appendix A

Boson Star Mode Frequencies

In this appendix we have tabulated some sample values from the perturbation theory calculations described in Chapter 3. The values and uncertainties expressed in the table captions were determined by integrating (3.33) and (3.34) to various maximum radii, for a range of error tolerances in the integration routines. The values and uncertainties given in the tables were chosen to express the variation in our results.

Table A.1: Shooting Parameters: Fundamental Mode. The values of $\phi_0(0)$ are exact. Other quantities are given within an uncertainty of ± 1 in the last significant digit.

$\phi_0(0)$	ω	$\delta\lambda''(0)/\delta\psi_1(0)$	σ^2
6.0E-02	1.0417E+00	1.68E-01	0.28E-03
1.0E-01	1.0727E+00	0.29E+00	0.67E-03
1.4E-01	1.1067E+00	0.43E+00	1.11E-03
1.8E-01	1.1440E+00	0.59E+00	1.41E-03
2.2E-01	1.1849E+00	0.77E+00	1.31E-03
2.6E-01	1.2299E+00	0.98E+00	0.45E-03
2.7E-01	1.2419E+00	1.04E+00	0.05E-03
2.8E-01	1.2542E+00	1.10E+00	-0.43E-03
3.0E-01	1.2796E+00	1.24E+00	-1.71E-03
4.0E-01	1.4281E+00	2.08E+00	-1.84E-02
5.0E-01	1.6215E+00	3.45E+00	-7.09E-02
6.0E-01	1.8777E+00	5.79E+00	-2.11E-01

Table A.2: Shooting Parameters: First Harmonic Mode. The values of $\phi_0(0)$ are exact, ω is given within an uncertainty of ± 1 in the last significant digit, and the other quantities are given within an uncertainty of ± 2 in the last significant digit.

$\phi_0(0)$	ω	$\delta\lambda''(0)/\delta\psi_1(0)$	σ^2
6.00E-01	1.8777E+00	0.63E+01	0.22E+00
7.00E-01	2.2230E+00	1.13E+01	0.32E+00
8.00E-01	2.6963E+00	2.09E+01	0.43E+00
9.00E-01	3.3536E+00	4.11E+01	0.53E+00
1.00E+00	4.2714E+00	0.84E+02	0.54E+00
1.10E+00	5.5471E+00	1.77E+02	0.42E+00
1.12E+00	5.8555E+00	2.07E+02	3.05E-01
1.14E+00	6.1842E+00	2.41E+02	1.46E-01
1.15E+00	6.3566E+00	2.59E+02	4.30E-02
1.16E+00	6.5346E+00	2.80E+02	-8.11E-02
1.17E+00	6.7184E+00	3.02E+02	-2.28E-01
1.18E+00	6.9083E+00	3.26E+02	-4.01E-01

Appendix B

Finite Difference Algorithm for Spherically-Symmetric Evolution Code

This appendix describes the numerical evolution scheme used in Chapters 3 and chap:msschap. We approximate the continuum field quantities $\{\alpha, a, \Pi_1, \Pi_2, \Pi_3,$ $\Phi_1, \Phi_2, \Phi_3, \phi_1, \phi_2, \phi_3\}$ by a set of *grid functions*, quantities which are obtained via the solution of finite difference approximations to the partial differential equations (3.8), (3.11) - (3.14) on a domain which has been discretized into a regular mesh (*i.e.* lattice) with mesh spacing Δr in space and Δt in time. For a grid function u, we denote the value of the grid function in the mesh location j in space and n in time by u_j^n, *e.g,*

$$\alpha_j^n \simeq \alpha\left(n\Delta t, (j-1)\Delta r\right),$$

where $\alpha\left(n\Delta t, (j-1)\Delta r\right)$ is the corresponding value for the continuum solution.

The initial data is obtained via "shooting", a standard method of solving ordinary differential equations, in a way essentially the same as that found in [86].

The numerical method used for evolving the system of equations is a *leapfrog scheme*, which is an explicit scheme requiring data at two previous time steps, n and $n-1$, to compute a value at the next time step $n+1$. Given a discretization of scale of order h in time and space, the leapfrog scheme is $\mathcal{O}(h^2)$ accurate. Throughout the mesh, the ratio $\lambda_{\text{CFL}} \equiv \Delta t / \Delta r$ is kept at a constant value, which must be less than unity due to the stability requirements of the leapfrog scheme.

To aid in the presentation of the difference equations, we define the following operators [23]:

$$\Delta_0^t u_j^n = \frac{u_j^{n+1} - u_j^{n-1}}{2\Delta t}$$

$$\Delta_0^r u_j^n = \frac{u_{j+1}^n - u_{j-1}^n}{2\Delta r}$$

$$\Delta_+^r u_j^n = \frac{u_{j+1}^n - u_j^n}{\Delta r}$$

$$\Delta_3^r u_j^n = 3\frac{u_{j+1}^n - u_{j-1}^n}{(r_{j+1})^3 - (r_{j-1})^3}.$$

We also define the averaging operator

$$\mu_+^r u_j^n = \frac{1}{2}\left(u_{j+1}^n + u_j^n\right),$$

which takes precedence over other algebraic operations, *e.g.*

$$\mu_+^r \left(\frac{fg^2}{h}\right) = \frac{\mu_+^r f_j^n \left(\mu_+^r g_j^n\right)^2}{\mu_+^r h_j^n}.$$

The evolution equations, which are applied to each field $\{\Phi_i, \Pi_i, i = 1, 2, 3\}$ can then be written as:

$$\Delta_0^t \Phi_j^n = \Delta_0^r \left(\frac{\alpha}{a}\Pi\right)_j^n \tag{B.1}$$

$$\Delta_0^t \Pi_j^n = \Delta_3^r \left(\frac{r^2\alpha}{a}\Phi\right)_j^n - 2\left(\alpha a\phi\right)_j^n \tag{B.2}$$

where the last term in the evolution equation for Π is not applied to the massless field.

Our boundary conditions are as follows: First, by regularity at the origin, we have

$$\Phi_1^n = 0$$

for all n. To obtain Π_1^{n+1} we employ a "quadratic fit" at the advanced time,

$$\Pi_1^{n+1} = \frac{4\Pi_2^{n+1} - \Pi_3^{n+1}}{3}, \tag{B.3}$$

which is based on the regularity condition, $\lim_{r\to 0}\Pi(t, r) = \Pi_0(t) + r^2\Pi_2(t) + \cdots$.

A significant challenge in the numerical solution of these equations is the problem of the outer boundary condition for the massive field. Numerous authors have proposed methods to handle this. Having tried various methods including first order expansions of the dispersion relation [89], sponge filters [60], and operator splitting [7], we were unable to obtain a scheme which produced results superior to the simple Sommerfeld condition one uses for massless fields [54]. Since, however, the Sommerfeld condition is still inadequate for massive fields, we have chosen to run our simulations on a grid large enough that the outer boundary is out of causal contact with the region of interest for the time the simulation runs. So, for example, if we are interested in a region $0 \le r \le 50$ and times $0 \le t \le 400$, then we place the outer boundary $r_J \ge 450$. (While unbounded phase velocities are a feature of the Klein-Gordon equation, we can argue on physical grounds as well as see quite clearly in simulations that it is the group velocity which is the important quantity in the numerical evolutions, and this is sub-luminal.) Recent work using a shifted coordinate system, with a shift vector that is vanishing in some region near $r = 0$ but increases to unity as $r \to r_J$, shows promise as a means of handling the challenge of the boundary condition for the massive field [58], and this method may be employed in future work. Thus the outer boundary condition we employ is [26]:

$$\Phi_J^{n+1} = \left(\frac{3}{\Delta t} + \frac{3}{\Delta r} + \frac{2}{r_J} \right)^{-1} \left(\frac{4\Phi_J^n - \Phi_J^{n-1}}{\Delta t} + \frac{4\Phi_{J-1}^{n+1} - \Phi_{J-2}^{n+1}}{\Delta r} \right) \qquad \text{(B.4)}$$

and an analagous equation is used for each Π variable.

After these evolved variables are obtained at the $n+1$ time step, we apply a form of numerical dissipation advocated by Kreiss and Oliger [65]. This is applied to both Φ_j^{n+1} and Π_j^{n+1} in the same manner. So, for instance we set

$$\Phi_j^{n+1} := \Phi_j^{n+1} - \frac{\epsilon}{16} \left(\Phi_{j+2}^{n-1} - 4\Phi_{j+1}^{n-1} + 6\Phi_j^{n-1} - 4\Phi_{j-1}^{n-1} + \Phi_{j-2}^{n-1} \right), \qquad \text{(B.5)}$$

where ϵ $(0 < \epsilon < 1)$ is an adjustable parameter: typically, we use $\epsilon = 0.5$.

The preceeding equations describe the "evolution" aspect of the code. The other variables are evolved in a "constrained" manner, $i.e.$ they are obtained on the spacelike hypersurface $n+1$ after the fields Φ_j^{n+1} and Π_j^{n+1} have been calculated. The field values ϕ_j^{n+1} are obtained by updating the value at the outer boundary $j = J$ according to

$$\Delta_0^t \phi_J^n = + \left(\frac{\alpha}{a} \Pi \right)_j^n \qquad \text{(B.6)}$$

and then integrating $inward$ from $j = J$ to $j = 1$ along the spatial hypersurface at $n+1$:

$$\Delta_+^r \phi_j = \mu_+^r \Phi_j. \qquad \text{(B.7)}$$

The Hamiltonian constraint (3.11) can be solved at each time step once all the field variables have been computed for the advanced time step. We use the variable $A \equiv \ln a$ to avoid loss of precision near the origin in the following finite difference approximation, which is evaluated at the advanced time step $n+1$:

$$\Delta_+^r A_j = \mu_+^r \left(\frac{1 - e^A}{2\,r} + \frac{r}{2} \left[\Pi_1^2 + \Pi_2^2 + \Pi_3^2 + \Phi_1^2 + \Phi_2^2 + \Phi_3^2 + e^A \left(\phi_1^2 + \phi_2^2 \right) \right] \right)_j.$$
$$\text{(B.8)}$$

This equation is solved using a *pointwise* Newton iteration, *i.e.* given a value of A_j^{n+1} (such as $A_1^{n+1} = 0$ at the origin), we find the next value A_{j+1}^{n+1} outward along the spatial hypersurface by solving (B.8) via Newton's method.

The slicing condition can be solved once the field variables and the metric function a have been obtained at the advanced time step, using the following linear algebraic relation:

$$\alpha_{j+1}^{n+1} = \alpha_j^{n+1} \cdot \frac{(1/\Delta r) + Z}{(1/\Delta r) - Z}, \qquad (B.9)$$

where

$$Z \equiv \mu_+^r \left(\frac{a^2 - 1}{2r} \right)_j + \frac{\Delta_+^r a_j}{\mu_+^r a_j} - \mu_+^r \left[r a^2 m^2 \left(\phi_1^2 + \phi_2^2 \right) \right]_j .$$

Appendix C

Details of Linear Stability Analysis

This appendix describes the details regarding the boson star stability analysis discussed in Chapter 3. Following Gleiser and Watkins [43], we write the most general time-dependent, spherically-symmetric metric as

$$ds^2 = -e^{\nu(t,r)}dt^2 + e^{\lambda(t,r)}dr^2 + r^2 d\Omega,$$

and decompose the complex massive field $\phi(t,r)$ via

$$\phi(t,r) = [\psi_1(t,r) + i\psi_2(t,r)]e^{-i\omega t}, \qquad (C.1)$$

where ψ_1 and ψ_2 are real.

In these variables, the Hamiltonian constraint and slicing condition can be written as

$$\lambda' = \frac{1 - e^\lambda}{r} + r\left(e^{\lambda-\nu}\left[(\dot\phi_1 + \omega\psi_2)^2 + (\dot\phi_2 - \omega\psi_1)^2\right] + \psi_1'^2 + \psi_2'^2 + e^\lambda(\psi_1^2 + \psi_2^2)\right) \qquad (C.2)$$

$$\nu' = \lambda' + 2\frac{e^\lambda - 1}{r} - 2re^\lambda(\psi_1^2 + \psi_2^2) \qquad (C.3)$$

where a prime ($'$) denotes $\partial/\partial r$ and an overdot ($\dot{}$) denotes $\partial/\partial t$.

The Klein Gordon equation yields:

$$\psi_1'' + \left(\frac{2}{r} + \frac{\nu' - \lambda'}{2}\right)\psi_1' \quad + \quad e^\lambda\left(e^{-\nu}\omega^2 - 1\right)\psi_1 - e^{\lambda-\nu}\ddot{\psi}_1$$

$$+ \quad e^{\lambda-\nu}\frac{\dot{\nu} - \dot{\lambda}}{2}(\dot{\psi}_1 + \omega\psi_2) - 2e^{\lambda-\nu}\omega\dot{\psi}_2 = 0 \quad \text{(C.4)}$$

and

$$\psi_2'' + \left(\frac{2}{r} + \frac{\nu' - \lambda'}{2}\right)\psi_2' \quad + \quad e^\lambda\left(e^{-\nu}\omega^2 - 1\right)\psi_2 - e^{\lambda-\nu}\ddot{\psi}_2$$

$$+ \quad e^{\lambda-\nu}\frac{\dot{\nu} - \dot{\lambda}}{2}(\dot{\psi}_2 - \omega\psi_1) + 2e^{\lambda-\nu}\omega\dot{\psi}_1 = 0. \quad \text{(C.5)}$$

Another equation we will find useful is $G_\theta^\theta = 8\pi G T_\theta^\theta$, which evaluates to

$$e^{-\lambda}\left(\frac{\nu' - \lambda'}{2r} + \frac{1}{2}\nu'' + \frac{1}{4}\nu'^2 - \frac{1}{4}\nu'\lambda'\right) - e^{-\nu}\left(\frac{1}{2}\ddot{\lambda} + \frac{1}{4}\dot{\lambda}^2 - \frac{1}{4}\dot{\nu}\dot{\lambda}\right)$$

$$= \quad e^{-\nu}\left(\dot{\phi}_1^2 + \dot{\phi}_2^2 + 2\omega(\dot{\phi}_1\psi_2 - \dot{\phi}_2\psi_1) + \omega^2(\psi_1^2 + \psi_2^2)\right)$$

$$-e^{-\lambda}(\psi_1'^2 + \psi_2'^2) - (\psi_1^2 + \psi_2^2). \quad \text{(C.6)}$$

We use equations (C.2) through (C.4) to obtain the equilibrium solutions, by setting

$$\lambda(t,r) \quad = \quad \lambda_0(r) \quad\quad\quad\quad \text{(C.7)}$$

$$\nu(t,r) \quad = \quad \nu_0(r) \quad\quad\quad\quad \text{(C.8)}$$

$$\psi_1(t,r) \quad = \quad \phi_0(r) \quad\quad\quad\quad \text{(C.9)}$$

$$\psi_2(t,r) \quad = \quad 0. \quad\quad\quad\quad \text{(C.10)}$$

The equilibrium equations are then given by:

$$\lambda_0' = \frac{1 - e^{\lambda_0}}{r} + r\left[e^{\lambda_0}(\omega^2 e^{-\nu_0} + 1)\phi_0^2 + \phi_0'^2\right] \quad\quad \text{(C.11)}$$

$$\nu_0' = \frac{e^{\lambda_0} - 1}{r} + r\left[e^{\lambda_0}(\omega^2 e^{-\nu_0} - 1)\phi_0^2 + \phi_0'^2\right] \quad\quad \text{(C.12)}$$

120

$$\phi_0'' = -\left(\frac{2}{r} + \frac{\nu_0' - \lambda_0'}{2}\right)\phi_0' - e^{\lambda_0}(\omega^2 e^{-\nu_0} - 1)\phi_0. \qquad \text{(C.13)}$$

We now introduce four perturbation fields—$\delta\lambda(t,r)$, $\delta\nu(t,r)$, $\delta\psi_1(t,r)$ and $\delta\psi_2(t,r)$—and expand about the equilibrium configuration by writing:

$$\lambda(t,r) = \lambda_0(r) + \delta\lambda(t,r) \qquad \text{(C.14)}$$

$$\nu(t,r) = \nu_0(r) + \delta\nu(t,r) \qquad \text{(C.15)}$$

$$\psi_1(t,r) = \phi_0(r)(1 + \delta\psi_1(t,r)) \qquad \text{(C.16)}$$

$$\psi_2(t,r) = \phi_0(r)\delta\psi_2(t,r). \qquad \text{(C.17)}$$

These last expressions are substituted into (C.2), (C.3), (C.4) and (C.6) to obtain the following equations for the perturbed quantities:

$$
\begin{aligned}
(re^{-\lambda_0}\delta\lambda)' &= r^2 \Big[2\phi_0^2\delta\psi_1 - e^{-\nu_0}\omega^2\phi_0^2\delta\nu + 2e^{-\nu_0}\omega^2\phi_0^2\delta\psi_1 \\
&\quad -2e^{-\nu_0}\omega\phi_0^2\delta\dot{\psi}_2 + 2e^{-\lambda_0}\phi_0'(\phi_0'\delta\psi_1 + \phi_0\delta\psi_1') - e^{-\lambda_0}\phi_0'^2\delta\lambda\Big] \text{(C.18)}
\end{aligned}
$$

$$\delta\nu' - \delta\lambda' = \left(\nu_0' - \lambda_0' + \frac{2}{r}\right)\delta\lambda - 4re^{\lambda_0}\phi_0^2\delta\psi_1 \qquad \text{(C.19)}$$

$$
\begin{aligned}
\delta\psi_1'' &+ \left(\frac{2}{r} + \frac{\nu_0' - \lambda_0'}{2} + 2\frac{\phi_0'}{\phi_0}\right)\delta\psi_1' + \frac{\phi_0'}{\phi_0}\left(\frac{\delta\nu' - \delta\lambda'}{2}\right) + e^{\lambda_0}\left(\omega^2 e^{-\nu_0} - 1\right)\delta\lambda \\
&- e^{\lambda_0 - \nu_0}\omega^2\delta\nu - e^{\lambda_0 - \nu_0}\delta\ddot{\psi}_1 - 2e^{\lambda_0 - \nu_0}\omega\delta\dot{\psi}_2 = 0 \qquad \text{(C.20)}
\end{aligned}
$$

$$
\begin{aligned}
&- \delta\lambda e^{-\lambda_0}\left(\frac{\nu_0' - \lambda_0'}{2r} + \frac{1}{2}\nu_0'' + \frac{1}{4}\nu_0'^2 - \frac{1}{4}\nu_0'\lambda_0'\right) \\
&+ e^{-\lambda_0}\left(\frac{\delta\nu' - \delta\lambda'}{2r} + \frac{1}{2}\delta\nu'' + \frac{1}{2}\nu_0'\delta\nu' - \frac{1}{4}\nu_0'\delta\lambda' - \frac{1}{4}\lambda_0'\delta\nu'\right) - \frac{1}{2}e^{-\nu_0}\delta\ddot{\lambda} \\
&= - \Big[e^{-\nu_0}\omega^2\phi_0^2\delta\nu - e^{-\nu_0}\left(-2\omega\phi_0^2\delta\dot{\psi}_2 + 2\omega^2\phi_0^2\delta\psi_1\right) - e^{-\lambda_0}\phi_0'^2\delta\lambda \\
&+ e^{-\lambda_0}\left(2\phi_0'^2\delta\psi_1 + 2\phi_0\phi_0'\delta\psi_1'\right) + 2\phi_0^2\delta\psi_1\Big]. \qquad \text{(C.21)}
\end{aligned}
$$

121

The four equations above can be manipulated such that two variables, $\delta\nu$ and $\delta\psi_2$ are eliminated, leaving us with only two equations in two unknowns. To obtain the first of these two equations, we subtract (C.18) from (C.20) to get

$$
\begin{aligned}
\delta\psi_1'' = & \quad - \left(\frac{2}{r} + \frac{\nu_0' - \lambda_0'}{2}\right)\delta\psi_1' - \frac{\delta\lambda'}{r\phi_0^2} + e^{\lambda_0 - \nu_0}\delta\ddot{\psi}_1 \\
& - \left[\frac{\phi_0'}{\phi_0}\left(\frac{\nu_0' - \lambda_0'}{2} + \frac{1}{r}\right) + \left(\frac{\phi_0'}{\phi_0}\right)^2 + \frac{1 - r\lambda_0'}{r^2\phi_0^2} + e^{\lambda_0 - \nu_0}\omega^2 - e^{\lambda_0}\right]\delta\lambda \\
& + 2e^{\lambda_0}\left[1 + e^{-\nu_0}\omega^2 + e^{-\lambda_0}\left(\frac{\phi_0'}{\phi_0}\right)^2 + r\phi_0\phi_0'\right]\delta\psi_1.
\end{aligned} \tag{C.22}
$$

To obtain the other equation, we differentiate (C.19) with respect to r, and substitute the resulting expression, along with (C.18) and (C.19), into (C.21) to get

$$
\begin{aligned}
\delta\lambda'' = & \quad - \frac{3}{2}(\nu_0' - \lambda_0')\delta\lambda' + \left[4\phi_0'^2 + \lambda_0'' + \frac{2}{r^2} - \frac{(\nu_0' - \lambda_0')^2}{2} - \frac{2\nu_0' + \lambda_0'}{r}\right]\delta\lambda + e^{\lambda_0 - \nu_0}\delta\ddot{\lambda} \\
& - 4(2\phi_0\phi_0' - re^{\lambda_0}\phi_0^2)\delta\psi_1' \\
& - 4\left[2\phi_0'^2 - re^{\lambda_0}\phi_0^2\left(2\frac{\phi_0'}{\phi_0} + \frac{2\nu_0' + \lambda_0'}{2}\right)\right]\delta\psi_1,
\end{aligned} \tag{C.23}
$$

where, differentiating (C.11) with respect to r we have

$$
\begin{aligned}
\lambda_0'' = & \quad \frac{e^{\lambda_0} - 1}{r^2} - \frac{e^{\lambda_0}\lambda_0'}{r} + \left[e^{\lambda_0}(\omega^2 e^{-\nu_0} + 1)\phi_0^2 + \phi_0'^2\right] \\
& + r\left[-\nu_0'\omega^2 e^{\lambda_0 - \nu_0}\phi_0^2 + e^{\lambda_0}(\omega^2 e^{-\nu_0} + 1)\left(\lambda_0'\phi_0^2 + 2\phi_0\phi_0'\right) + 2\phi_0'\phi_0''\right].
\end{aligned} \tag{C.24}
$$

(Note that (C.22) omits a factor of $\exp(\lambda_0)$ which one finds in the $\sim \delta\lambda/(r^2\phi_0^2)$ term of equation (34) in [43].) For the stability analysis, we assume a harmonic time dependence, *i.e.*,

$$
\delta\psi_1(t,r) = \delta\psi_1(r)e^{i\sigma t}
$$
$$
\delta\lambda(t,r) = \delta\lambda(r)e^{i\sigma t}.
$$

Note that (C.23) and (C.24) contain only second derivatives with respect to time. There are good arguments for assuming σ^2 is purely real [61, 43], so we can determine instability by simply looking for instances where $\sigma^2 < 0$.

As a further consideration, we note that the boson star system admits a conserved Noether current,

$$J^\mu = \frac{i}{8\pi} g^{\mu\nu} (\phi \partial_\nu \phi^* - \phi^* \partial_\nu \phi), \tag{C.25}$$

for which the corresponding charge or "particle number" is

$$
\begin{aligned}
N &= \int d^3 x \sqrt{-g} J^t \\
&= \int_0^\infty dr\, r^2 e^{(\lambda-\nu)/2} \left(\dot{\psi}_1 \psi_2 - \dot{\psi}_2 \psi_1 + \omega(\psi_1^2 + \psi_2^2) \right).
\end{aligned}
\tag{C.26}
$$

Conventional stability analysis (see, e.g., [95]) demands that we consider only perturbations for which the total charge is conserved. Thus we compute the variation in the charge, δN, and work to ensure $\delta N = 0$. In practice, since we cut off the grid at finite radius, it makes sense to consider the function $\delta N(r)$, the total charge enclosed in a sphere with surface area $4\pi r^2$. This quantity is

$$
\begin{aligned}
\delta N(r) &= \frac{1}{\omega} \int_0^r d\tilde{r}\, \tilde{r}^2 e^{(\nu_0 - \lambda_0)/2} \phi_0^2 \\
&\times \left\{ \frac{\delta\lambda'}{2\tilde{r}\phi_0^2} + \frac{1}{2} \left[e^{\lambda_0 - \nu_0} \omega^2 + \left(\frac{\phi_0'}{\phi_0} \right)^2 + \frac{1 - \tilde{r}\lambda_0'}{\tilde{r}^2 \phi_0^2} \right] \delta\lambda \right. \\
&\left. - \frac{\phi_0'}{\phi_0} \delta\psi_1' - \left[-e^{\lambda_0 - \nu_0} \omega^2 + \left(\frac{\phi_0'}{\phi_0} \right)^2 + e^{\lambda_0} \right] \delta\psi_1 \right\},
\end{aligned}
\tag{C.27}
$$

where primes denote $\partial/\partial\tilde{r}$. (Note that (C.27) contains a term involving $\delta\psi_1'$, which was not included in equation (35) of [43].) We then demand that $\delta N \to 0$ as $r \to \infty$.

The boundary conditions are as follows:

At $r = 0$:

$$\lambda_0 = 0$$

$$\nu_0 = 0$$

$$\phi_0' = 0$$

$$\phi_0'' = -\frac{1}{3}(\omega^2 - 1)\phi_0 \tag{C.28}$$

$$\delta\psi_1'' = \frac{1}{3}\left[-\frac{3\delta\lambda''}{2\phi_0^2} + \left(2(\omega^2 + 1) - \sigma^2\right)\delta\psi_1\right] \tag{C.29}$$

$$\delta\lambda = 0$$

$$\delta\lambda' = 0.$$

As $r \to \infty$:

$$\delta N \to 0$$

$$\delta\psi_1 \to 0$$

$$\delta\lambda \to 0.$$

To solve the system (C.23) and (C.24) subject to the above boundary conditions, for a given value of $\phi_0(0)$, we resort to the method of "shooting," first for the equilibrium solutions, then for the perturbed quantities. Specifically, we choose a value for ω and solve the equilibrium equations numerically by integrating outward from $r = 0$. We do this repeatedly, performing a "binary search" on ω (as described in [86]) until the boundary conditions for the equilibrium quantities are satisfied.

Due to the linearity of the problem, we can choose $\delta\psi_1(0)$ arbitrarily. We then have two parameters left, namely σ^2 and $\delta\lambda''(0)$. To make matters easy at first, we consider perturbations very close to the transition between stability and instability. At the transition point, σ^2 is zero. Thus for boson stars near the transition point, we choose $\sigma^2 = 0$ and shoot on the parameter $\delta\lambda''(0)$ until the boundary conditions are satisfied. As Gleiser and Watkins [43] note, the transition point occurs at the maximum boson star mass; so we can take two slightly different equilibrium solutions near the maximum mass and subtract them to generate solutions which should agree with those obtained from the perturbation problem. We use this method to obtain

a trial value of $\delta\lambda''(0)$, and also as a way of checking the final solution we obtain from the perturbation analysis.

For more general configurations ($\sigma^2 \neq 0$), we choose a value of σ^2 and shoot on $\delta\lambda''(0)$ until we find δN at the outer boundary of the grid to be less than some tolerance value. Then we use the fact (gleaned from experience) that if σ^2 is too large (too positive), δN will have a local minimum, the value of which will be less than zero (*i.e.*, $\delta N(r)$ will dip below zero and then turn back up at larger radii). If σ^2 is too low there will be no such local minimum. We use these two criteria to select the value of σ^2 via a binary search. Thus our two-dimensional eigenvalue-finding algorithm consists simply of two (nested) binary searches, one in each direction: For each value of σ^2 tried, a full binary search on the parameter $\delta\lambda''(0)$ is performed to drive $\delta N(r_{\mathtt{max}}) \to 0$. Then the solution of $\delta N(r)$ is examined for the behavior described above, and a new value of σ^2 is selected, and so on until both $\delta\lambda''(0)$ and σ^2 have been found to some desired precision.

Bibliography

[1] AVS Visualization Software, Advanced Visual Systems, Inc. http://www.avs.com/.

[2] A. M. Abrahams and C. R. Evans. Critical behavior and scaling in vacuum axisymmetric gravitational collapse. *Phys. Rev. Lett.*, 70:2980, 1993.

[3] E. Agol and J. H. Krolik. Magnetic stress at the marginally stable orbit: Altered disk structure, radiation, and black hole spin evolution. *Astrophys. J.*, 528:161–170, 2000.

[4] M. Alcubierre, G. Allen, B. Bruegmann, G. Lanfermann, E. Seidel, W.-M. Suen, and M. Tobias. Gravitational collapse of gravitational waves in 3D numerical relativity. *Phys. Rev.*, D61:041501, 2000.

[5] A. Anderson and J. James W. York. Fixing Einstein's equations. *Phys. Rev. Lett.*, 82:4384–4387, 1999.

[6] D. A. Anderson, J. C. Tannehill, and R. H. Plechter. *Computational Fluid Mechanics and Heat Transfer*. Hemisphere, 1984.

[7] A. Arbona and C. Bona. Dealing with the center and boundary problems in 1D numerical relativity. *Comput. Phys. Commun.*, 118:229, 1999.

[8] R. Arnowitt, S. Deser, and C. Misner. In L. Witten, editor, *Gravitation: An Introduction to Current Research*. Wiley, New York, 1962.

[9] J. Balakrishna, E. Seidel, and W.-M. Suen. Dynamical evolution of boson stars. II: Excited states and self-interacting fields. *Phys. Rev.*, D58:104004, 1998.

[10] T. Baumgarte. Cornell/NSCA-3+1 Group Report. Online recording of a presentation given at the ITP Miniprogram on Colliding Black Holes: Mathematical Issues in Numerical Relativity, January 2000. `http://online.itp.ucsb.edu/online/numrel00/baumgarte/`.

[11] M. J. Berger and J. Oliger. Adaptive mesh refinement for hyperbolic partial differential equations. *J. Comp. Phys.*, 53:484–512, 1984.

[12] M. J. Berger and I. Rigoutsos. An algorithm for point clustering and grid generation. *IEEE Trans. on Systems, Man, and Cybernetics*, 21:1278–1286, 1991.

[13] R. Blandford and R. Znajek. Electromagnetic extraction of energy from Kerr black holes. *M.N.R.A.S.*, 179:433–456, 1977.

[14] C. Bona and J. Massó. Hyperbolic evolution system for numerical relativity. *Phys. Rev. Lett.*, 68:1097–1099, 1992.

[15] P. R. Brady, C. M. Chambers, and S. M. C. V. Goncalves. Phases of massive scalar field collapse. *Phys. Rev.*, D56:6057–6061, 1997.

[16] S. Brandt, J. A. Font, J. M. Ibanez, J. Masso, and E. Seidel. Numerical evolution of matter in dynamical axisymmetric black hole spacetimes. I: Methods and tests. *Comput. Phys. Commun.*, 124:169, 2000.

[17] F. P. Brooks, Jr. *The Mythical Man Month: Essays on Software Enginnering, Anniversary Edition.* Addison-Wesley, 1995.

[18] B. Carter. Hamilton-Jacobi and Schrodinger separable solutions of Einstein's equations. *Commun. Math. Phys.*, 10:280–310, 1968.

[19] H. Chiba, A. Gay, P. Harnden, D. Knight, A. van Maanen, S. Pavey, M. Pont, J. Walton, and C. Weir. Iris Explorer 3.5. Scientific vizualization software. `http://www.nag.com/Welcome_IEC.html`.

[20] D.-I. Choi. *Numerical Studies of Nonlinear Schrdinger and Klein-Gordon Systems: Techniques and Applications.* PhD thesis, University of Texas at Ausin, 1998.

[21] M. W. Choptuik. Binary black hole grand challenge update. Talk given in Aspen, CO, Feb 1, 1997. `http://wwwrel.ph.utexas.edu/Members/matt/Doc/aspen97.ps`.

[22] M. W. Choptuik. ser: 1+1 D visualization software overview. `http://laplace.physics.ubc.ca/~matt/Software/ser/intro.html`.

[23] M. W. Choptuik. *Numerical Techniques for Radiative Problems in General Relativity.* PhD thesis, University of British Columbia, 1986.

[24] M. W. Choptuik. Universality and scaling in gravitational collapse of a massless scalar field. *Phys. Rev. Lett.*, 70:9–12, 1993.

[25] M. W. Choptuik. Critical behavior in scalar field collapse. In D. W. Hobill, A. Burd, and A. A. Coley, editors, *Deterministic Chaos in General Relativity*, page 155. Plenus Press, New York, 1994.

[26] M. W. Choptuik. `ad`: An implementation of the Berger-Oliger mesh refinement algorithm for the wave equation in spherical symmetry. Technical Re-

port UTREL/TR94-001, University of Texas at Austin, Center for Relativity, Technical Report, 1994. (unpublished).

[27] M. W. Choptuik. The Berger & Oliger algorithm using a shadow hierarchy for truncation error estimation, May 1995.
http://laplace.physics.ubc.ca/~matt/Doc/shadow0.ps.

[28] M. W. Choptuik. Personal communication, November 1997.

[29] M. W. Choptuik. Personal communication, July 2000.

[30] M. W. Choptuik, T. Chmaj, and P. Bizon. Critical behaviour in gravitational collapse of a Yang-Mills field. *Phys. Rev. Lett.*, 77:424–427, 1996.

[31] D. Christodoulou. Violation of cosmic censorship in the gravitational collapse of a dust cloud. *Comm. Math. Phys.*, 93:171–195, 1984.

[32] D. Christodoulou. A mathematical theory of gravitational collapse. *Commun. Math. Phys.*, 109:613, 1987.

[33] M. Colpi, S. Shapiro, and S. Teukolsky. The explosion of a rotating neutron star near the minimum mass. *Astrophys. J.*, 369, 1991.

[34] M. Colpi, S. L. Shapiro, and I. Wasserman. Boson stars: Gravitational equilibria of self-interacting scalar fields. *Phys. Rev. Lett.*, 57:2485, 1986.

[35] M. P. Dabrowski and F. E. Schunck. Boson stars as gravitational lenses. astro-ph/9807039, 1998.

[36] T. Damour. Black-hole eddy currents. *Phys. Rev. D*, 18:3598, 1978.

[37] R. d'Inverno. *Introducing Einstein's Relativity.* Clarendon Press, Oxford, 1992.

[38] C. R. Evans and J. S. Coleman. Observation of critical phenomena and self-similarity in the gravitational collapse of radiation fluid. *Phys. Rev. Lett.*, 72:1782–1785, 1994.

[39] J. Font, J. Ibáñez, and P. Papadopoulos. Non-axisymmetric relativistic Bondi-Hoyle accretion on to a Kerr black hole. *M.N.R.A.S.*, 305:920–936, May 1999.

[40] H. Friedrich. On the regular and asymptotic characteristic initial value problem for Einstein's vacuum field equations. *Proc. Roy. Soc. Lond.*, A375:169, 1981.

[41] S. Frittelli and O. A. Reula. First-order symmetric-hyperbolic Einstein equations with arbitrary fixed gauge. *Phys. Rev. Lett.*, 76:4667–4670, 1996.

[42] C. F. Gammie. Efficiency of magnetized thin accretion disks in the Kerr metric. `astro-ph/9906223`, 1999.

[43] M. Gleiser and R. Watkins. Gravitational stability of scalar matter. *Nucl. Phys.*, B319:733, 1989.

[44] R. L. Guenther, 1995. Private computer code.

[45] C. Gundlach. Critical phenomena in gravitational collapse. *Adv. Theor. Math. Phys.*, 2:1, 1998.

[46] C. Gundlach. Critical phenomena in gravitational collapse. *Living Reviews in Relativity*, 1999.

[47] B. Gustafsson, H.-O. Kreiss, and J. Oliger. *Time Dependent Problems and Difference Methods.* Wiley Interscience, New York, 1995.

[48] R. S. Hanni and R. Ruffini. Lines of force of a point charge near a Schwarzschild black hole. *Phys. Rev. D*, 8:3259, 1973.

[49] D. Harrison. Xgraph version 11.3.2. University of California Berkeley Electronics Research Laboratory, December 1989.

[50] S. W. Hawking. Black hole explosions. *Nature*, 248:30–31, 1974.

[51] J. F. Hawley. Global magnetohydrodynamical simulations of accretion tori. 1999.

[52] J. F. Hawley and C. R. Evans. Simulation of magnetohydrodynamic flows — a constrained transport method. *Astrophys. J.*, 332:659–677, 2000.

[53] J. F. Hawley and J. H. Krolik. Global MHD simulation of the inner accretion disk in a pseudo-Newtonian potential. `astro-ph/0006456`, 2000.

[54] S. H. Hawley. (unpublished). A collection of MPEG movies showing the effects of various outer boundary conditions can be found at `http://wwwrel.ph.utexas.edu/~shawley/bc.html`.

[55] S. H. Hawley and M. W. Choptuik. `bbh_grace` distribution. `http://wwwrel.ph.utexas.edu/Members/shawley/bbh_grace.html` .

[56] S. H. Hawley and M. W. Choptuik. Boson stars driven to the brink of black hole formation. `gr-qc/0007039`, 2000. Accepted August 15, 2000 for publication in *Phys. Rev. D*.

[57] S. D. Hern. Numerical relativity and inhomogeneous cosmologies. `gr-qc/0004036`, 1999.

[58] E. Honda. *Resonant Dynamics within the Nonlinear Klein-Gordon Equation*. PhD thesis, University of Texas at Ausin, 2000.

[59] P. Huebner. A scheme to numerically evolve data for the conformal Einstein equation. *Class. Quant. Grav.*, 16:2823, 1999.

[60] M. Israeli and S. Orszag. Approximation of radiation boundary conditions. *J. Comp. Phys.*, 41:115, 1981.

[61] P. Jetzer. Boson stars. *Phys. Rept.*, 220:163–227, 1992.

[62] D. Kaup. Klein-Gordon geon. *Phys. Rev.*, 172:1331, 1968.

[63] S. Koide, D. Meier, K. Shibata, and T. Kudoh. General relativistic simulations of early jet formation in a rapidly rotating black hole magnetosphere. *Astrophys. J.*, 536:668–674, 2000.

[64] T. Koike, T. Hara, and S. Adachi. Critical behavior in gravitational collapse of radiation fluid: A renormalization group (linear perturbation) analysis. *Phys. Rev. Lett.*, 74:5170–5173, 1995.

[65] H. Kreiss and J. Oliger. Methods for the approximate solution of time dependent problems. *GARP Publications Series*, No. 10, 1973.

[66] J.-W. Lee and I.-G. Koh. Galactic halos as boson stars. *Phys. Rev.*, D53:2236–2239, 1996.

[67] T. D. Lee and Y. Pang. Stability of mini-boson stars. *Nucl. Phys.*, B315:477, 1989.

[68] M. S. Madsen. A note on the equation of state of a scalar field. *Astrophys. and Space Science*, 113:205–207, 1985.

[69] R. L. Marsa. *Radiative Problems in Black Hole Spacetimes*. PhD thesis, University of Texas at Ausin, 1995.

[70] J. Massó, E. Seidel, and P. Walker. Adaptive mesh refinement in numerical relativity. `gr-qc/9412057`, 1994.

[71] E. W. Mielke and F. E. Schunck. Boson stars: Early history and recent prospects. gr-qc/9801063, 1997.

[72] E. W. Mielke and F. E. Schunck. Boson stars: Alternatives to primordial black holes? *Nucl. Phys.*, B564:185–203, 2000.

[73] C. A. Misner, K. S. Thorne, and J. A. Wheeler. *Gravitation*. Freeman, 1973.

[74] D. W. Neilsen and M. W. Choptuik. Critical phenomena in perfect fluids. *Class. Quant. Grav.*, 17:761, 2000.

[75] I. D. Novikov and K. S. Thorne. Astrophysics of black holes. In C. DeWitt and B. DeWitt, editors, *Black Holes*, pages 343–450, 1973. Lectures given at the 23rd session of the Summer School of Les Houches.

[76] J. R. Oppenheimer and H. Snyder. On continued gravitational contraction. *Physical Review*, 56:508.

[77] P. Papadopoulos and J. A. Font. Relativistic hydrodynamics around black holes and horizon adapted coordinate systems. *Phys. Rev.*, D58:024005, 1998.

[78] M. Parashar, J. Browne, C. Edwards, and K. Klimkowski. A common computational infrastructure for adaptive algorithms for pde solutions. In *Proceedings of Supercomputing '97*, 1997.

[79] R. Penrose. Asymptotic properties of fields and space-times. *Phys. Rev. Lett.*, 10:66–68, 1963.

[80] R. Penrose. Gravitational collapse: The role of general relativity. *Rev. del Nuovo Cimento*, 1:252–276, 1969.

[81] R. Penrose. *Techniques of Differential Topology in Relativity*. S.I.A.M., Philadelphia, 1972.

[82] W. H. Press, S. A. Teukolsky, W. T. Vetterling, and B. P. Flannery. *Numerical Recipes in Fortran 77: The Art of Scientific Computing*. Cambridge Univeristy Press, 2nd edition, 1992.

[83] O. A. Reula. Hyperbolic methods for Einstein's equations. *Living Reviews in Relativity*, 1998-3, 1998.

[84] B. Richardson. Introduction to parallel computing workshop, National Center for Supercomputing Applications, Sept 1999.

[85] L. F. Richardson. The approximate arithmetical solution by finite differences of physical problems involving differential equations, with an application to stresses in a masonry dam. *Phil. Trans. Roy. Soc.*, 210:307–357, 1910.

[86] R. Ruffini and S. Bonnazzola. Systems of self-gravitating particles in general relativity and the concept of an equation of state. *Phys. Rev.*, 187:1767, 1969.

[87] F. E. Schunck and A. R. Liddle. The gravitational redshift of boson stars. *Phys. Lett.*, B404:25–32, 1997.

[88] F. E. Schunck and D. F. Torres. Boson stars with generic self-interactions. gr-qc/9911038, 1999.

[89] E. Seidel and W.-M. Suen. Dynamical evolution of boson stars. 1. perturbing the ground state. *Phys. Rev.*, D42:384–403, 1990.

[90] E. Seidel and W. M. Suen. Oscillating soliton stars. *Phys. Rev. Lett.*, 66:1659, 1991.

[91] E. Seidel and W.-M. Suen. Formation of solitonic stars through gravitational cooling. *Phys. Rev. Lett.*, 72:2516–2519, 1994.

[92] E. Seidel and W.-M. Suen. Numerical relativity as a tool for computational astrophysics. gr-qc/9904014, 1999.

[93] N. Shakura and R. A. Sunyaev. Black holes in binary systems: Observational appearance. *Astron. & Astrophys.*, 24:337–355, 1973.

[94] J. Shalf, G. Pushkareva, and B. Miksa. Lca vision 1.0. http://zeus.ncsa.uiuc.edu/~miksa/LCAVision.html .

[95] S. Shapiro and S. Teukolsky. *Black Holes, White Dwarfs and Neutron Stars.* Wiley, New York, 1983.

[96] K. Sumiyoshi, S. Yamada, H. Suzuki, and W. Hillebrandt. The fate of a neutron star just below the minimum mass: Does it explode? *Astron. and Astrophys.*, 334:159, 1998.

[97] S. A. Teukolsky. Rotating black holes: Separable wave equations for graviational and electromagnetic perturbations. *Phys. Rev. Lett.*, 29:1114–1118, 1972.

[98] K. S. Thorne. *Black Holes and Time Warps: Einstein's Outragous Legacy.* W. W. Norton & Company, 1994.

[99] K. S. Thorne, R. H. Price, and D. A. MacDonald, editors. *Black Holes: The Membrane Paradigm.* Yale University Press, 1986.

[100] R. M. Wald. *General Relativity.* University of Chicago Press, 1984.

[101] P. Walker. A 2 & 3D clusterer for the DAGH system, 1999. http://jean-luc.ncsa.uiuc.edu/Codes/3DCluster/.

[102] J. W. York and T. Piran. The initial value problem and beyond. In R. A. Matzner and L. C. Shepley, editors, *Spacetime and Geometry: The Alfred Schild Lectures*, pages 147–176, 1982.

Vita

Scott Hearne Hawley, the son of Gerald S. Hawley and Carolyn S. Hawley, was born on October 18, 1972 in Hong Kong. Two years later, the family moved to Fairfax, Virginia where they stayed for nearly 25 years. Scott went to the Thomas Jefferson High School for Science and Technology and then majored in Physics at the College of William and Mary. After graduating in 1994, he worked for the Army Research Laboratory and then the Naval Research Laboratory until the fall of 1995, when he began his graduate studies in physics at the University of Texas at Austin. After receiving his Ph.D., he plans to move to Germany and work as postdoctoral fellow at the Max Planck Institut für Gravitationsphysik/Albert Einstein Institut in Golm, near Berlin.

Permanent Address: 171 Carefree Lane

Kilmarnock, VA 22482

This dissertation was typeset with $\text{\LaTeX}\,2_\varepsilon$[1] by the author.

---

[1] $\text{\LaTeX}\,2_\varepsilon$ is an extension of $\text{\LaTeX}$. $\text{\LaTeX}$ is a collection of macros for $\text{\TeX}$. $\text{\TeX}$ is a trademark of the American Mathematical Society. The macros used in formatting this dissertation were written by Dinesh Das, Department of Computer Sciences, The University of Texas at Austin.